Development and Analysis of Computational Methods to Study Hydrogen Bonding in Molecular Clusters

Ryan DiRisio

A dissertation
submitted in partial fulfillment of the
requirements for the degree of

Doctor of Philosophy

University of Washington

2022

Reading Committee:
Anne McCoy, Chair
Munira Khalil
Xiaosong Li

Program Authorized to Offer Degree:
Chemistry

University of Washington

Abstract

Development and Analysis of Computational Methods to Study Hydrogen Bonding in Molecular Clusters

Ryan DiRisio

Chair of the Supervisory Committee:
Professor Anne McCoy
Chemistry

Understanding the role of hydrogen bonding in the structure and dynamics of water is an ongoing challenge in physical chemistry. In particular, understanding how the quantum mechanical effects of molecular vibrations govern the structure and dynamics of water is of interest. The cornerstone method used to study this phenomenon in this work is Diffusion Monte Carlo (DMC), which can be used to obtain the ground state vibrational wave function of any arbitrary molecule or molecular cluster. Instead of attempting to model bulk water and its properties outright, small, gas-phase molecular and ionic clusters of water, which provide model systems to study hydrogen bonding and proton transfer, are studied.

To begin, DMC will be reviewed, and PyVibDMC, an open source, general purpose Python DMC software package developed as part of this work, will be discussed. As DMC is rigorously a ground state method, extensions to the DMC approach are required to obtain information about excited states. With excited state information, one can then directly compare simulation to experiment through theoretical and experimental spectroscopy. As such, next, the Ground State Probability Amplitude (GSPA) approximation is presented, and it is applied to protonated water clusters. In the GSPA approach, excited state wave functions are approximated based on simple products of polynomials of vibrational displacements with the ground state DMC wave function. The power of this approach is that one can construct

a small basis through which to comprehensively examine the vibrational state space of the chemical system of interest. Extensions to the GSPA approach that incorporate excited state mixing and improved descriptions of higher-order excited states states will be presented as well. These improvements lead to good agreement between the GSPA theoretical and gas-phase experimental vibrational spectra of $H_7O_3^+$ and $H_9O_4^+$. Using this rich theoretical approach, we are able to draw connections between the molecular vibrations and structures that govern proton transfer and experimental spectroscopy of the clusters.

A methodological procedure is presented next, which is the incorporation of machine learning into the DMC workflow. A potential energy surface is required for DMC simulations. Performing on-the-fly, *ab initio* potential energy calculations of molecular configurations in DMC simulations for systems beyond a few atoms is computationally intractable. As such, fitted potential energy surfaces are often employed for DMC simulations. However, as systems of interest increase in size, even the evaluations of these fitted surfaces become computationally demanding. To this end, a workflow is developed to use the large amount of data obtained from a small-scale DMC simulation to train a neural network to learn the potential energy surface of interest. Neural network structure, choice of descriptor, and hyperparameter optimization are reviewed and discussed in the context of other machine learning methods, and training data collection strategies are discussed, including the need to sample regions of the potential energy surface that are beyond regions accessed by a typical DMC simulation. Once the neural network surface is trained, it is evaluated in an extremely fast and highly-parallel manner, making DMC simulations significantly more efficient for H_2O, CH_5^+, and $(H_2O)_2$.

In the final section, DMC is set aside, and an exploration of the correlation between the vibrational spectral signature of an individual water molecule with its surrounding chemical environment is discussed. Specifically, the frequency of a hydrogen-bonded OH stretch in a water dimer pair is correlated to the number of solvating water molecules surrounding it.

A quantum mechanical model is constructed to quantify this correlation, and applications of the model to a sample water cluster show the causality between the change in quantum mechanical electron density in the hydrogen bonding region of a particular OH bond and its OH stretch frequency. The application of the quantum model formalizes and explains empirical trends and categorization approaches put forth in previous work to characterize hydrogen bonding environments. This model is then applied to the water network found in a $Cs^+ \cdot (H_2O)_{20}$ cluster, where these trends are again quantified and then related to both the first and second solvation shell of a hydrogen-bond donor/acceptor water pair within the larger network.

TABLE OF CONTENTS

LIST OF FIGURES

Figure Number Page

LIST OF TABLES

Table Number Page

ACKNOWLEDGMENTS

It's been quite a journey going through a good half of graduate school over the course of a pandemic. I sincerely would not have been able to make it through this program without all of the support from my friends, family, and colleagues.

First and foremost, I'd like to thank my family. My parents, Paula and Derek, supported my moving across the country to pursue a PhD in a city where I knew nobody and my entry into a program where I was swapping academic sub-disciplines. I'm very grateful they simultaneously gave me the space and support I needed to grow into the scientist and person I am today, and I could not have done it without them. Next I'd like to thank my brother, Chris, who had his own journey through law school, marriage, and the birth of his firstborn son. I couldn't feel more supported by him, if not just by the comforting feeling that my older brother is at such a good point in his life. I thank my grandma Annette (Det), my late grandpa Onofrio (Nuff), and aunt Maria (M), who bring so much joy into my life through their constant support and love. I want to thank my grandma and late grandpa, Geraldine (Ger) and Roderick (Rod), who were always a pleasure to see when I was back in town for the holidays and who were always very supportive of me and my brother.

I'd like to next thank my friends all over the country who helped me get through graduate school. At UW, I'd like to especially thank Diana Roh, Robert Weakly, Sarah Sweger, and Jason Sandwisch for their help on problem sets, projects, and research questions, but more importantly for the coffee runs, commisseration sessions, and special nights out we had throughout graduate school. In the McCoy group, I'd like to thank all of the lab for their support. Lindsey Madison, Meng Huang, Meredith Fore, Victor Lee, Mark Boyer, Rachel Huchmala, Jacob Finney, Coire Gavin-Hanner, Fenris Lu, Mickey Moonkaen, Luke Hatcher,

Chloe Chiu, Nick Vetterli, and Mathew Joyner, you all have had more impact on me and my academic growth than you think.

I'd also like to thank some friends from William and Mary: Cati Gurri, Marissa Kleiman, Harrison Schindler, Pryce Fortune, and Muzzammil Mehdi. We all helped keep each other sane in the post-graduation malaise, whether it be through playing video games together, watching weird movies together, or just chatting online. For this I'll be forever grateful, and I'm looking forward to spending more time with everyone on the East Coast.

I'd like to thank all of the teachers and professors that I was able to grow from over the years, particularly those in Chemistry: Ms. Monda, Dr. Wustholz, and Dr. Bagdassarian, you were all inspirations for me. In particular, I thank Dr. McNamara, you were a fantastic mentor to me in my undergraduate research career, and you made me realize how much I truly enjoy the act of Chemistry and Chemistry research.

I would like to thank the Molecular Sciences Software Institute (MolSSI) for awarding me a Software Fellowship to write PyVibDMC. I would especially like to thank Dr. Jessica Nash, the MolSSI Education Lead, and Dr. Jonathan Moussa, my mentor, for their training and guidance throughout the fellowship. I am thankful that MolSSI set me up for a successful career in scientific software development.

I'd like to thank my advisor, Dr. Anne McCoy, who has been a fantastic mentor throughout graduate school. You allowed me to grow into a full-fledged theoretical chemist who can think and speak like a scientist, which is an amazing gift. You also facilitated my growth into a scientific programmer, and since I am now going to pursue a career in this field, I will be forever grateful for your support. None of this thesis could have been written without you!

Finally, last but certainly not least, I'd like to thank my partner, Kareem. You were always there for me throughout this entire process, despite going through a master's degree at the same time. Being able to visit you in Vancouver, and then being able to live with you afterwards in Seattle, really was my saving grace throughout graduate school. I'm looking forward to our continued journey in New York City as we both embark on the next step of our professional careers and our lives.

DEDICATION

to my parents, Paula and Derek, my brother, Christopher, and my partner for life, Kareem.

Chapter 1

INTRODUCTION

1.1 Hydrogen Bonding

Water is a fundamental component of human life. Water is ubiquitous in the human body and one of the main components of our sustenance and our external environment. Water is a unique substance, though, as it contains a hydrogen bonding network that leads to unique physical and chemical properties. Hydrogen bonding is typically defined as the exceptionally strong intermolecular dipole-dipole interaction between molecules with hydrogen atoms and molecules with strongly electronegative atoms such as oxygen, nitrogen, and fluorine. The properties of water that are, in part, a result of hydrogen bonding include the exceptionally high boiling point of liquid water, the higher density of liquid water relative to solid water at the same temperature, and the change in density of water when the hydrogen atoms are replaced with deuterium atoms. While it is convenient to consider these hydrogen bond interactions between water molecules as static interactions as one would observe in a textbook, the dynamic, thermochemical aspect of the real world leads to an intricate, ever-changing hydrogen bonding network in any sample of liquid water in the universe. In addition, even at zero Kelvin, there is an intrinsic amount of energy associated with the molecular vibrations of water molecules, purely due to the effects of quantum mechanics. Along with these nuclear quantum effects, the electrostatic interactions between water molecules, mentioned above, lead to dynamical attraction or repulsion the atomic nuclei of a water molecule in a given network. While neither the phenomena of zero-point energy nor electrostatic interactions is specific to water, the unusually strong hydrogen bonding interactions and quantum effects make the substance difficult to model on the bulk scale.

1.2 Modeling Water Clusters

In chemical simulation, it is difficult to model bulk water and its interactions with solutes fully quantum mechanically. Many different approaches have been taken to approximate the effect of water on a chemical environment, including polarizable continuum models and coulombic and Lennard Jones interactions.[12–14] In this work, we do not focus on providing a quantum mechanical description of water for solute-solvent interaction. Instead, an effort is made to gain insights into the structure and physics of water by modeling it fully quantum mechanically, both in the electronic and vibrational dimensions outlined above. In particular, the majority of this work will focus on the implications of treating the molecular vibrations of water quantum mechanically, and the implications of this treatment on the dynamics and structure of the intermolecular interactions of water. Since modeling bulk water would require the the study of more than 10^{22} molecules, instead we turn to model systems where we can computationally study water in great detail. These model systems are referred to as water clusters, and they are small, gas phase models of water that contain on the order of 3 to 100 atoms.

In order to study these clusters quantum mechanically, a computational and theoretical framework is needed. To begin, the molecular Schrödinger equation must be solved. The Born-Oppenheimer approximation[15] is typically invoked so that the energy and wave function for a given molecule can be expressed as a sum of the electronic and vibrational components separately. The electronic wave function is calculated by numerically solving the electronic Schrödinger equation for the system given the positions of the nuclei, which are treated as stationary. The vibrational Hamiltonian for a single water molecule in Cartesian coordinates, within the Born-Oppenheimer approximation, is written:

$$\hat{H} = -\frac{\hbar^2}{2}\sum_{n=1}^{3}\frac{1}{m_n}\nabla_n^2 + V(\mathbf{x}) \tag{1.1}$$

where m_n is the mass of atom n (either oxygen or hydrogen) and $\mathbf{x}$ is the vector of nuclear coordinates of the water molecule. The form of the potential energy, $V(\mathbf{x})$ for a water monomer, or any arbitrary molecule, is not analytically known, and it must be calculated numerically. Additionally, there is not a generic set of coordinates that describes each vibrational problem at hand perfectly. In the most basic and popular approximation, the harmonic oscillator approximation, the potential energy is assumed to be quadratic in the molecular coordinates, and the wave function is assumed to be a direct product of $3N - 6$ uncoupled, one-dimensional quantum harmonic oscillators that follow the vibrational normal modes of the system of interest. Within the harmonic oscillator approximation, the vibrational normal modes are a set of orthogonal coordinates for which the mass-weighted Hessian Matrix

$$S_{ij} = \frac{\partial^2 V(\mathbf{q})}{\partial q_i \partial q_j} \tag{1.2}$$

is diagonal. While there are errors already in the characteristic frequencies of the vibrations in a single water monomer, the harmonic approximation breaks down further as the number of water molecules one wishes to study increases. This is because the form of the potential energy surface of larger systems is largely anharmonic, particularly in coordinates that describe the intermolecular interactions between water monomers.

There are many quantum mechanical models that include anharmonicity of molecular vibrations. Vibrational Perturbation Theory to second order (VPT2)[16] is an extension beyond the harmonic approximation through the introduction of higher order terms in the expansion of the vibrational Hamiltonian. The Vibrational Self-Consistent Field approach (VSCF)[17] assumes a direct product form of the wave function like the harmonic approximation, but incorporates the full-dimensional, anharmonic potential energy surface instead of the assumed parabolic functional form described above. The vibrational wave function is solved self-consistently, and the resultant wave function is a direct product of anharmonic oscillators. The accuracy of VSCF energies and wave functions can be improved by performing Vibrational Configuration Interaction (VSCF/VCI)[18] calculations, which allow for coupling between these wave functions.

The methods described above are typically implemented as extensions of the harmonic oscillator approximation. An alternative method to these types of approaches is Diffusion Monte Carlo (DMC).[19,20] Briefly, DMC is a stochastic method that is used to obtain the ground state solution to the time independent Schrödinger equation by propagating a basis of localized functions, referred to as walkers, forward in imaginary time ($\tau = \frac{it}{\hbar}$). The benefit of the DMC approach is that the use of such a basis does not assume anything about the molecular vibrations or structure of a system, is fully anharmonic, and the approach scales favorably with system size. At the end of a DMC simulation, one obtains a representation of the ground state vibrational wave function, and the vibrational zero-point energy mentioned above.

1.3 Outline of Thesis

This work is divided into four sections. In the first section, the DMC theory and algorithm are reviewed, and PyVibDMC, a code for performing DMC simulations written by our group, is discussed.

The second section focuses on the application and analysis of the results of DMC simulations to the structure and spectroscopy of protonated water clusters. These protonated water clusters consist of three or four water molecules with an excess proton. The structure and spectroscopy of such systems are important since these clusters act as models for the understanding of proton transfer. As such, we use the rich amount of nuclear quantum mechanical information encoded in the ground state DMC wave function to understand the structure and physics of these protonated clusters, and how this structural information can be related experimental vibrational spectroscopy of such systems.

The third section discusses a DMC simulation advancement. In a DMC simulation, the potential energy of each walker must be calculated at each time step. This leads to millions to billions of potential energy surface evaluations per simulation. The potential energy is typically calculated numerically using codes from other theoretical chemistry research groups, and this evaluation is the bottleneck of DMC simulations. To this end, we use artificial neural networks to learn the section of the potential energy surface that is relevant to DMC simulations by running small scale calculations to collect training data. Once these neural network potential energy surfaces are generated, we can evaluate the potential energy on Graphics Processing Units (GPUs) for fast and highly parallel evaluations in a fraction of the time.

The fourth and final section is a study on relating the electrostatic hydrogen-bonding environment of a given water molecule in a larger water cluster to its vibrations, specifically the hydrogen-bonded OH stretching vibration. Modeling the relationship between the change in electron density of a water molecule given its hydrogen bonding environment is both a way to quantify the effects of quantum mechanics on a a hydrogen bond donor/acceptor pair in a larger network, but also a way to explain how the fundamental interactions between molecules leads to the spectral features of liquid water that are observed on the macro scale.

Chapter 2

THE APPLICATION OF DIFFUSION MONTE CARLO TO SYSTEMS THAT DISPLAY LARGE AMPLITUDE MOTIONS

2.1 Introduction

In 1929, Dirac said[21]

> The underlying physical laws necessary for the mathematical theory of a large part of physics and the whole of chemistry are thus completely known, and the difficulty is only that the exact application of these laws leads to equations much too complicated to be soluble. It there fore becomes desirable that approximate practical methods of applying quantum mechanics should be developed, which can lead to an explanation of the main features of complex atomic systems without too much computation.

Of the currently available methods for solving quantum mechanical problems in chemistry, some of the most promising avenues for meeting Dirac's challenge are those that are based on diffusion quantum Monte Carlo (DMC). One particularly attractive feature of DMC is that it is amenable for high levels of parallelization, and for many years, the electronic structure community has looked towards developing and implementing DMC algorithms on the the state of the art large-scale supercomputing resources.[22,23] While there has been much activity in developing and extending approaches for obtaining accurate solutions to the electronic Schrödinger equation using quantum Monte Carlo approaches, and the reader is referred to reviews of that work,[24–31] these approaches can also provide powerful tools for exploring the solution to the nuclear Schrödinger equation. This introduction to DMC provides a discussion of the simulation method in the context of this class of problems. We will also discuss a method that can be used to obtain expectation values from the DMC wave function, descendant weighting.

2.2 *Theory of Diffusion Monte Carlo*

The DMC approach is based on solving the time-dependent Schrödinger equation, which has been rotated to imaginary time by replacing the time variable, t, with $\tau = it/\hbar$. Expressed in this way,[19,32]

$$\frac{d\Psi}{d\tau} = -(\hat{H} - E_{\text{ref}}))\Psi(\mathbf{x}, \tau) \tag{2.1}$$

where for a molecule that contains N atoms,

$$\hat{H} = \sum_{k=1}^{N} \frac{\hat{\mathbf{p}}_k^2}{2m_k} + V(\mathbf{x}) \tag{2.2}$$

The general solution to Eq. 2.1 can be expressed as

$$\Psi(\mathbf{x}, \tau) = \sum_n c_n(\tau = 0) e^{-(E_n - E_{\text{ref}})\tau} \varphi_n(\mathbf{x}) \tag{2.3}$$

where

$$\hat{H}\varphi_n(\mathbf{x}) = E_n \varphi_n(\mathbf{x}) \tag{2.4}$$

In the limit of large τ,

$$\Psi(\mathbf{x}, \tau) = c_0(\tau = 0) e^{-(E_0 - E_{\text{ref}})\tau} \varphi_0(\mathbf{x}) \tag{2.5}$$

In the above expressions, the energy has been shifted by a value, E_{ref}. This parameter will be used in the simulation to obtain an estimate to E_0 by requiring that the amplitude of Ψ remains constant throughout the simulation.

The above expressions are general and do not require Monte Carlo approaches to solve nor do they appear to be related to diffusion. The diffusion aspect of DMC arises from the isomorphism between Eq. 2.1 and a diffusion equation with a coordinate-dependent rate process.[19,32] This provides one approach for obtaining the working equations for DMC. Here we will utilize the solution to the time-dependent Schrodinger equation based on propagators[33–35]

$$\begin{aligned}\Psi(\mathbf{x}, \tau + \Delta\tau) &= e^{-(\hat{H} - E_{\text{ref}})\Delta\tau}\Psi(\mathbf{x}, \tau) \\ &\approx e^{-(\hat{V} - E_{\text{ref}})\Delta\tau} e^{-\hat{T}\Delta\tau}\Psi(\mathbf{x}, \tau) \qquad (2.6)\end{aligned}$$

where $\Psi(\mathbf{x}, \tau)$ is represented by a weighted sum of localized functions, $g(\mathbf{x})$,

$$\Psi(\mathbf{x}, \tau) = \sum_j w_j(\tau) g_j(\mathbf{x} - \mathbf{x}_j(\tau)) \qquad (2.7)$$

In the discussion that follows, these localized functions will be referred to as walkers. Analyzing the action of the propagator in Eq. 2.6 on a single localized function, we find that the kinetic energy term leads to an increase of the width of the function in the Cartesian coordinates of the kth atom to

$$\sigma_k = \hbar\sqrt{\Delta\tau/m_k} \qquad (2.8)$$

To retain the form of Ψ as a sum of localized functions, rather than allowing the widths of each of the $g(\mathbf{x} - \mathbf{x}_j)$ functions to increase at each time step, the position of the center of each of these functions is displaced by an amount δ_j. The values of the elements of δ_j are selected from a Gauss-random distribution, with a width in the coordinates of the kth atom that is given by σ_k.

The other term in Eq. 2.6 takes the role of the potential energy. Since Ψ is represented as an ensemble of localized functions we find that the effect of this term is to update the value of w_j in Eq. 2.7 based on the value of

$$P_j(\tau) = \exp\left[-(V(\mathbf{x}_j(\tau + \Delta\tau)) - E_{\text{ref}}(\tau))\Delta\tau\right] \qquad (2.9)$$

Updating the w_j can be accomplished through one of two approaches. The first, termed continuous weighting, allows the weights of the walkers to be updated at each time step based on[36]

$$w_j(\tau + \Delta\tau) = P_j(\tau) w_j(\tau) \tag{2.10}$$

This approach can be effective for short time propagations, but at longer times some of the w_j become very large while others approach zero. This results in the ensemble containing a large number of walkers that have low weights and a small number of walkers that carry most of the weight. To avoid this problem, we limit the range of allowed values for the w_j by defining $w_{\max}$ and $w_{\min}$, which provide the maximum and minimum allowed values for the w_j. If the weights of one or more of the walkers fall below $w_{\min}$, the following steps are followed for each of the low-weight walkers:

1. The walker with the largest weight is identified.
2. The coordinates of the low-weight walker are replaced by those of the walker with the largest weight
3. The weights of the low- and largest weight walkers at are replaced by half the value of the weight of the largest weight walker

Likewise, if after this procedure the weights of one or more of the walkers exceed $w_{\max}$ an analogous procedure is followed. This removal of walkers is referred to as branching. We have found that setting a minimum value weight of 0.01 to 0.1 and a maximum value of 20 results in a stable simulation.[37]

An alternative to continuous weighting is discrete weighting.[20] In this approach, the weights of all of the walkers are set to 1. While in continuous weighting, the number of walkers remains constant throughout the simulation, in discrete weighting the ensemble size fluctuates. In discrete weighting, we once again start by evaluating $P_j(\tau)$ using Eq. 2.9. The integer part of $P_j(\tau)$ provides the number of walkers centered at $\mathbf{x}_j$ that will be in the ensemble at the start of the next step in the propagation. The fractional part of $P_j(\tau)$ provides the probability that one additional walker will introduced be at these coordinates. The determination of whether (or not) to introduce this additional walkers is made by comparing the fractional part of $P_j(\tau)$ to a random number taken from a uniform distribution on the range of [0,1]. If the random number is smaller than the fractional part of $P_j(\tau)$, an additional walker that is centered at $\mathbf{x}_j$ is added to the ensemble. As noted above, in the discrete weighting scheme, all of the weights are constrained to be equal to one.

Once the weights have been determined, the final step of the simulation is to evaluate E_{ref}. As noted above, the purpose of E_{ref} is to ensure that the amplitude of the wave function remains constant. This is achieved by keeping the sum of the weights constant. To this end,[19]

$$E_{\mathrm{ref}}(\tau) = \frac{\sum_j w_j(\tau)V(\mathbf{x}_j)}{\sum_j w_j(\tau)} - \frac{\alpha \sum_j w_j(\tau)}{\sum_j w_j(\tau = 0)} \tag{2.11}$$

where α is a simulation parameter, which is introduced to keep the ensemble size constant. We have found that using $\alpha = 0.5/\Delta\tau$ works well.[38, 39] This is illustrated in Figures 6 and S2 of Ref. 39. One can see that we achieve the desired effect as in cases where the sum of the weights becomes smaller than the sum of the weights at $\tau = 0$, E_{ref} is increased, placing more walkers in the classically allowed region of configuration space where $\exp[-V(\mathbf{x}) - E_{\mathrm{ref}})] > 1$, thereby leading to an increase in the sum of the weights at the next time step.

The above procedure, which can be summarized as

1. Generate displacements of the walkers, δ.
2. Evaluate $V(\mathbf{x}(\tau)$.
3. Evaluate $P(\tau)$ using Eq. 2.9.
4. Update the weights, w, and branch walkers as needed.
5. Update E_{ref}

is repeated for sufficient time steps to obtain converged results. For time steps of 1.0 a.u., generally runs of 10 000 or more time steps are performed. To obtain the zero-point energy E_0, one averages E_{ref} over a portion of the DMC simulation. Discussion of this procedure can be found elsewhere.[39]

The above description is based on performing the DMC simulation in Cartesian coordinates as this is the most common choice. One can use other coordinates with minor adjustments to the above algorithm.[40] Additionally, one can incorporate guiding functions into the DMC algorithm. Discussion of this technique is found elsewhere.[41]

2.2.1 Initializing the ensemble of walkers

The above procedure is predicated on an initial distribution of walkers. Over the years, we have employed several approaches to obtain an initial distribution of walkers. One option is to localize all of the walkers at a minimum in the potential.[42] This approach can be advantageous if the potential contains multiple minima and the state of interest is not localized in the global minimum. Generally, though such a bias is not desired.

Another simple algorithm involves placing the center of mass of the system of interest at the origin, and multiplying the Cartesian coordinates of all of the atoms by a scaling factor. This places the walkers in a high energy region of the potential, from which it can relax toward the potential minimum. A third approach samples the coordinates based on the ground state probability amplitude obtained through a normal mode analysis of the potential.[43] For vibrations that are highly anharmonic, the width of the distribution in these coordinates may be expanded by multiplying the sampled normal mode coordinate by a constant scaling factor. Finally, when the ground state wave function is expected to sample multiple minima, the initial ensemble may be generated by sampling geometries from each of the relevant minima. This final approach should be employed when one is studying partially deuterated systems where the energy differences among the isotopologues are small.

2.2.2 Probability Amplitude and Descendant Weighting

A DMC simulation produces a discrete, full-dimensional representation of the ground state vibrational wave function. While this is a useful quantity itself, from Ψ^2 one can obtain expectation values of operators and visualizations of the probability amplitude along displacements of vibrational coordinates. Unfortunately, taking the square of a multidimensional, discretized wave function is nontrivial. To address this, there are multiple methods to obtain and evaluate integrals over Ψ^2 from DMC that are summarized elsewhere.[34,36,44] Here, we will briefly discuss one of these methods called descendant weighting. The core idea behind descendant weighting is that, at each position of each of the walkers, one must find a way to evaluate a second representation of Ψ. It has been shown[36,44] that one can relate the ratio of the weight (or number of descendants) of a given walker at time $\tau + \tau_{DW}$ and the weight some time earlier at τ to another evaluation of the wave function. This ratio is referred to as the descendant weight, and the value of τ_{DW} is the amount of time one allows the ensemble to propagate before collecting the weights once more. With the descendant weights, one can perform Monte Carlo Integration to evaluate expectation values[36]

$$\langle A(\mathbf{x}) \rangle = \int \Psi^*(\mathbf{x}) A(\mathbf{x}) \Psi(\mathbf{x}) d\mathbf{x} = \frac{\sum_j A(\mathbf{x}_j) d_j}{\sum_j d_j} \tag{2.12}$$

where d_j is the descendant weight of the jth walker in the ensemble, and A is an arbitrary multiplicative operator. The calculation of expectation values of differential operators requires additional computation or approximation, as it is nontrivial to take a derivative of the wave function in its current form. In addition to evaluating expectation values, one can examine projections of the probability amplitude onto certain coordinates by taking the discrete set of walkers and organizing them into ranges of values. The walkers are separated into bins along the vibrational coordinate, and the probability amplitude is the sum of the values of d_j in a particular bin. Operationally, this visualization is done by binning the walkers and examining them in the form of a histogram. For multidimensional DMC wave functions, one must project the probability amplitude onto one or more coordinates of interest, effectively integrating over all other degrees of freedom. Typically, this takes the form of a one or two-dimensional histogram of the probability amplitude along the coordinates of interest, such as bond lengths or angles.

2.3 PyVibDMC

While there are software packages for performing DMC simulations for electronic structure problems,[23,45] there were previously no formalized codes for DMC simulations of vibrational problems. To this end, we present PyVibDMC, an open source, general purpose diffusion Monte Carlo software package written in Python.[46] With the support of the Molecular Sciences Software Institute (MolSSI), this package was written in order to provide a formal, standardized, and maintainable implementation of the DMC algorithm across research groups, as well as provide an efficient and straightforward implementation for new users.

As a potential energy surface is required to evaluate the energy of each walker at each time step in a DMC simulation, PyVibDMC provides an efficient application program interface (API) that is flexible enough to support any potential energy surface that can be called within Python. The parallelization of the potential energy surface call for the ensemble of walkers within the DMC simulation can be done externally, or PyVibDMC is equipped with multi-core parallelization through Python's multiprocessing package or multi-node parallelization through MPI4Py. As will be mentioned in a later chapter, this flexible API also supports Graphics Processing Unit (GPU)-accelerated potential energy surfaces.

In addition to providing an API for potential energy surfaces, PyVibDMC also provides the user a suite of tools for analysis of DMC wave functions and energies. This includes calculating expectation values via descendant weighting, averaging over E_{ref} to obtain E_0, and projecting Ψ^2 onto various types of vibrational coordinates (bond lengths, angles, dihedral angles, etc.). Tutorials on how to use the code to perform DMC simulations, analyze them, and more are found in PyVibDMC's documentation. The code is available on GitHub, has extensive documentation on ReadTheDocs, and can be installed via the Python Package Index (PyPI).

Chapter 3

USING DIFFUSION MONTE CARLO WAVE FUNCTIONS TO ANALYZE THE VIBRATIONAL SPECTRA OF $H_7O_3^+$ AND $H_9O_4^+$

Reproduced in part with permission from [Ryan J. DiRisio, Jacob M. Finney, Laura C. Dzugan, Lindsey R. Madison, and Anne B. McCoy. Using Diffusion Monte Carlo Wave Functions to Analyze the Vibrational Spectra of $H_7O_3^+$ and $H_9O_4^+$. *J. Phys. Chem. A* **2021** ,125 (33), 7185–7197]. Copyright [2021] American Chemical Society.

3.1 Introduction

The study of the proton transfer mechanism in water is an important area of investigation. Advances in experimental techniques have allowed for the study of this mechanism in bulk systems,[47,48] the air/water interface,[49–51] nanodroplets and reverse micelles,[52,53] and gas-phase water clusters.[2,5,54–59] Cold, protonated water clusters provide model systems through which one can experimentally and theoretically interrogate the underlying physics of an excess proton in a known environment. In particular, vibrational spectroscopy of these systems allows for the direct interrogation of the motions that underpin proton transfer.

Experimental and theoretical studies of $H^+(H_2O)_{n=1-4}$ have demonstrated that the incorporation of nuclear quantum effects is essential to obtain an accurate description of the vibrational dynamics and spectroscopy of these systems.[2,4,5,60–67] Additionally, these studies show how the position, width and structure of the spectral feature that corresponds to the transition to the state with one quantum of excitation in a hydrogen-bonded OH stretch in the hydronium core is modulated by the cluster size and solvation environment.[56] Much can be learned from the analysis and theoretical reproduction of the spectra of the protonated water clusters. As chemists an important aspect of this type of work is in the ability to make connections between the features in the spectrum and the underlying bond strengths and structure of the ion that is being studied.

Analysis of changes to the vibrational frequency of the shared proton stretch with cluster size and structure has shown that the changes reflect the couplings between the OH stretch vibrations that lead to proton transfer and various intra- and intermolecular vibrations of the donating hydronium ion and the accepting water molecule. These couplings are also responsible for the evolution of the spectral envelope of the feature associated with the shared proton stretch. These large couplings make protonated water clusters challenging systems for computational approaches, such as vibrational perturbation theory (VPT2) or reduced dimensional treatments, which rely on a good zero-order description.[1,4,63,67] An alternative approach involves the use of large basis set calculations, e.g. vibrational self-consistent field/vibrational configuration interaction (VSCF/VCI) approaches. Yu and Bowman have performed VSCF/VCI calculations of the spectra of the protonated water trimer ($H_7O_3^+$) and tetramer ($H_9O_4^+$) using a Hamiltonian that is expressed in the normal mode coordinates of the ion of interest, focusing on the 18 and 24 vibrations that are expected to be responsible for the spectral features in $H_7O_3^+$ and $H_9O_4^+$,[2,4,65] respectively. The large couplings among the normal modes meant that large basis sets were needed to obtain converged results. The large basis along with a coordinate choice that did not follow the curvilinear nature of the molecular vibrations made the interpretation of the resulting spectra challenging.[2–5,65,66] This problem is most severe in the low energy region of the spectrum, which is dominated by large amplitude, low-frequency motions. The exclusion of the low-frequency vibrations in the VSCF/VCI analysis renders this spectral region inaccessible by this approach, while the large cubic and quartic terms in the expansion of the Hamiltonian lead to divergent behavior in VPT2 calculations. For this region, quasiclassical calculations as well as classical and ring polymer molecular dynamics calculations have been used to study this region of the spectrum.[5,66]

The focus of the present study will be on the examination of the molecular vibrations in $H_7O_3{}^+$ and $H_9O_4{}^+$, and their deuterated analogs. The vibrational spectra of $H_7O_3{}^+$ and $H_9O_4{}^+$are quite similar, both in the low frequency region (200-1000 cm^{-1}) and much of the region that corresponds to the $\Delta n = 1$ transitions of the OH stretches and bends (1000-4000 cm^{-1}). The main spectroscopic differences between the two systems are in the shared proton stretching region, where the spectrum of $H_7O_3{}^+$ has a series of peaks from approximately 1800-2500 cm^{-1}, and the shared proton stretching region of $H_9O_4{}^+$ consists of a single, broad peak centered at 2650 cm^{-1}.

Previous theoretical studies of $H_7O_3{}^+$ have shown that the series of intense peaks in the region of the $\Delta n = 1$ transition of the shared proton stretch result from intensity borrowing.[2,3,63,65,67] Specifically, there are a number of vibrational states that are nearly degenerate with the state with one quantum of excitation in the shared proton stretching mode, which can mix with that state. The importance of intensity borrowing among several states makes the interpretation of this region of the spectrum difficult. It also results in a large difference in the shape of the spectral envelope of this region upon deuteration. Despite the large amplitude nature of the vibrations, degenerate forms of VPT2, which are based on normal mode Hamiltonians expressed in internal[1] and Cartesian[67] coordinates as well as VSCF/VCI calculations[2] all provide reasonable reproductions of the spectral envelopes for $H_7O_3{}^+$ and $D_7O_3{}^+$. An analysis of the states that contribute to the peaks in the calculated spectra in the region of the $n = 1$ level in the shared proton stretch shows that many of these transitions involve two quanta of excitation in low frequency modes.

While there are fewer peaks in the shared proton region of the spectrum in $H_9O_4{}^+$and $D_9O_4{}^+$, Bowman and Yu assigned the broad shared proton stretch feature as a series of complicated combination bands involving the shared proton stretching vibration and rotations and bends of the hydronium core, and the results of degenerate VPT2 calculations indicated that the band was composed of the shared proton stretching mode as well as umbrella and hydronium bend combinations.[4,68]

While progress has been made in interpreting the spectra of these systems, the analysis is sensitive to the choice of coordinates. The observation that degenerate VPT2 calculations based on states with up to two quanta of excitation provide a reasonable description of the spectra of ${H_7O_3}^+$ and ${H_9O_4}^+$[1,59,67] leads us to conclude that if we can identify a good set of coordinates, we may be able to obtain a reasonable description of the spectrum using a much smaller basis than is required for the previous VSCF/VCI calculations.

To explore this possibility, we will use insights gained from the ground state probability amplitudes for ${H_7O_3}^+$ and ${H_9O_4}^+$, which were obtained from diffusion Monte Carlo (DMC) simulations.[37] DMC is a stochastic method in which an ensemble of localized functions, referred to as walkers, randomly samples the potential energy surface for the system of interest. The DMC ground state wave function is represented by the density of walkers near the configuration of interest. While DMC provides a powerful approach for obtaining information about the vibrational ground state wave function and energy of a molecular cluster, extracting information about excited states presents significant challenges. First, without further modification to the algorithm,[69] each excited state must be calculated independently, and each state is described by distinct ensembles of walkers. Further, the evaluation of these excited states requires knowledge of the associated nodal surface, which can become quite complicated when large amplitude vibrations are involved.[2,20,36] The fact that distinct sets of walkers are used to describe each state also makes the evaluation of matrix elements of the Hamiltonian or dipole moment difficult.[70]

To circumvent these challenges, in the present study, we explore an approach in which we use the DMC ground state probability amplitude (GSPA) to generate a set of coordinates, which we then use to calculate the vibrational spectra of ${H_7O_3}^+$, ${H_9O_4}^+$, and their deuterated analogs in a small basis set calculation. The GSPA approach was outlined in a pair of studies on $H_3O_2^-$ and $H_5O_2^+$,[71,72] and has also been applied to calculations of the H_2 stretch frequencies in H_5^+.[73] In this approach, excited states are approximated as products of polynomials that are functions of displacements of internal coordinates, which are obtained from the ground state probability amplitude, and the DMC ground state wave function. This approach has an advantage over large basis set techniques in that the interpretation of the results is simplified by the use of a smaller, carefully constructed basis, which were shown to provide surprisingly accurate results in the earlier studies. In this work, we introduce several extensions to the previously described approaches. The first focuses on improving the description of states with two quanta of vibrational excitation. We test this extension for a series of Morse Oscillators as well as a calculation of the excited state energies of H_3O^+. We also consider general strategies for selecting the internal coordinates on which the approximation is based. Finally, we extend the approach to account for strong coupling of the shared proton stretch to nearby nearly degenerate states. The numerical details of the DMC calculations are provided in Refs. 37 and 74.

3.2 Implementation of the GSPA approach

In a pair of earlier studies, we described an approach for approximating the excited state energies and wave functions based on the ground state probability amplitude obtained using DMC.[71, 72] For the present applications, we developed a slightly modified version of this approach. As in earlier studies, we will use approximate expressions for the excited state wave functions. Since we will be focusing on states with up to two quanta of excitation, these states are denoted as $|\Phi_{n_i=l,n_j=m}\rangle$, where i and j represent the modes that are being excited, and l and m provide the number of quanta of excitation in modes i and j, respectively.

Within this approximation, $|\Phi_{n_i=l,n_j=m}\rangle$ is expressed as

$$|\Phi_{n_i=l,n_j=m}\rangle \approx \mathrm{P}_{i,j}^{(l,m)}(q_i, q_j)\,|\Phi_0\rangle \tag{3.1}$$

where

$$\mathrm{P}_{i,j}^{(l,m)}(q_i, q_j) = \sum_{k=0}^{l}\sum_{k'=0}^{m} c_{i,j}^{(k,k')}(q_i - \langle q_i\rangle)^k (q_j - \langle q_j\rangle)^{k'} \tag{3.2}$$

For states that involve excitation in one mode, the coefficients are determined by the requirement that

$$\langle \Phi_{n_i=l,n_j=0}|\Phi_{n_i=l',n_j=0}\rangle = 0 \tag{3.3}$$

for all $l' < l$. Based on these requirements,

$$\mathrm{P}_{i,j}^{(1,0)}(q_i, q_j) \equiv \mathrm{P}_i^{(1)}(q_i) = q_i - \langle q_i \rangle \tag{3.4}$$

and

$$\mathrm{P}_{i,j}^{(2,0)}(q_i, q_j) \equiv \mathrm{P}_i^{(2)}(q_i) = \frac{-(q_i - \langle q_i \rangle)^2}{\langle (q_i - \langle q_i \rangle)^2 \rangle} + \frac{\langle (q_i - \langle q_i \rangle)^3 \rangle \, (q_i - \langle q_i \rangle)}{\langle (q_i - \langle q_i \rangle)^2 \rangle^2} + 1 \tag{3.5}$$

For states in which $n_i = 1$ and $n_j = 1$,

$$\mathrm{P}_{i,j}^{(1,1)}(q_i, q_j) = (q_i - \langle q_i \rangle)(q_j - \langle q_j \rangle) \tag{3.6}$$

The vibrational modes $\{\mathbf{q}\}$ are formed from linear combinations of $3N-6$ carefully chosen internal coordinates, $\mathbf{r} - \langle \mathbf{r} \rangle$. The transformation matrix that rotates the internal coordinates to q-coordinates is the eigenvectors of the mass-weighted matrix of second moments $\mathbf{M}^{\mathrm{MW}}$, where

$$\mathbf{M}^{\mathrm{MW}} = \mathbf{G}^{-1/2}\mathbf{M}\mathbf{G}^{-1/2} \tag{3.7}$$

$$\mathrm{M}_{ij} = \langle (r_i - \langle r_i \rangle)(r_j - \langle r_j \rangle) \rangle \tag{3.8}$$

and $\mathbf{G}$ in Eq. 3.7 represents the Wilson G-matrix[75] the elements of which are evaluated numerically using

$$\mathrm{G}_{ij} = \left\langle \sum_{k=1}^{3N} \frac{\partial r_i}{\partial x_k} \frac{1}{m_k} \frac{\partial r_j}{\partial x_k} \right\rangle \tag{3.9}$$

Finally, m_k is the atomic mass associated with x_k, and all expectation values are taken over $|\Phi_0\rangle$. It should be noted that based on the above definitions $\langle \mathbf{q} \rangle = 0$, and this definition of the q-coordinates will recover the usual normal mode coordinates in the limit of a harmonic Hamiltonian. The above definitions ensure that the ground state and all of the states with one quantum of excitation are mutually orthogonal as are states with different amounts of excitation in a given mode. Additionally, all excited states are orthogonal to the ground state. On the other hand, excited states are generally not orthogonal to each other. This will become important if we wish to introduce couplings between the approximate excited states.

To calculate the transition energy from the ground state, we need to evaluate

$$E_{n_i,n_j} - E_0 = \left(\langle T\rangle_{i,j}^{(l,m)} - \langle T\rangle_{i,j}^{(0,0)}\right) + \left(\langle V\rangle_{i,j}^{(l,m)} - \langle V\rangle_{i,j}^{(0,0)}\right) \tag{3.10}$$

where for an operator, $A = T$ or V,

$$\langle A\rangle_{i,j}^{(l,m)} = \left\langle \Phi_{n_i=l,n_j=m}\right| A \left|\Phi_{n_i=l,n_j=m}\right\rangle \tag{3.11}$$

Since the potential is a multiplicative operator,

$$\langle V\rangle_{i,j}^{(l,m)} = \frac{\left\langle \left(\mathrm{P}_{i,j}^{(l,m)}\right)^2 V\right\rangle}{\left\langle \left(\mathrm{P}_{i,j}^{(l,m)}\right)^2\right\rangle} \tag{3.12}$$

and the potential energy of each walker is evaluated using the many-body surface reported by Bowman and coworkers.[3]

The evaluation of $\langle T\rangle_{i,j}^{(l,m)} - \langle T\rangle_{i,j}^{(0,0)}$ is more complicated since an ensemble of localized functions in $3N$ dimensions is used to represent $\Phi_0\Psi_T$. While division by Ψ_T is straightforward, differentiation of Φ_0 is not. Rather than trying to differentiate Φ_0 numerically, we turn to insights from the harmonic oscillator expressed in terms of mass weighted coordinates, Q, and their conjugate momentum, P, where

$$\langle n|P^2|n\rangle - \langle 0|P^2|0\rangle = \beta n \tag{3.13}$$

and

$$\langle n|Q^2|n\rangle - \langle 0|Q^2|0\rangle = \frac{n}{\beta} \tag{3.14}$$

Additionally, for the harmonic oscillator,

$$\langle n|T|n\rangle - \langle 0|T|0\rangle = \frac{\beta n}{2} \tag{3.15}$$

When the harmonic Hamiltonian is expressed in mass-weighted coordinates and $\hbar = 1$, $\beta = \omega$.

In the GSPA approach, we use Eq. 3.15 to evaluate the kinetic contribution to the energy, but instead of equating β to the harmonic frequency, we treat $\beta_i^{(\mathrm{GSPA},n)}$ as a parameter, which depends on the number of quanta of excitation in mode i. The expressions for $\beta_i^{(\mathrm{GSPA},n)}$ are evaluated by using relationships between $\langle Q^l\rangle$ and β, which are also based on a harmonic system. Specifically, for transitions to states with one and two quanta of excitation in the ith mode, we use

$$\beta_i^{(\mathrm{GSPA},1)} = \frac{\langle q_i^2\rangle}{\langle q_i^4\rangle - \langle q_i^2\rangle^2} \tag{3.16}$$

and

$$\beta_i^{(\mathrm{GSPA},2)} = \sqrt{\frac{8\,\langle q_i^4\rangle}{\langle q_i^8\rangle - \langle q_i^4\rangle^2}} \tag{3.17}$$

respectively. The above definition of $\beta^{(\mathrm{GSPA},1)}$ has been shown to provide accurate energies for transitions with $\Delta n = 1$ in $H_3O_2{}^-$ and $H_5O_2{}^+$, but it is less accurate for higher levels of vibrational excitation.[71,72] The loss of accuracy with vibrational excitation, and the need for expressions $\beta^{(\mathrm{GSPA})}$ that depend on the number of quanta of excitation, can be traced to the fact that in anharmonic systems most of the anharmonicity is in $\langle T\rangle_n$, while $\langle V\rangle_n$ is much less sensitive to the anharmonicity. For a Morse oscillator, where

$$E_n - E_0 = n\omega - n(n+1)\omega x \tag{3.18}$$

one can show that $\langle V\rangle_n - \langle V\rangle_0 = n\omega/2$, which is the same as the harmonic value, while $\langle T\rangle_n - \langle T\rangle_0 = n\omega/2 - n(n+1)\omega x$.[76] Letting the expression for $\beta_i^{(\mathrm{GSPA},n)}$ depend on the value of n allows us to account for the the higher order terms in $\langle T\rangle$.

To evaluate intensities within the GSPA approach, we also need the matrix elements of the dipole operator, from which we calculate the transition dipole moment. These calculations for $H_7O_3{}^+$ and $H_9O_4{}^+$ are performed using the many-body dipole surface reported by Bowman and coworkers.[3] Following the above discussion,

$$\langle \Phi_{n_i=l,n_j=m}|\,\vec{\mu}\,|\Phi_{n_i=0,n_j=0}\rangle \approx \frac{\left\langle (\mathrm{P}_{i,j}^{(l,m)}\vec{\mu}\right\rangle}{\sqrt{\left\langle \left(\mathrm{P}_{i,j}^{(l,m)}\right)^2\right\rangle}} \tag{3.19}$$

3.3 Introducing Couplings in the GSPA Approach

While the energies obtained by the approach described above provide good approximations to the excited state energies, the excited states themselves are not eigenstates of the vibrational Hamiltonian. To account for the coupling of these zero-order states, we construct a reduced-dimensional Hamiltonian **H** and the corresponding overlap matrix **S**. The diagonal elements of **H** are the transition energies, as described above, and the diagonal elements of **S** are 1. The off-diagonal elements of each matrix are given by

$$\mathrm{S}_{n,n'} = \langle \Phi_{n_i=l,n_j=m}|\Phi_{n'_{i'}=l',n'_{j'}=m'}\rangle = \frac{\left\langle \mathrm{P}_{i,j}^{(l,m)}\mathrm{P}_{i',j'}^{(l',m')}\right\rangle}{\sqrt{\left\langle \left(\mathrm{P}_{i,j}^{(l,m)}\right)^2\right\rangle \left\langle \left(\mathrm{P}_{i',j'}^{(l',m')}\right)^2\right\rangle}} \tag{3.20}$$

$$\mathrm{H}_{n,n'} = \langle \Phi_{n_i=l,n_j=m}|V - \langle V\rangle\,|\Phi_{n'_{i'}=l',n'_{j'}=m'}\rangle = \frac{\left\langle \mathrm{P}_{i,j}^{(l,m)}V\mathrm{P}_{i',j'}^{(l',m')}\right\rangle - \langle V\rangle \left\langle \mathrm{P}_{i,j}^{(l,m)}\mathrm{P}_{i',j'}^{(l',m')}\right\rangle}{\sqrt{\left\langle \left(\mathrm{P}_{i,j}^{(l,m)}\right)^2\right\rangle \left\langle \left(\mathrm{P}_{i',j'}^{(l',m')}\right)^2\right\rangle}} \tag{3.21}$$

The above expression for $H_{n,n'}$ includes only contributions from the potential energy. While there should also be kinetic contributions to these terms, we have found that they are small compared to the contributions from the potential energy.

The energies and wave functions, $|\Phi^{\mathrm{coup}}\rangle$, in the coupled representation can then be obtained by solving the generalized eigenvalue problem

$$\mathbf{H}|\Phi^{\mathrm{coup}}\rangle = E\mathbf{S}|\Phi^{\mathrm{coup}}\rangle \tag{3.22}$$

Using these eigenvectors, we can obtain the intensities of the transitions from the ground state to these mixed states.

3.4 Results and Discussion

The discussion that follows will be divided into several parts. We will start by assessing the numerical accuracy of the expressions for $\beta^{(\mathrm{GSPA},n)}$, which are provided in Eqs. 3.16 and 3.17, by evaluating the excited state energies for a series of Morse oscillators with varying amounts of anharmonicity. We next consider the coordinates that are to be used to describe the protonated water systems and apply the GSPA technique to the calculation of spectra of these ions. We first use the GSPA approach to evaluate the energies of excited states of H_3O^+ with one and two quanta of excitation. These energies are compared to the results of VSCF/VCI calculations based on the same potential surface.[77,78] Using the insights gained from these calculations on H_3O^+, we turn to the calculated spectra of $H_7O_3{}^+$ and $H_9O_4{}^+$ and their deuterated analogs. All reported spectra that are calculated using the GSPA approach have been convoluted with Gaussian functions. The calculated transition energies and intensities between 1000 to 4000 cm^{-1} have been convoluted with Gaussians with $\sigma = 25$ cm^{-1}, while between 200 and 1500 cm^{-1} the calculated transitions have been convoluted with Gaussians with $\sigma = 10$ cm^{-1}. The relative intensity is obtained by normalizing the most intense feature in the displayed spectral region to one.

3.4.1 Evaluation of the Kinetic Energy

The kinetic energy expression used in the GSPA technique is derived from the expressions of expectation values of kinetic energy for the nth state of the one-dimensional Harmonic oscillator, where $\langle T\rangle_n - \langle T\rangle_0 = n\beta/2$. In Eqs. 3.16 and 3.17, we introduced expressions for evaluating $\beta^{(\mathrm{GSPA},n)}$ for $n = 1$ and 2, which can be used to obtain an approximation to the kinetic contribution to the transition energy. To explore the accuracy of this approximation, we use a series of one-dimensional Morse oscillators, for which

$$E_n = \omega(n + 1/2) - \omega x(n + 1/2)^2 \tag{3.23}$$

and the transition energies are described in Eq. 3.18. For this series of Morse oscillators, $\omega =$ 3000 cm^{-1} and ωx ranges from 0 to 500 cm^{-1}, where 500 cm^{-1} is roughly the anharmonicity of the OH stretch in ${H_7O_3}^+$. For this part of the study, we obtain the ground state wave function using a discrete variable representation (DVR) based on an evenly spaced grid[79] consisting of 800 points in $\Delta r = r - r_e$ ranging from -1.00 to 3.00 a_0, or -0.529 to 1.59 Å. We then calculate the energy differences between the states with $n = 1$ or 2 and the ground state using the expressions provided in Eqs. 3.10-3.17.

In Figure 3.1, we compare the results of these calculations using $\beta^{(\mathrm{GSPA},1)}$ (red solid line) and $\beta^{(\mathrm{GSPA},2)}$ (blue solid line) to the energies evaluated using Eq. 3.23 (grey dotted line). The plot on the left shows results for the $\Delta n = 1$ transitions, while results for the $\Delta n = 2$ transitions are shown in the right panel. Consistent with earlier studies,[71] calculating the transition energy to the state with $n = 1$, using $\beta^{(\mathrm{GSPA},1)}$ in the expression for the kinetic energy provides more accurate excited state energies, and the percent error of the calculated transition energy is less than 3% over this range of anharmonicities. This is illustrated by the agreement between the solid red and dotted grey lines in the left panel of this figure. Using $\beta^{(\mathrm{GSPA},2)}$ (results shown with the blue solid line) to calculate the $n = 1$ energies yields much poorer agreement with the expected results (shown with the grey dotted line). When $\beta^{(\mathrm{GSPA},1)}$ is used to evaluate the transition energies to states with $n = 2$, the values are overestimated. This can be seen by comparing the results plotted with the red solid line and the grey dotted line in the right panel of this figure. On the other hand, if we use $\beta^{(\mathrm{GSPA},2)}$ (results shown with the blue solid line) to evaluate the energies of the $\Delta n = 2$ transitions, the error is smaller than 5% over a large range of anharmonicities. Based on these results, we will use the expressions for β provided in Eqs. 3.16 and 3.17 based on the value of Δn in the calculations described below.

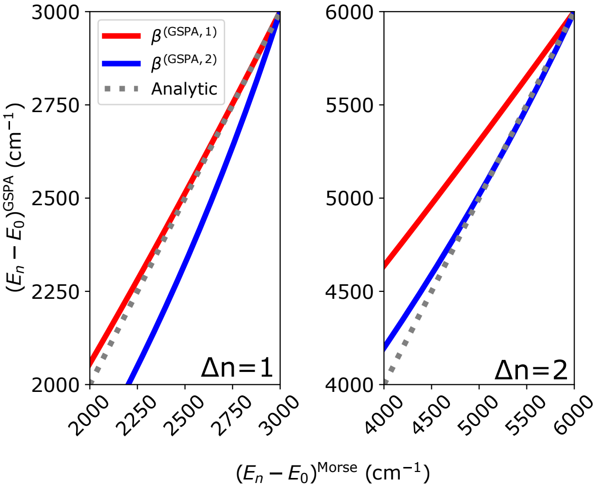

Figure 3.1: Comparison of the transition energies for $\Delta n = 1$ (left) and $\Delta n = 2$ (right) obtained using the GSPA approach with $\beta^{(\mathrm{GSPA,m})}$ defined in Eqs. 3.16 for $m = 1$ (red solid line) and 3.17 for $m = 2$ (blue solid line) to the expected values for Morse oscillators (grey dotted line) with harmonic frequencies of 3000 cm^{-1} and anharmonicities between 1 and 500 cm^{-1}, see Eq. 3.18.

3.4.2 Structure and Internal Coordinates of H_3O^+, $H_7O_3{}^+$, and $H_9O_4{}^+$

The GSPA approach is predicated on finding an appropriate set of internal coordinates as well as a reference structure for evaluating the Cartesian components of the dipole moment. The most important consideration in identifying a reference structure is that it is energetically accessible in the vibrational ground state. It should also reflect the symmetry of the vibrationally averaged structure of the system of interest.[80] In the present study, we are focusing on ions that can be characterized as hydronium bound to two or three water molecules.

In a previous study,[1] we found that, by examining projections of the ground state DMC probability amplitude, $H_7O_3{}^+$ and $H_9O_4{}^+$ display large amplitude motions in various coordinates. Notably, the large amplitude vibrational motions along the umbrella coordinate (γ) of the hydronium core and the rotation of the flanking water monomers lead to a drastic change in overall structure of the cluster. We show projections of the probability amplitude onto the umbrella coordinate in Figure 3.2. These projections illustrate that, with vibrational zero-point energy included, there is equal probability of finding the hydronium core on either side of the heavy-atom plane. Additionally, there is significant amplitude in the transition state structure where the hydronium core is planar. For the flanking water molecules, we show the projection of Ψ^2 onto the C-component of the hydrogen atoms in the flanking water monomers in $H_7O_3{}^+$ and $H_9O_4{}^+$. The C-component is defined as the displacement off of the plane defined by the heavy atoms and is explained in more detail below.

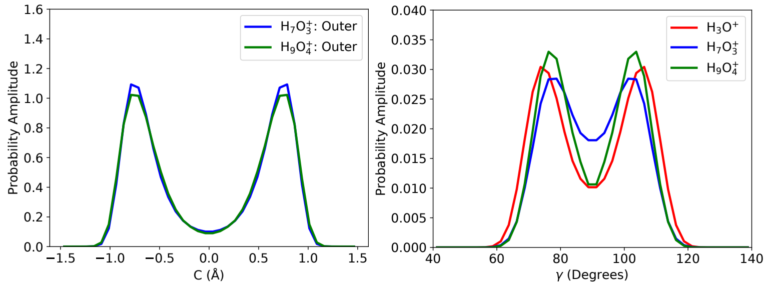

Figure 3.2: (Left) Projection of the probability amplitude (Ψ^2) onto the C component of the hydrogen atoms of the flanking water monomers in $H_7O_3{}^+$(blue) and $H_9O_4{}^+$ (green). The C component is defined as the displacement from the plane defined by the three oxygen atoms in $H_7O_3{}^+$ and the three outer oxygen atoms in $H_9O_4{}^+$shown in Figure 3.3. (Right) Projection of the probability amplitude onto the umbrella coordinate γ for H_3O^+ (red), $H_7O_3{}^+$ (blue), and $H_9O_4{}^+$ (green).[1]

Because of the free rotation of the outer water monomers and the delocalization of the wave function across the hydronium umbrella coordinate, we choose for the reference structure a vibrationally-averaged one in which the hydronium core is planar, the oxygen atoms are in the same plane as the hydronium core, and the water molecules lie in planes that are perpendicular to the plane that contains the oxygen atoms. These reference structures are illustrated in the top panels of Figure 3.3. With the reference structure defined, we need a way to rotate an arbitrary structure to this reference structure. With the large amplitude umbrella motions of the hydrogen atoms in the hydronium core and the large amplitude rotations of the outer water molecules, we choose to base this on the coordinates of the oxygen atoms and use standard algorithms[81,82] to rotate arbitrary structures to the reference geometry.

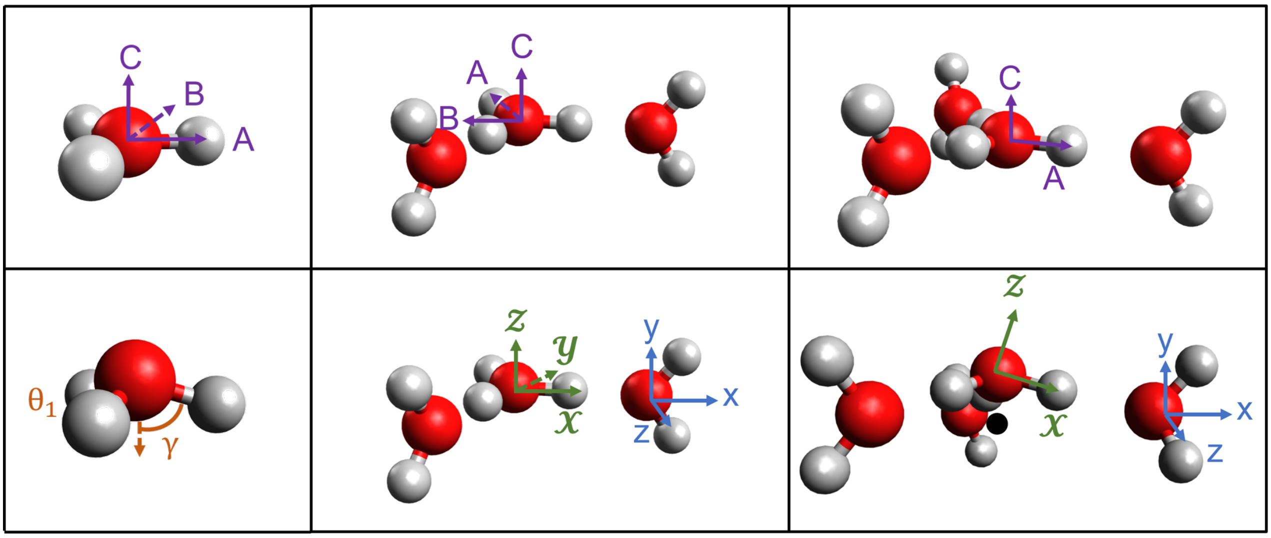

Figure 3.3: (Top) Reference structures for H_3O^+ (left), $H_7O_3{}^+$ (middle) and $H_9O_4{}^+$ (right) used in this study. The heavy atoms and the hydrogen atoms in the hydronium core are all coplanar. Additionally, in $H_7O_3{}^+$ and $H_9O_4{}^+$, the outer water molecules lie in planes that are perpendicular to the heavy atom plane. The purple A, B and C axes are used to define the modified Eckart frame described in the text. (Bottom left) The umbrella coordinate (γ) and one of the HOH angles (θ_1) are defined for H_3O^+. (Bottom Middle and Right) The axis systems used to define the orientation of the outer water molecules (see text for details), are shown in green and blue. The black circle in the lower right panel shows the point in the plane containing the three outer oxygen atoms that is closest to the central oxygen atom, and is used in the definition of the $\mathcal{XZ}$ plane.

With the reference structure determined, we define internal coordinates. Since the GSPA approximation is based on a harmonic description of molecular vibrations, in selecting coordinates, we aim to identify ones for which the projections of Φ_0^2 onto the chosen coordinates are roughly Gaussian. This criterion is not always achievable, particularly for some of the large amplitude motions that correspond to the umbrella motion of the hydronium core and the hindered rotation of the outer water molecules. In addition, the coordinates are chosen such that we can construct symmetry adapted linear combinations of the coordinates that reflect the symmetry of the reference structure of the ion.

If we consider H_3O^+, three of the six internal coordinates are the three OH bond lengths. In the planar reference structure there is redundancy in the HOH angles. We use two linear combinations of these angles that transform as the E irreducible representation under the D_{3h} symmetry group, $2\theta_1 - \theta_2 - \theta_3$ and $\theta_2 - \theta_3$. The sixth coordinate, γ, is an umbrella coordinate, which is the angle between a vector shown in the lower panel of Figure 3.3 that has its origin at the oxygen atom and passes through the center of a triangle, which is defined by the vertices of unit vectors along each of the three OH bonds, and a second vector that lies along one of the OH bonds. This definition ensures that the value of the umbrella coordinate is independent of the OH bond that is used to define it.

Defining the coordinates for ${H_7O_3}^+$ and ${H_9O_4}^+$ requires an overall axis system (expressed as A, B, C, and shown in purple in the upper panels of Figure 3.3). To define these axes, we use a modified Eckart frame. In ${H_7O_3}^+$, this frame is based on the coordinates of the three oxygen atoms, while in ${H_9O_4}^+$ we use the three outer oxygen atoms to define the Eckart frame.[81,82] Once the reference structure has been rotated to a principle axis frame, with the origin of the axis system at the center of mass of the three oxygen atoms that are used to define this axis system, these three oxygen atoms all lie in the AB-plane. In ${H_7O_3}^+$, the central oxygen atom is on the A-axis, while in ${H_9O_4}^+$ one of the external oxygen atoms is on the A-axis. For ${H_7O_3}^+$ this is the same as the axis system that is used to define the components of the dipole moment surface, while for ${H_9O_4}^+$, the coordinate systems differs due to the exclusion of the fourth oxygen atom from the definition of the modified Eckart frame.

We then define the internal coordinates of the constituent water and hydronium molecules. Each outer water molecule is described by two OH bond lengths and one HOH angle. The three OH bonds in the hydronium core are described in terms of three spherical polar coordinates, with θ providing the angle between the OH bond and the $C-$axis, while ϕ provides the rotation of the OH vector off of the $A-$axis in the AB plane. For the free OH in the hydronium core in $H_7O_3{}^+$, we replace ϕ with ϕ', which is the the difference between the two $H_{\mathrm{Free}}OH_{\mathrm{Bound}}$ angles, as ϕ becomes ill-defined when θ approaches 0° and 180°.

The orientations of the outer water molecules are each defined using three Euler angles. For both $H_7O_3{}^+$ and $H_9O_4{}^+$, the axes that describe the orientation (x, y, z) of the water molecules are defined with the x-axis pointing along the bisector of the two OH vectors, and the z-axis as the cross product between the two OH vectors. For $H_7O_3{}^+$, three Euler angles define the rotation between the axis system for the water molecule of interest (x, y, z) and one $(\mathcal{X}, \mathcal{Y}, \mathcal{Z})$ in which the OO vector from the central oxygen atom to the oxygen atom in the water molecule of interest lies along the $\mathcal{X}$-axis, and the third oxygen atom lies in the $\mathcal{XY}$ plane, with the direction of the $\mathcal{Z}$-axis being determined by the cross product of the OO vectors from the central to the outer oxygen atoms. In this way, the $\mathcal{Z}$-axis is the same for both water molecules, while the orientation of the $\mathcal{X}$ and $\mathcal{Y}$ axes is determined by which water molecule is being considered (See Figure 3.3). Likewise for $H_9O_4{}^+$, the three Euler angles relate the axis system for the water molecule of interest to an axis system where the $\mathcal{X}$-axis points along the OO vector from the central oxygen atom to the oxygen atom in the water molecule being considered. The $\mathcal{XZ}$ plane contains these two oxygen atoms as well as the point on the AB plane that is closest to the central oxygen atom. The $\mathcal{Y}$-axis is defined by $\mathcal{Z} \times \mathcal{X}$ (See Figure 3.3).

Finally, we use the OO distances and the OOO bending coordinate to describe the relative distances between the hydronium and the outer water molecules in $H_7O_3{}^+$. For $H_9O_4{}^+$, we use the three outer OO distances as well as the three Cartesian displacements of the center of mass of the hydroninum core based on the modified Eckart axis system described above. For the purposes of assignments, the C-axis is defined as the one that is perpendicular to the plane defined by the oxygen atoms.

3.4.3 Application to H_3O^+

As a test of the approximation to the expectation value of the kinetic energy described above, we apply the GSPA approach to the calculation of the transition energies in H_3O^+, where the results can be compared to the results of VSCF/VCI calculations by Huang *et al.* using the same potential surface.[77,78] We also compare to the results of VPT2 calculations. The VPT2 energies were obtained at the MP2/aug-cc-pVTZ level of theory/basis as implemented in Gaussian 16.[83]

Table 3.1: Calculated Vibrational Transition Energies of H_3O^+ (cm^{-1})

State	Sym	Assignment	GSPA	VSCF/VCI^a	VPT2^b
(0,0,0,0)	A_1'	Ground State	0	0/38.6	0
(0,1,0,0)	E'	Antisymmetric OH Stretch	3535/3535	3545	3502
(1,0,0,0)	A_1'	Symmetric OH Stretch	3406	3416	3410
(0,0,1,0)	E'	H_3O^+ Bend	1617/1617	1623	1625
(0,0,0,1)	A_2''	Umbrella	151	573/945	734
(0,2,0,0)	A_1'		6983	6972	6879
(0,2,0,0)	E'		6998/7031	7068	6944
(2,0,0,0)	A_1'		6746	6748	6768
(0,0,2,0)	A_1'		3212	3211	3211
(0,0,2,0)	E'		3215/3233	3233	3236
(0,0,0,2)	A_1'		705	1462/2030	1290

[a] Based on HCB-4 potential.[77,78]
[b] MP2/aug-cc-pVTZ.

The results of the calculations are reported in Table 3.1. Focusing on the states with one quantum of excitation in one of the vibrational modes, the states with excitation in the OH stretches or HOH bends obtained using the GSPA approach are in very good agreement with the results of VSCF/VCI calculations. In addition to reporting the excited state energy and assignment, we provide the symmetry of the excited state based on the D_{3d} reference structure. The energies that were calculated using the GSPA approximation reflect the expected degeneracies of the antisymmetric OH stretch and the HOH bend. While the five high-frequency vibrations are well-described by this approach, the frequency of the fundamental in the umbrella vibration is not in as good agreement with the VSCF/VCI values. Due to the double well character of the potential along the umbrella coordinate, the state with a node at the planar reference structure will correspond to the upper level of the ground-state tunneling doublet and not a proper first excited state in this vibration. The measured ground state tunneling splitting in H_3O^+ is 55 cm^{-1},[84] and calculations based on this potential yield a ground state tunneling splitting of 38.6 cm^{-1}.[78]

When we compare the calculated energy of the state with two quanta of excitation in the umbrella vibration to that obtained from a VPT2 calculation, we find that the $n = 2$ energy from the GSPA calculation is close to the calculated energy of the state with one quantum of excitation. It is also close to the average energy of the tunneling split $n = 1$ states obtained from the VSCF/VCI calculation (573 and 945 cm^{-1}). If we recalculate the energy of the $n = 1$ state using $\beta^{(\mathrm{GSPA},2)}$ in the evaluation of the kinetic contribution, the calculated energy is 556 cm^{-1}, which is 17 cm^{-1} smaller than the energy of the lower energy $n = 1$ state, based on the VSCF/VCI calculation. Clearly, the umbrella vibration is a challenging one to describe using the GSPA approach, which is based on a harmonic treatment of molecular vibrations about a planar reference structure, and we are encouraged by the fact that we can obtain a reasonably good description of this motion in H_3O^+.

When we compare the energies of the states with two quanta of excitation to those obtained using VPT2 and VSCF/VCI energies, the agreement remains good for all but the umbrella vibration. In the case of the antisymmetric stretch and bend, which have E' symmetry, the states with $n = 2$ will correspond to three transitions, two of which are degenerate, and one with A' symmetry. The energies of the overtones in the OH stretch and the HOH bend with A' symmetry are in very good agreement with the VSCF/VCI results, further validating the expressions for $\beta^{(2,\mathrm{GSPA})}$ in Eq. 3.17. On the other hand, for the pair of states with E' symmetry, there is a notable difference between the two calculated energies, with the higher energy one being in better agreement with the VSCF/VCI results. The loss of degeneracy for the overtones with E' symmetry reflects, in part, the fact that the first value is treated as a state with two quanta in one of the two degenerate vibrations, while the second value is obtained by putting one quantum in each of the two degenerate vibrations. Based on these comparisons, we find that the GSPA technique also does a good job of describing the overtones of the stretches and bends in hydronium, although some care should be taken in handling degenerate vibrations. Additionally, the good agreement with VSCF/VCI results for states with one quantum in each of two vibrations validates our definition of the energies of these excited states.

3.4.4 Examining the Vibrational Spectrum of $H_7O_3^+$and $H_9O_4^+$

The richest region of the spectra for $H_7O_3^+$ and $H_9O_4^+$ is the region that contains transitions to $n = 1$ levels of the OH stretches and the HOH bend (i.e. the 1000-4000 cm^{-1} region). As can be seen in the black traces in Figure 3.4, this region is characterized by intense features near the expected location of the fundamental in the shared proton stretch, which is near 2100 cm^{-1} in $H_7O_3^+$and 2600 cm^{-1} in $H_9O_4^+$. There are several narrow peaks near 3500 cm^{-1}, where the OH stretch fundamental in water is expected, as well as a series of less intense peaks at lower frequency. Except for the region near the transition to the $n = 1$ state in the shared proton stretch, the measured spectra of $H_7O_3^+$ and $H_9O_4^+$ appear very similar to each other. The primary difference between the spectra for $H_7O_3^+$ and $D_7O_3^+$ and between $H_9O_4^+$ and $D_9O_4^+$ can be accounted for by the factor of $\sqrt{2}$ difference between frequencies of the OH stretch and HOH bend vibrations involving deuterium compared to those involving hydrogen. The results of the GSPA approximation are shown with blue sticks in the upper panel for each ion in Figure 3.4. The peaks in the calculated spectra are labeled, and the corresponding energies and assignments are provided in Tables 3.7-3.10. The Th and Rh labels are used to denote transitions in $H_9O_4^+$ and $H_7O_3^+$, respectively, while Td and Rd are used to refer to peaks in the spectra of the deuterated forms of these ions. For comparison, we also provide the VSCF/VCI spectra, which were reported by Yu

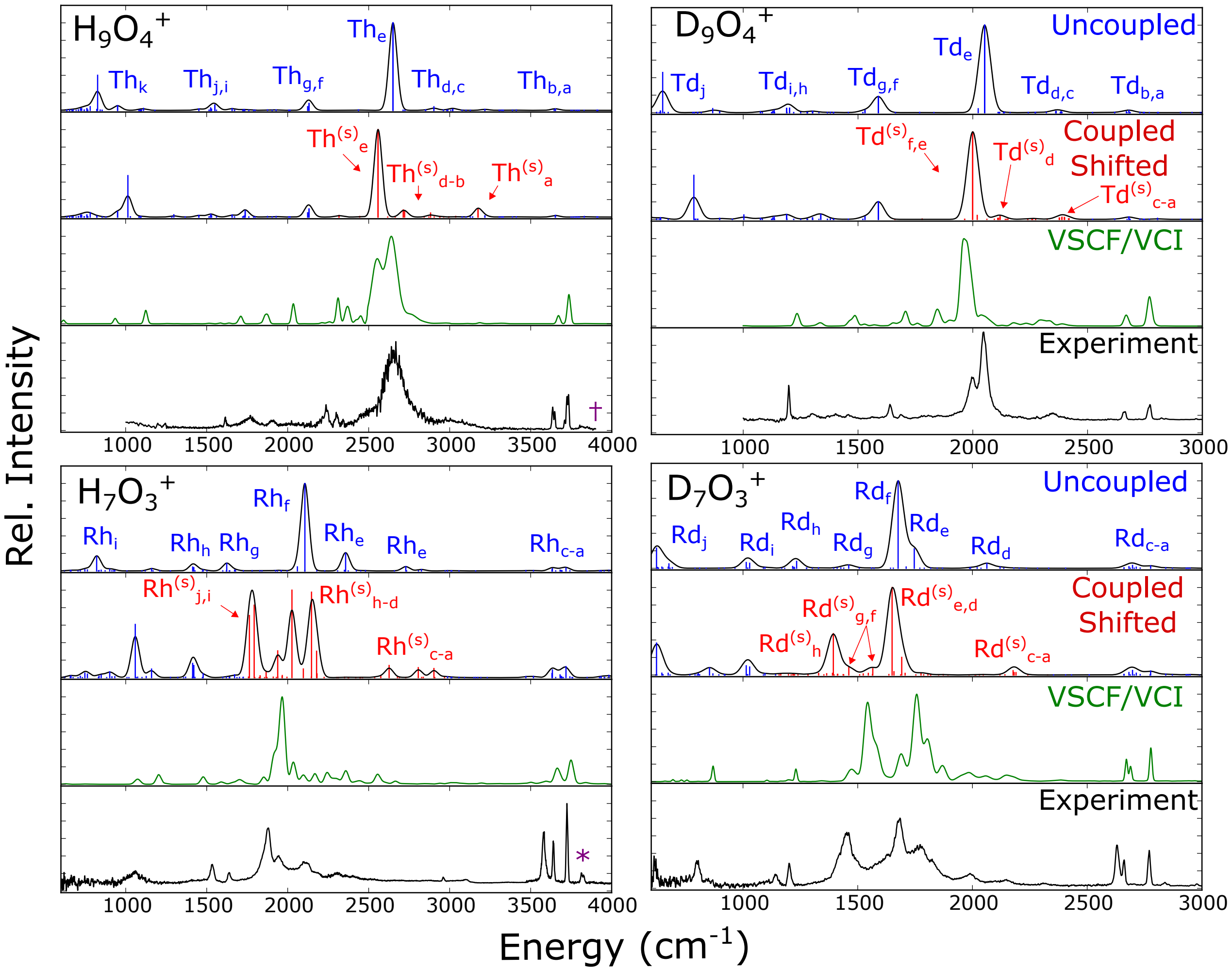

Figure 3.4: Comparison of the uncoupled (blue sticks), coupled and shifted (red sticks), VSCF/VCI[2,3] (green), and measured spectra[2,4] (black) of $H_9O_4^+$ (top left), $D_9O_4^+$ (top right) $H_7O_3^+$ (bottom left), $D_7O_3^+$ (bottom right). In these spectra, the Th and Rh labels are used to denote transitions in $H_9O_4^+$ and $H_7O_3^+$, respectively, while Td and Rd are used to refer to peaks in the spectra of the deuterated forms of these ions. The purple $*$ and † identify transitions in $H_7O_3^+$ and $H_9O_4^+$, which were assigned by the authors to combination transitions involving the outer water OH stretches and the torsion of the water molecules. Descriptions of the states accessed by labeled uncoupled transitions in the GSPA spectra are provided in Tables 3.7-3.10, and the coupled shifted transitions are provided in Tables 3.11-3.14.

and Bowman, green traces in Figure 3.4.[2,3] Overall, the spectra calculated using the GSPA approach, shown in red, are in good agreement with both the spectra calculated using the VSCF/VCI with the same potential surface and the measured spectra.

Free OH Stretching Vibrations

Table 3.2: Calculated GSPA, VSCF/VCI and Measured Transitions in the Outer OH Stretch Region for $H_7O_3{}^+$ (cm^{-1})

GSPA	VSCF/VCI[a]	Measured[a]	Assignment[a]
3769, 3772, 3786, 3790,	-	3814, 3828	H_2O antisym. stretch + H_2O torsion
3761	3748	3726	Outer water OH antisym. H_2O stretch
3632	3658	3640	Outer water OH sym. H_2O stretch
3634	3664	3580	Hydronium free OH stretch

[a] Ref. 2 .

The higher frequency end of this region of the measured spectrum, shown in black traces in Figure 3.4, is characterized by a series of narrow peaks. In earlier studies, these peaks were assigned to transitions to states with one quantum in the OH or OD stretches in the flanking water molecules or the free OH stretch on the hydronium core in $H_7O_3{}^+$. To facilitate the comparison between calculated and measured spectra, the calculated frequencies and intensities of these transitions are also reported in Tables 3.2 and 3.3. As can be seen, the GSPA approach generally provides energies that are within 30 cm^{-1} of both the measured values and those obtained from VSCF/VCI calculations by Yu and Bowman.[2,4] These differences are consistent with the differences between the GSPA approach and the results of MCTDH calculations for $H_5O_2{}^+$,[62,72] the differences between the GSPA and VSCF/VCI results for $H_3O_2^-$,[71] and the comparisons for H_3O^+. The only exception is the transition in $H_7O_3{}^+$ that has been assigned to the free OH stretch in the hydronium core. Both the VSCF/VCI and GSPA approaches show larger deviations from the measured position of this transition compared to the other OH stretch transitions in this region of the spectrum. The measured spectrum of $H_7O_3{}^+$ is obtained by monitoring the loss of the tag molecule (M) from M·$H_7O_3{}^+$, where the tag has been shown to attach to the free hydrogen atom in the hydronium core. Recent experimental studies showed that this is the vibration whose frequency is most sensitive to the strength of the interaction with the tag. VPT2 calculations, which were performed as part of that study, showed a shift in the anharmonic frequency of this OH stretch of 90 cm^{-1} when it is bound to D_2 and a 50 cm^{-1} shift when the OD bond in $D_7O_3{}^+$ is bound to D_2.[63]

Table 3.3: Calculated GSPA, VSCF/VCI and Measured Transitions in the Outer OH Stretch Region for $H_9O_4{}^+$ (cm^{-1})

GSPA	VSCF/VCI[a]	Measured[a]	Assignment[a]
3757, 3759, 3759, 3769, 3775, 3782, 3786, 3790, 3800	-	3823,3803	H_2O antisym. stretch + H_2O torsion
3733, 3762	3734	3733	Outer water OH antisym. H_2O stretch
-	-	3724	Tagged outer water OH antisym. H_2O stretch
3652,3694	3670	3648	Outer water OH sym. H_2O stretch
-	-	3636	Tagged outer water OH sym. H_2O stretch

[a] Ref. 4 .

Further examination of the fundamental frequencies and intensities of the OH stretching vibrations in $H_7O_3{}^+$ and $H_9O_4{}^+$, reported in Tables 3.4 and 3.5, shows that the fundamental transition of the antisymmetric stretch of the water molecules does not carry any intensity, and the fundamental transition of the in-phase combination of the OH symmetric stretches in $H_9O_4{}^+$ is also dark. The lack of intensity in the fundamental in the symmetric stretch can be anticipated from the average symmetry of the ion. On the other hand, the lack of intensity of the antisymmetric water OH stretch is somewhat surprising, and was not anticipated by previous VSCF/VCI studies.[2–4,65] Further consideration of this vibration shows that in simpler ion-water complexes, e.g. Li^+OH_2, in which the cation binds along the C_2 axis of the water molecule, the antisymmetric OH stretch is associated with $\Delta K = 1$, or a change in the number of quanta of excitation in the motion associated with rotation of the water molecule about its symmetry axis.[85] Depending on the size of the barrier for internal rotation of the flanking water molecules, these transitions will either access a $\Delta K = 1$ transition or access the upper level in the tunneling doublet for the state with one quantum of excitation in both the OH stretch and the rotation of the water molecule about its symmetry axis. Previous analyses of the ground state probability amplitudes for $H_7O_3{}^+$ and $H_9O_4{}^+$ showed large amplitude rotation of the flanking water molecules about this axis, which would be consistent with these levels being energetically split by a small tunneling splitting.[1] This rotational motion was not included in VSCF/VCI calculations, which is why these calculations anticipated intensity in the transitions involving the outer water molecules. While this tunneling splitting is not resolved in the experiment, the spectra of both $H_7O_3{}^+$ and $H_9O_4{}^+$ contain features which have been assigned to excitation to states that have a quantum of excitation in both the antisymmetric OH stretch and in this torsion motion.[58] These transitions are indicated with the purple $*$ and † in the measured spectra in Figure 3.4, and we report the calculated energies for these transitions based on the GSPA approach in Tables 3.2 and 3.3.

Umbrella Vibration

The fundamental in the umbrella motion lies at the other end of this spectral range. As noted for hydronium, the large amplitude nature of this mode, which samples a double well potential with a small barrier, makes it a challenging one for the GSPA approach. For both $H_7O_3{}^+$ and $H_9O_4{}^+$, the frequency of this vibration calculated using the GSPA approach is roughly 200 cm^{-1} smaller than the observed transition frequency, which is near 1000 cm^{-1} for both of these ions.[2,4,59] The underestimation of the frequency of this vibration is consistent with our findings for H_3O^+. Like H_3O^+, the umbrella motions in $H_7O_3{}^+$ and $H_9O_4{}^+$ both sample a double-well potential, and for both ions the projection of the ground state probability amplitude onto this coordinate is bimodal.[1] This makes the GSPA approach, which is based on properties of harmonic oscillators, less effective for this vibration. The underestimation of the frequency of the umbrella mode will also affect the energies of states that have one quantum of excitation in the umbrella along with one quantum of excitation of one of the higher frequency vibrations. To account for this, in the spectra that are identified as Coupled Shifted in Figure 3.4, we have shifted the transition energies of the states that involve the umbrella mode by the error in the calculated transition energy to the $n = 1$ level prior to diagonalization of the Hamiltonian matrix. The values of these shifts are provided in Table 3.6. Because the frequency of the umbrella in $D_9O_4^+$ has not been reported, the shift for this ion was evaluated based on the shifts for the other three species. A comparison of the calculated GSPA spectrum with and without this shift is provided in Figure 3.6.

Shared Proton Stretch Vibration

The most interesting region of the spectrum includes the fundamental in the shared proton stretch. In the absence of state mixing, the GSPA energies of the $\Delta n = 1$ transitions in the shared proton stretch vibration for $H_9O_4^+$ and $D_9O_4^+$ ($\mathrm{Th_e}$ and $\mathrm{Td_e}$) are in excellent agreement with experiment. In the case of $H_7O_3^+$ and $D_7O_3^+$, the energies of the $\Delta n = 1$ transition in the shared proton stretch ($\mathrm{Rh_f}$ and $\mathrm{Rd_f}$) are close to the centroids of the experimental signal in the shared proton region.[63] While the agreement is generally very good, the measured peaks in $H_7O_3^+$, $D_7O_3^+$, $H_9O_4^+$, and $D_9O_4^+$ in this region have been attributed to states of mixed character. The states that are nearly degenerate to the shared proton stretch undergo intensity borrowing, leading to the observed broad and structured features seen in the experimental traces shown in Figure 3.4.[2–4,63,67]

To account for this state mixing, we explore how the spectra in the region of the fundamental in the shared proton stretch changes if we introduce couplings among the $n = 1$ states in the shared proton stretch and energetically nearby zero-order states. We can then examine the contributions from the zero-order vibrational states to the excited state of interest by calculating the coefficients (C_n) of the eigenvectors of the reduced dimensional Hamiltonian matrix obtained from solving the generalized eigenvalue problem (Eq. 3.22). The resulting spectra, obtained by considering states with two or fewer quanta of excitation and with energies that are within 600 cm^{-1} of the anharmonic frequency of the shared proton stretch in $H_7O_3{}^+$ and $D_7O_3{}^+$ and within 400 cm^{-1} of the shared proton stretch in $H_9O_4{}^+$and $D_9O_4{}^+$, are shown with red sticks in the middle panels of Figure 3.4. Transitions to states that were not included in this analysis are shown with blue sticks in these panels. The transitions are identified with the (s) superscript to reflect the fact that we have introduced a shift in the frequency of the umbrella vibration prior to diagonalizing the Hamiltonian matrix. The associated frequency and decomposition in terms of zero-order states are provided in Tables 3.11-3.14. The assignments of the transitions in the uncoupled region of the spectrum are provided in Tables 3.7-3.10.

The small basis representation of the Hamiltonian yields a spectrum that is in good agreement with both the measured spectrum and the spectrum obtained from a VSCF/VCI calculation, which employed a substantially larger basis. The use of a small basis allows us to decompose the contributions to the various features in the spectrum. In fact, the state-mixing treatment used in the GSPA approach is similar to the approach that is used to account for near-degeneracies in vibrational perturbation theory calculations. In an earlier study, we used VPT2 to explore mode mixing in $H_7O_3{}^+$, $D_7O_3{}^+$ and $H_9O_4{}^+$, where the VPT2 was based on an expansion of the Hamiltonian in internal coordinates.[1,68] The results of that study are summarized in Tables 3.19-3.21 to aid in the discussion that follows.

We begin by considering the results of the GSPA calculations of the spectra for $H_9O_4{}^+$ and $D_9O_4{}^+$. For these ions, the introduction of state mixing leads to subtle changes in the spectral envelope. The most significant change is that the peak that corresponds to the fundamental in the antisymmetric shared proton stretch is shifted to the red in both systems. These shifts result from mixing of the states with one quantum of excitation in the shared proton stretch and states with one quantum of excitation in both the shared proton stretch and the OO stretch. While these shifts lead to poorer agreement with the measured spectrum, the peak that is assigned to the transition to the state with one quantum of excitation in the shared proton stretch in $D_9O_4{}^+$ becomes closer to the position of the corresponding peak in the VSCF/VCI spectrum.

In addition, the transitions identified as $\mathrm{Th}^{(s)}_{\mathrm{a-d}}$ and $\mathrm{Td}^{(s)}_{\mathrm{a-d}}$ gain intensity and better reproduce the corresponding features in the measured spectrum of $H_9O_4{}^+$ near 3000 cm^{-1} and the feature near 2350 cm^{-1} in calculated spectrum for $D_9O_4{}^+$. These peaks have been assigned to transitions to states with one quantum of excitation in the shared proton stretch and one quantum in the corresponding OO stretch,[4] which is consistent with the decomposition of the GSPA states that are accessed by these transition (see Tables 3.11 and 3.12).

While the main features in this spectral region are reproduced by the coupled GSPA calculation, the widths of some of the peaks are not. The breadth of the peak near 2600 cm^{-1} in $H_9O_4{}^+$ suggests couplings to energetically proximal states, many of which involve more than two quanta of excitation. The large density of vibrational states at this energy makes it impossible to reproduce the breadth of this feature using a method that focuses on states with only one or two quanta of vibrational excitation. For this reason, as we consider the results of the GSPA calculations we focus on the position of this transition, rather than the width of the feature. As noted, the position of these features are generally in very good agreement with previous VSCF/VCI calculations despite the much smaller basis used in the GSPA approach.

We next turn our attention to $H_7O_3{}^+$ and $D_7O_3{}^+$. By comparison to the corresponding spectra for $H_9O_4{}^+$ and $D_9O_4{}^+$, the region of the spectrum that has been assigned to transitions to the $n = 1$ state in the shared proton stretch in $H_7O_3{}^+$ and $D_7O_3{}^+$ contains significantly more structure. This has been attributed to couplings between this state and states with two quanta of excitation in lower frequency modes.[2,63,67] In contrast to the breadth of the shared proton stretch feature in the spectrum for $H_9O_4{}^+$, this is an effect that should be accessible by the GSPA approach.

When we introduce state mixing in the GSPA calculation, the resulting spectra undergo dramatic changes in the region where the transition to the state with one quantum of excitation in the shared proton stretch had been in the uncoupled spectrum ($\mathrm{Rh_f}$ and $\mathrm{Rd_f}$ in the blue trace in Figure 3.4). Additionally the band profiles for $H_7O_3{}^+$ and $D_7O_3{}^+$ have qualitatively different shapes. In the case of $H_7O_3{}^+$, the intensity spans from 1760 to 2180 cm^{-1}, while it spans from 1400 to 1700 cm^{-1} in $D_7O_3{}^+$. Qualitatively, this increase in the number of transitions that carry significant intensity correlates to the features in the measured and VSCF/VCI spectra. One of the the advantages of the GSPA approach is that it employs a small basis, making the interpretation of the zero-order states that make up the states that are accessed in these transitions straightforward to identify, and these decompositions for $H_7O_3{}^+$ and $D_7O_3{}^+$ are summarized in Tables 3.13 and 3.14. Examination of these results shows that the most intense features of the calculated GSPA spectrum are composed of states with two quanta of excitation in combinations of the OO stretch, H_3O^+ HOH bends, the umbrella mode, and the hindered rotation of the hydronium core.

Intuitively, the transfer of a proton from hydronium to an acceptor water molecule requires deformations of the water cluster. This in turn involves motions such as the OO stretch as well as the HOH angles in both hydronium and water.[1,4,59,86] Likewise, motions that break the hydrogen bond network through rotation of the hydronium core affect the potential energy surface along the shared proton stretch coordinate. These changes in the potential landscape with proton transfer result in the large couplings between the excited states of $H_7O_3{}^+$ that involve these motions. These large couplings provide the source of the large changes in the spectra when coupling is introduced in the GSPA calculation. The decomposition of the eigenvectors of the degenerate VPT2 calculations,[1,68] which are provided in Tables 3.19 and 3.20, identify similar mixing patterns to those identified from the GSPA approach.

Turning our attention to the comparison of both the measured and calculated spectra of $H_7O_3{}^+$ with $D_7O_3{}^+$, we note significant differences. The change in the structure of the spectrum upon deuteration of $H_7O_3{}^+$ has been discussed previously,[2,63,67] and it reflects the fact that the energies of the zero-order states that are strongly coupled to the shared proton stretch are each shifted by different amounts. Additionally, the smaller amplitude OD vibrations, compared to the OH vibrations, leads to smaller couplings between the various zero-order states when we allow these states to mix. Similar considerations explain the large difference in the structure of the most intense features in the spectra of $H_9O_4{}^+$ and $H_7O_3{}^+$. The couplings that result in the more structured feature in $H_7O_3{}^+$ and $D_7O_3{}^+$ are also present in $H_9O_4{}^+$ and $D_9O_4{}^+$. The smaller amplitude motion of the shared proton stretch in $H_9O_4{}^+$ decreases the magnitude of these couplings. More importantly, though, the higher frequency of the shared proton stretch vibration in $H_9O_4{}^+$ brings it out of resonance with the states with two quanta of excitation in lower frequency vibrations that contribute to the shared proton stretch feature in $H_7O_3{}^+$.

Low Frequency Vibrations

Finally, we consider the low frequency (200-800 cm^{-1}) region of the spectrum reported by Asmis and coworkers.[5] This region of the spectrum provides direct access to the motions that are mixed with the shared proton stretch in the higher energy regions of the spectrum. In the GSPA approach the coordinates are developed from the ground state wave function, and as a result, the calculated energies capture the anharmonicity of the potential. This allows us to obtain a good description of this spectral region, which is difficult to study using VPT2 and other approaches that are based on a normal mode Hamiltonian.

The calculated and measured spectra for $H_7O_3{}^+$ and $H_9O_4{}^+$ are shown in blue and black, respectively, in Figure 3.5. We use the (f) superscript to indicate that these labeled transitions lie in the far-IR region. In the measured spectrum, the low frequency regions of $H_7O_3{}^+$ and $H_9O_4{}^+$ contain peaks at similar frequencies. We attribute many of the features of both spectra to analogous low frequency vibrational motions (see Table 3.22). There are two intense features in this region of the $H_7O_3{}^+$ and $H_9O_4{}^+$ spectrum. Based on the GSPA approach, the lower energy feature is assigned to the fundamental transition in the in-phase outer water rock ($\mathrm{Rh}_\mathrm{d}^{(\mathrm{f})}$ and $\mathrm{Th}_\mathrm{d}^{(\mathrm{f})}$) for both $H_7O_3{}^+$ and $H_9O_4{}^+$. The higher energy feature is assigned to the antisymmetric OO stretch in $H_7O_3{}^+$, and the two degenerate antisymmetric OO stretches in $H_9O_4{}^+$ ($\mathrm{Rh}_\mathrm{c}^{(\mathrm{f})}$ and $\mathrm{Th}_\mathrm{c}^{(\mathrm{f})}$).

Based on quasiclassical calculations of $H_7O_3{}^+$, the lower energy feature at 234 cm^{-1} was assigned to be the outer water wag, and the higher energy feature at 344 cm^{-1} was assigned

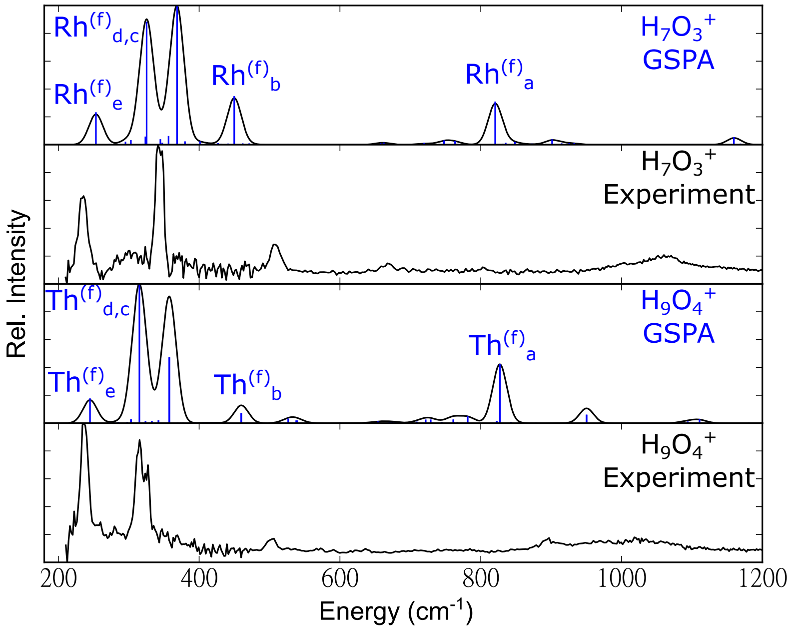

Figure 3.5: Calculated uncoupled GSPA spectrum (blue sticks) compared with experiment[5] (black) for $H_7O_3^+$ and $H_9O_4^+$. The assignments of the labeled transitions are provided in Table 3.22. In these spectra, the Th and Rh labels are used to denote transitions in $H_9O_4^+$ and $H_7O_3^+$, respectively.

to be the symmetric OO stretch. For $H_9O_4{}^+$, the lower energy feature was assigned to the outer water wag, and the higher energy feature was assigned to both the symmetric and antisymmetric OO stretch. The peak at approximately 500 cm^{-1}, which in previous work was assigned as a combination of low frequency modes,[5] is assigned using the GSPA approach as an outer water wag overtone transition in $H_7O_3{}^+$ and two degenerate outer water wag combinations in $H_9O_4{}^+$ ($\mathrm{Rh}_\mathrm{b}^{(\mathrm{f})}$ and $\mathrm{Th}_\mathrm{b}^{(\mathrm{f})}$). The good agreement between the GSPA results and the measured spectra in this region illustrates the power of the GSPA approach for describing the low-energy region of the spectra where the use of curvilinear coordinates is essential, while the low density of vibrational states results in little mixing among the carefully constructed zero-order states developed in this approach.

3.5 Conclusions

In this work, we extended the previously developed GSPA approach[71,72] to allow for more accurate descriptions of the energies of states with two quanta of excitation, provided better descriptions of coordinates, and introduced coupling between zero order states. This allowed us to exploit the rich structural and physical information contained in the DMC ground state probability amplitude of $H_7O_3{}^+$ and $H_9O_4{}^+$, as well as their deuterated analogs, to develop a compact basis set that can be used to calculate the spectra for these ions.

In the absence of state mixing, the GSPA approach allows us to assign many of the features in the spectra of these ions. State mixing becomes essential to explain the region of the spectrum near the $\Delta n = 1$ transition in the shared proton stretch. By allowing states with up to two quanta of excitation to mix, we obtain spectra that are in generally good agreement with the measured spectra for $H_7O_3{}^+$ and $D_7O_3{}^+$. While there are clear differences between the measured and calculated spectra in the region of the transition to the $n = 1$ state of the shared proton stretch, the agreement of the measured spectra with the spectra obtained using the GSPA approach and VSCF/VCI calculations is similar. The deviations are a reflection of the sensitivity of both calculations of these spectral regions to subtle details in the potential and approximations made in both calculations.

The power of the GSPA approach comes in the ability to use a small basis through systematic and careful choice of vibrational coordinates and basis functions. These choices are informed by the fully anharmonic ground state wave function, which has been obtained using DMC. While aspects of the calculation and the basis that is used are similar to some aspects of VPT2 calculations, the GSPA approach has the advantage that it does not suffer from the singularities that plague VPT2 calculations, particularly in systems like $H_7O_3{}^+$ and $H_9O_4{}^+$ that contain low-frequency, large-amplitude vibrations. Further, the method relies on the ability to calculate the potential energy and dipole functions with sufficient accuracy for spectral evaluation, and the ability to construct a set of internal coordinates as a basis for these calculations. While the availability of a potential often limits the types of systems that can be explored with the GSPA approach, we have recently expanded our DMC calculations to allow us to utilize direct evaluation of electronic energies.[42]

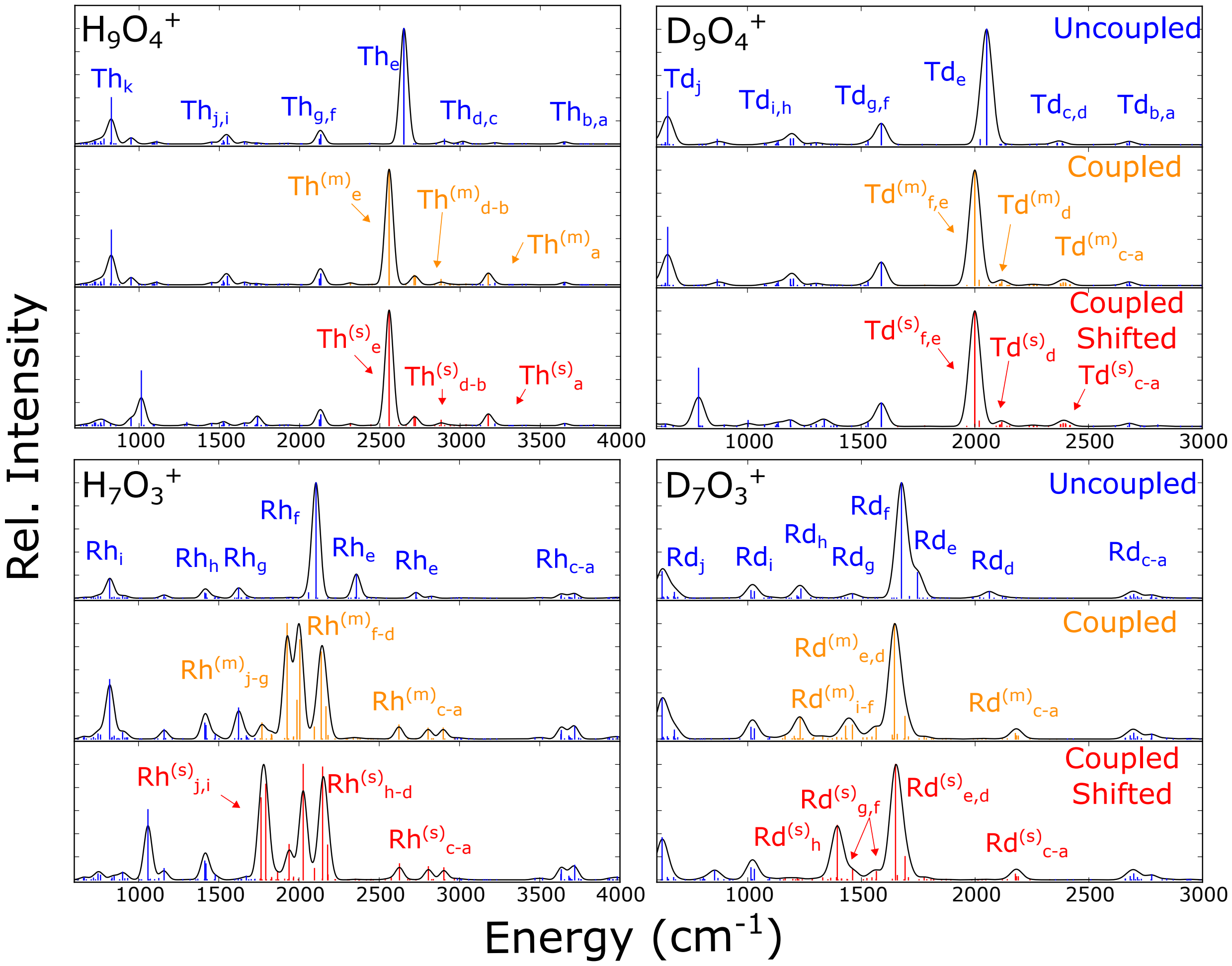

Figure 3.6: Calculated uncoupled GSPA (blue sticks, top), coupled GSPA (gold sticks, middle), and shifted coupled GSPA (red sticks, bottom) spectra of $H_7O_3^+$ (left) $D_7O_3^+$ (right). In these spectra, the Th and Rh labels are used to denote transitions in $H_9O_4^+$ and $H_7O_3^+$, respectively, while Td and Rd are used to refer to peaks in the spectra of the deuterated forms of these ions. For the shifted GSPA spectra, the energies of the transitions involving the umbrella mode have been shifted by the amounts provided in Table 3.6. Assignments for the labeled transitions in the uncoupled spectra are provided in Tables 3.7-3.10, assignments of the transitions in the coupled spectra are provided in Tables 3.15-3.18, and the assignments of the transitions in the coupled shifted spectra can be found in 3.11-3.14.

Table 3.4: Frequencies, Relative Intensities, and Assignments for $H_7O_3^+$ and $D_7O_3^+$

	$H_7O_3^+$		$D_7O_3^+$		
Symbol	Energy (cm^{-1})	Rel. Intensity	Energy (cm^{-1})	Rel. Intensity	Name
$\nu_{\mathrm{OH}}^{w,a,o}$	3761	0.000	2777	0.000	Antisymmetric outer OH stretch
$\nu_{\mathrm{OH}}^{w,a,i}$	3761	0.000	2777	0.000	Antisymmetric outer OH stretch
$\nu_{\mathrm{OH}}^{w,s,o}$	3691	0.002	2682	0.018	Symmetric outer OH stretch
ν_{OH}^{f}	3634	0.024	2698	0.032	Hydronium Free OH Stretch
$\nu_{\mathrm{OH}}^{w,s,i}$	3632	0.013	2661	0.004	Symmetric Outer OH stretch
$\nu_{\mathrm{OH}}^{b,s}$	2358	0.203	1746	0.222	Symmetric Shared Proton Stretch
$\nu_{\mathrm{OH}}^{b,a}$	2106	1.000	1676	1.000	Antisymmetric Shared Proton Stretch
$\nu_{\mathrm{HOH}}^{w,a}$	1622	0.001	1216	0.020	Antisymmetric HOH Bend
$\nu_{\mathrm{HOH}}^{w,s}$	1593	0.000	1182	0.000	Symmetric HOH Bend
$\nu_{\mathrm{HOH}}^{b/f}$	1478	0.012	1096	0.010	Hydronium Bend
ν_{HOH}^{b}	1413	0.044	1014	0.066	Hydronium Bend
$\nu_{\mathrm{rot-A}}^{b}$	858	0.000	615	0.000	Out of plane bend , out of phase
$\nu_{\mathrm{rot-B}}^{b}$	820	0.165	623	0.230	Umbrella; Out of plane bend, in phase
$\nu_{\mathrm{rot-C}}^{b/f}$	622	0.005	456	0.018	In plane H_3O^+ Rotation
ν_{OO}^{a}	369	0.542	327	0.757	Antisymmetric OO Stretch
ν_{OO}^{s}	357	0.031	349	0.053	Symmetric OO Stretch
$\nu_{\mathrm{rock}}^{w,i}$	325	0.476	218	0.000	H_2O rock, in phase
$\nu_{\mathrm{rock}}^{w,o}$	283	0.000	230	0.577	H_2O rock, out of phase
$\nu_{\mathrm{wag}}^{w,o}$	216	0.000	140	0.000	H_2O wag, out of phase
$\nu_{\mathrm{wag}}^{w,i}$	211	0.000	130	0.001	H_2O wag, in phase
ν_{OOO}	83	0.008	93	0.048	OOO Bend
$\nu_{\mathrm{rot-B}}^{f}$	57	0.694	33	1.388	Free Hydronium OH out of plane bend
$\nu_{\mathrm{rot}}^{w,i}$	16	0.000	9	0.079	H_2O rotation, in phase
$\nu_{\mathrm{rot}}^{w,o}$	15	0.026	9	0.000	H_2O rotation, out of phase

Table 3.5: Frequencies, Relative Intensities, and Assignments for $H_9O_4^+$ and $D_9O_4^+$

	$H_9O_4^+$		$D_9O_4^+$		
Symbol	Energy (cm^{-1})	Rel. Intensity	Energy (cm^{-1})	Rel. Intensity	Name
$\nu_{\mathrm{OH}}^{w,a(1/2)}$	3762	0.000	2798	0.000	Antisymmetric OH stretch
$\nu_{\mathrm{OH}}^{w,a(3)}$	3733	0.000	2798	0.000	Antisymmetric OH stretch
$\nu_{\mathrm{OH}}^{w,s,i}$	3694	0.000	2677	0.000	In phase symmetric OH stretch
$\nu_{\mathrm{OH}}^{w,s,o(1/2)}$	3652	0.015	2680	0.024	Out of phase symmetric OH stretch
$\nu_{\mathrm{OH}}^{b,s}$	2878	0.000	2045	0.000	Symmetric shared proton stretch
$\nu_{\mathrm{OH}}^{b,a(1/2)}$	2650	1.000	2052	1.000	Antisymmetric shared proton stretch
$\nu_{\mathrm{HOH}}^{w,a(1/2)}$	1657	0.018	1189	0.049	Antisymmetric H_2O Bend
$\nu_{\mathrm{HOH}}^{w,s}$	1595	0.000	1190	0.000	Symmetric H_2O Bend
$\nu_{\mathrm{HOH}}^{b(1/2)}$	1452	0.016	1075	0.010	Hydronium Bend
ν_{umb}^{b}	827	0.401	649	0.459	Umbrella
$\nu_{\mathrm{rot-A}}^{b}$	745	0.000	564	0.000	Out of plane Hydronium bend (out of phase)
$\nu_{\mathrm{rot-B}}^{b}$	745	0.000	564	0.000	Out of plane Hydronium bend (out of phase)
$\nu_{\mathrm{rot-C}}^{b/f}$	682	0.000	469	0.000	Hydronium rotation
$\nu_{\mathrm{OO}}^{a(1)}$	358	0.447	322	0.654	OO stretch (Rattle)
$\nu_{\mathrm{OO}}^{a(2)}$	358	0.447	322	0.654	OO stretch (Rattle)
$\nu_{\mathrm{rock}}^{w,i}$	315	0.957	247	1.106	H_2O rock, in phase
$\nu_{\mathrm{rock}}^{w,o(1/2)}$	298	0.002	231	0.000	H_2O rock, out of phase
ν_{OO}^{s}	294	0.000	197	0.000	OO Stretch, breathing mode
$\nu_{\mathrm{wag}}^{w,o(1/2)}$	259	0.000	171	0.000	H_2O wag, out of phase
$\nu_{\mathrm{wag}}^{w,i}$	146	0.002	114	0.007	H_2O wag, in phase
$\nu_{\mathrm{OOO}}^{(1/2)}$	76	0.009	70	0.049	OOO Bend
$\nu_{\mathrm{rot}}^{w,o(1/2)}$	22	0.000	7	0.000	H_2O rotation, out of phase
$\nu_{\mathrm{trans,C}}^{b}$	11	2.099	-2	3.675	Hydronium out of plane translation
$\nu_{\mathrm{rot}}^{w,i}$	9	0.000	11	0.000	H_2O rotation, in phase

Table 3.6: Shifts Applied to the Transitions Involving the Umbrella mode for ${H_7O_3}^+$, ${D_7O_3}^+$, ${H_9O_4}^+$, and ${D_9O_4}^+$ Based on the $\Delta n = 1$ Transition Energies (cm^{-1})

System	GSPA	Measured	Shift
${H_7O_3}^+$	820	1059[a]	239
${D_7O_3}^+$	623	800[a]	177
${H_9O_4}^+$	827	1014[b]	187
${D_9O_4}^+$	649	-	138[c]

[a] Ref. 2.

[b] Ref. 5.

[c] Calculated based on the other shifts using $177/239 \times 187 = 138$.

Table 3.7: Uncoupled GSPA Calculated Frequencies, Relative Intensities, and Assignments for the Shared Proton Stretch Region of $\mathrm{H_9O_4}^{+}$[a] (Th)

Symbol	Frequency ($\mathrm{cm^{-1}}$)	Rel. Int.	Assignment
$\mathrm{Th_a}$	3652	0.015	$\nu_{\mathrm{OH}}^{w,s,o(2)}$
	3652	0.015	$\nu_{\mathrm{OH}}^{w,s,o(1)}$
$\mathrm{Th_b}$	3644	0.005	$\nu_{\mathrm{OH}}^{b,s}+\nu_{\mathrm{umb}}^{b}$
$\mathrm{Th_c}$	3019	0.011	$\nu_{\mathrm{OH}}^{b,a(2)}+\nu_{\mathrm{OO}}^{a(1)}$
	3019	0.011	$\nu_{\mathrm{OH}}^{b,a(1)}+\nu_{\mathrm{OO}}^{a(2)}$
	3018	0.011	$\nu_{\mathrm{OH}}^{b,a(1)}+\nu_{\mathrm{OO}}^{a(1)}$
	3018	0.011	$\nu_{\mathrm{OH}}^{b,a(2)}+\nu_{\mathrm{OO}}^{a(2)}$
	3217	0.011	$\nu_{\mathrm{OH}}^{b,s}+\nu_{\mathrm{OO}}^{a(2)}$
	3217	0.011	$\nu_{\mathrm{OH}}^{b,s}+\nu_{\mathrm{OO}}^{a(1)}$
$\mathrm{Th_d}$	2902	0.041	$\nu_{\mathrm{OH}}^{b,s}+\nu_{\mathrm{trans,C}}^{b}$
$\mathrm{Th_e}$	2650	1.000	$\nu_{\mathrm{OH}}^{b,a(2)}$
	2650	1.000	$\nu_{\mathrm{OH}}^{b,a(1)}$
$\mathrm{Th_f}$	2132	0.078	$\nu_{\mathrm{HOH}}^{b(2)}+\nu_{\mathrm{rot-B}}^{b}$
	2132	0.078	$\nu_{\mathrm{HOH}}^{b(1)}+\nu_{\mathrm{rot-A}}^{b}$
$\mathrm{Th_g}$	2124	0.041	$\nu_{\mathrm{HOH}}^{b(2)}+\nu_{\mathrm{rot-C}}^{b/f}$
	2124	0.041	$\nu_{\mathrm{HOH}}^{b(1)}+\nu_{\mathrm{rot-C}}^{b/f}$
$\mathrm{Th_h}$	1657	0.018	$\nu_{\mathrm{HOH}}^{w,a(1)}$
	1657	0.018	$\nu_{\mathrm{HOH}}^{w,a(2)}$
$\mathrm{Th_i}$	1551	0.061	$\nu_{\mathrm{umb}}^{b}+\nu_{\mathrm{rot-A}}^{b}$
	1551	0.061	$\nu_{\mathrm{umb}}^{b}+\nu_{\mathrm{rot-B}}^{b}$
$\mathrm{Th_j}$	1525	0.028	$\nu_{\mathrm{rot-A}}^{b}+\nu_{\mathrm{rot-B}}^{b}$
	1452	0.016	$\nu_{\mathrm{HOH}}^{b(1)}$
	1452	0.016	$\nu_{\mathrm{HOH}}^{b(2)}$
$\mathrm{Th_k}$	827	0.401	ν_{umb}^{b}

[a] These features are plotted in blue in Figures 3.4 and 3.6.

Table 3.8: Uncoupled GSPA Calculated Frequencies, Relative Intensities, and Assignments for the Shared Proton Stretch Region of $D_9O_4{}^{+a}$ (Td)

Symbol	Frequency (cm^{-1})	Rel. Int.	Assignment
$\mathrm{Td_a}$	2680	0.024	$\nu_{\mathrm{OH}}^{w,s,o(1)}$
	2680	0.024	$\nu_{\mathrm{OH}}^{w,s,o(2)}$
$\mathrm{Td_b}$	2669	0.011	$\nu_{\mathrm{OH}}^{b,s} + \nu_{\mathrm{umb}}^{b}$
$\mathrm{Td_c}$	2385	0.011	$\nu_{\mathrm{OH}}^{b,a(2)} + \nu_{\mathrm{OO}}^{a(2)}$
	2385	0.011	$\nu_{\mathrm{OH}}^{b,a(1)} + \nu_{\mathrm{OO}}^{a(1)}$
$\mathrm{Td_d}$	2363	0.013	$\nu_{\mathrm{OH}}^{b,s} + \nu_{\mathrm{OO}}^{a(1)}$
	2363	0.013	$\nu_{\mathrm{OH}}^{b,s} + \nu_{\mathrm{OO}}^{a(2)}$
	2361	0.011	$\nu_{\mathrm{OH}}^{b,a(1)} + \nu_{\mathrm{OO}}^{a(2)}$
	2361	0.011	$\nu_{\mathrm{OH}}^{b,a(2)} + \nu_{\mathrm{OO}}^{a(1)}$
$\mathrm{Td_e}$	2052	1.000	$\nu_{\mathrm{OH}}^{b,a(2)}$
	2052	1.000	$\nu_{\mathrm{OH}}^{b,a(1)}$
$\mathrm{Td_f}$	1589	0.185	$\nu_{\mathrm{HOH}}^{b(1)} + \nu_{\mathrm{rot-A}}^{b}$
	1589	0.185	$\nu_{\mathrm{HOH}}^{b(2)} + \nu_{\mathrm{rot-B}}^{b}$
$\mathrm{Td_g}$	1530	0.027	$\nu_{\mathrm{HOH}}^{b(2)} + \nu_{\mathrm{rot-C}}^{b/f}$
	1530	0.027	$\nu_{\mathrm{HOH}}^{b(1)} + \nu_{\mathrm{rot-C}}^{b/f}$
$\mathrm{Td_h}$	1202	0.050	$\nu_{\mathrm{umb}}^{b} + \nu_{\mathrm{rot-A}}^{b}$
	1202	0.050	$\nu_{\mathrm{umb}}^{b} + \nu_{\mathrm{rot-B}}^{b}$
$\mathrm{Td_i}$	1189	0.049	$\nu_{\mathrm{HOH}}^{w,a(2)}$
	1189	0.049	$\nu_{\mathrm{HOH}}^{w,a(1)}$
$\mathrm{Td_j}$	649	0.459	ν_{umb}^{b}

[a] These features are plotted in blue in Figures 3.4 and 3.6.

Table 3.9: Uncoupled GSPA Calculated Frequencies, Relative Intensities, and Assignments for the Shared Proton Stretch Region of $H_7O_3{}^{+a}$ (Rh)

Symbol	Frequency (cm^{-1})	Rel. Int.	Assignment
$\mathrm{Rh_a}$	3718	0.034	$\nu_{\mathrm{OH}}^{b,s}+\nu_{\mathrm{HOH}}^{b/f}$
$\mathrm{Rh_b}$	3682	0.008	$\nu_{\mathrm{OH}}^{f}+\nu_{\mathrm{rot-B}}^{f}$
	3688	0.004	$\nu_{\mathrm{OH}}^{b,a}+\nu_{\mathrm{HOH}}^{w,s}$
$\mathrm{Rh_c}$	3634	0.024	ν_{OH}^{f}
	3632	0.013	$\nu_{\mathrm{OH}}^{w,s,i}$
$\mathrm{Rh_d}$	2729	0.050	$\nu_{\mathrm{OH}}^{b,s}+\nu_{\mathrm{OO}}^{a}$
	2826	0.016	$\nu_{\mathrm{HOH}}^{b/f}+\nu_{\mathrm{HOH}}^{b}$
$\mathrm{Rh_e}$	2358	0.203	$\nu_{\mathrm{OH}}^{b,s}$
$\mathrm{Rh_f}$	2106	1.000	$\nu_{\mathrm{OH}}^{b,a}$
	2060	0.046	$\nu_{\mathrm{HOH}}^{b}+\nu_{\mathrm{rot-C}}^{b/f}$
$\mathrm{Rh_g}$	1624	0.086	$\nu_{\mathrm{rot-A}}^{b} + \nu_{\mathrm{rot-B}}^{b}$
$\mathrm{Rh_h}$	1413	0.044	ν_{HOH}^{b}
	1421	0.037	$\nu_{\mathrm{HOH}}^{b}+\nu_{\mathrm{rot-B}}^{f}$
	1478	0.012	$\nu_{\mathrm{HOH}}^{b/f}$
$\mathrm{Rh_i}$	820	0.165	$\nu_{\mathrm{rot-B}}^{b}$

[a] These features are plotted in blue in Figures 3.4 and 3.6.

Table 3.10: Uncoupled GSPA Calculated Frequencies, Relative Intensities, and Assignments for the Shared Proton Stretch Region of $D_7O_3{}^{+a}$ (Rd)

Symbol	Frequency (cm^{-1})	Rel. Int.	Assignment
$\mathrm{Rd_a}$	2777	0.028	$\nu_{\mathrm{OH}}^{b,s}+\nu_{\mathrm{HOH}}^{b/f}$
$\mathrm{Rd_b}$	2714	0.012	$\nu_{\mathrm{OH}}^{f} + \nu_{\mathrm{rot-B}}^{f}$
$\mathrm{Rd_c}$	2698	0.032	ν_{OH}^{f}
	2682	0.018	$\nu_{\mathrm{OH}}^{w,s,o}$
$\mathrm{Rd_d}$	2063	0.056	$\nu_{\mathrm{OH}}^{b,s}+\nu_{\mathrm{OO}}^{a}$
$\mathrm{Rd_r}$	1746	0.222	$\nu_{\mathrm{OH}}^{b,s}$
$\mathrm{Rd_f}$	1676	1.000	$\nu_{\mathrm{OH}}^{b,a}$
$\mathrm{Rd_g}$	1461	0.036	$\nu_{\mathrm{HOH}}^{b}+\nu_{\mathrm{rot-C}}^{b/f}$
$\mathrm{Rd_h}$	1234	0.079	$\nu_{\mathrm{rot-B}}^{b}+\nu_{\mathrm{rot-A}}^{b}$
$\mathrm{Rd_i}$	1014	0.066	ν_{HOH}^{b}
	1029	0.057	$\nu_{\mathrm{HOH}}^{b}+\nu_{\mathrm{rot-B}}^{f}$
$\mathrm{Rd_j}$	623	0.230	$\nu_{\mathrm{rot-B}}^{b}$

[a] These features are plotted in blue in Figures 3.4 and 3.6.

Table 3.11: Shifted, Coupled GSPA Frequencies, Relative Intensities, and Assignments for $\mathrm{H_9O_4}^{+a}$ (Th)

Symbol	Frequency (cm^{-1})	Rel. Int.	C_n	n
$\mathrm{Th}_\mathrm{a}^{(\mathrm{s})}$	3175	0.098	-0.530	$\nu_{\mathrm{OH}}^{b,a(2)}+\nu_{\mathrm{OO}}^{a(2)}$
			-0.530	$\nu_{\mathrm{OH}}^{b,a(1)}+\nu_{\mathrm{OO}}^{a(1)}$
			0.485	$\nu_{\mathrm{OH}}^{b,a(2)}+\nu_{\mathrm{OO}}^{s}$
$\mathrm{Th}_\mathrm{a}^{(\mathrm{s})}$	3175	0.098	-0.530	$\nu_{\mathrm{OH}}^{b,a(2)}+\nu_{\mathrm{OO}}^{a(1)}$
			0.530	$\nu_{\mathrm{OH}}^{b,a(1)}+\nu_{\mathrm{OO}}^{a(2)}$
			0.486	$\nu_{\mathrm{OH}}^{b,a(1)}+\nu_{\mathrm{OO}}^{s}$
$\mathrm{Th}_\mathrm{b}^{(\mathrm{s})}$	2882	0.046	0.903	$\nu_{\mathrm{OH}}^{b,s}+\nu_{\mathrm{trans,C}}^{b}$
			0.394	$\nu_{\mathrm{OH}}^{b,s}+\nu_{\mathrm{wag}}^{w,i}$
			-0.098	$\nu_{\mathrm{OH}}^{b,a(2)}+\nu_{\mathrm{rock}}^{w,o(2)}$
$\mathrm{Th}_\mathrm{c}^{(\mathrm{s})}$	2722	0.075	-0.685	$\nu_{\mathrm{OH}}^{b,a(1)}+\nu_{\mathrm{OO}}^{s}$
			-0.675	$\nu_{\mathrm{OH}}^{b,a(2)}+\nu_{\mathrm{OOO}}^{(2)}$
			0.229	$\nu_{\mathrm{OH}}^{b,a(1)}$
$\mathrm{Th}_\mathrm{d}^{(\mathrm{s})}$	2713	0.081	0.676	$\nu_{\mathrm{OH}}^{b,a(1)}+\nu_{\mathrm{OOO}}^{(2)}$
			-0.676	$\nu_{\mathrm{OH}}^{b,a(2)}+\nu_{\mathrm{OOO}}^{(1)}$
			-0.238	$\nu_{\mathrm{OH}}^{b,a(2)}$
$\mathrm{Th}_\mathrm{e}^{(\mathrm{s})}$	2558	1.000	0.686	$\nu_{\mathrm{OH}}^{b,a(1)}$
			-0.531	$\nu_{\mathrm{OH}}^{b,a(2)}$
			0.211	$\nu_{\mathrm{OH}}^{b,a(2)}+\nu_{\mathrm{OO}}^{a(2)}$
$\mathrm{Th}_\mathrm{e}^{(\mathrm{s})}$	2558	0.997	-0.684	$\nu_{\mathrm{OH}}^{b,a(2)}$
			-0.531	$\nu_{\mathrm{OH}}^{b,a(1)}$
			0.211	$\nu_{\mathrm{OH}}^{b,a(2)}+\nu_{\mathrm{OO}}^{a(1)}$

[a] These features are plotted in red in Figure 3.4 and Figure 3.6.

Table 3.12: Shifted, Coupled GSPA Frequencies, Relative Intensities, and Assignments for $D_9O_4{}^{+a}$ (Td)

Symbol	Frequency (cm^{-1})	Rel. Int.	C_n	n
$\mathrm{Td}_{\mathrm{a}}^{(\mathrm{s})}$	2399	0.022	-0.651	$\nu_{\mathrm{OH}}^{b,s}+\nu_{\mathrm{OO}}^{a(2)}$
			-0.429	$\nu_{\mathrm{HOH}}^{w,a(1)}+\nu_{\mathrm{HOH}}^{w,s}$
			0.367	$\nu_{\mathrm{HOH}}^{w,a(2)}+\nu_{\mathrm{HOH}}^{w,a(2)}$
$\mathrm{Td}_{\mathrm{b}}^{(\mathrm{s})}$	2388	0.016	0.683	$\nu_{\mathrm{HOH}}^{w,a(1)}+\nu_{\mathrm{HOH}}^{w,s}$
			-0.635	$\nu_{\mathrm{OH}}^{b,s}+\nu_{\mathrm{OO}}^{a(2)}$
			-0.244	$\nu_{\mathrm{HOH}}^{w,a(2)}+\nu_{\mathrm{HOH}}^{w,a(2)}$
$\mathrm{Td}_{\mathrm{c}}^{(\mathrm{s})}$	2389	0.024	-0.706	$\nu_{\mathrm{OH}}^{b,s}+\nu_{\mathrm{OO}}^{a(1)}$
			-0.584	$\nu_{\mathrm{HOH}}^{w,a(2)}+\nu_{\mathrm{HOH}}^{w,s}$
			-0.318	$\nu_{\mathrm{HOH}}^{w,a(1)}+\nu_{\mathrm{HOH}}^{w,a(2)}$
$\mathrm{Td}_{\mathrm{d}}^{(\mathrm{s})}$	2119	0.034	-0.558	$\nu_{\mathrm{OH}}^{b,s}+\nu_{\mathrm{OOO}}^{(1)}$
			0.499	$\nu_{\mathrm{OH}}^{b,a(1)}+\nu_{\mathrm{OOO}}^{(1)}$
			-0.498	$\nu_{\mathrm{OH}}^{b,a(2)}+\nu_{\mathrm{OOO}}^{(2)}$
$\mathrm{Td}_{\mathrm{d}}^{(\mathrm{s})}$	2118	0.031	-0.634	$\nu_{\mathrm{OH}}^{b,s}+\nu_{\mathrm{OOO}}^{(2)}$
			-0.441	$\nu_{\mathrm{OH}}^{b,a(2)}+\nu_{\mathrm{OOO}}^{(1)}$
			0.394	$\nu_{\mathrm{HOH}}^{b(2)}+\nu_{\mathrm{HOH}}^{b(2)}$
$\mathrm{Td}_{\mathrm{e}}^{(\mathrm{s})}$	2019	0.045	0.977	$\nu_{\mathrm{OH}}^{b,s}+\nu_{\mathrm{trans,C}}^{b}$
			-0.178	$\nu_{\mathrm{OH}}^{b,s}+\nu_{\mathrm{wag}}^{w,i}$
			0.094	$\nu_{\mathrm{HOH}}^{w,s}+\nu_{\mathrm{umb}}^{b}$
$\mathrm{Td}_{\mathrm{f}}^{(\mathrm{s})}$	2000	1.000	-0.884	$\nu_{\mathrm{OH}}^{b,a(2)}$
			-0.210	$\nu_{\mathrm{OH}}^{b,s}+\nu_{\mathrm{OO}}^{a(1)}$
			-0.167	$\nu_{\mathrm{HOH}}^{b(1)}+\nu_{\mathrm{HOH}}^{b(2)}$
$\mathrm{Td}_{\mathrm{f}}^{(\mathrm{s})}$	1999	0.994	0.881	$\nu_{\mathrm{OH}}^{b,a(1)}$
			-0.210	$\nu_{\mathrm{OH}}^{b,s}+\nu_{\mathrm{OO}}^{a(2)}$
			-0.156	$\nu_{\mathrm{OH}}^{b,a(2)}+\nu_{\mathrm{OO}}^{a(1)}$

[a] These features are plotted in red in Figure 3.4 and Figure 3.6.

Table 3.13: Shifted, Coupled GSPA Frequencies, Relative Intensities, and Assignments for $H_7O_3{}^{+a}$ (Rh)

Symbol	Frequency (cm^{-1})	Rel. Int.	C_n	n
$\mathrm{Rh}_{\mathrm{a}}^{(\mathrm{s})}$	2903	0.104	0.908	$\nu_{\mathrm{OH}}^{b,s}+\nu_{\mathrm{OO}}^{A}$
			-0.425	$\nu_{\mathrm{OH}}^{b,a}$
			0.294	$\nu_{\mathrm{OH}}^{b,a}+\nu_{\mathrm{OO}}^{s}$
$\mathrm{Rh}_{\mathrm{b}}^{(\mathrm{s})}$	2806	0.113	-0.591	$\nu_{\mathrm{OH}}^{b,s}+\nu_{\mathrm{OO}}^{s}$
			-0.452	$\nu_{\mathrm{OH}}^{b,a}+\nu_{\mathrm{OO}}^{A}$
			0.446	$\nu_{\mathrm{OH}}^{b,s}$
$\mathrm{Rh}_{\mathrm{c}}^{(\mathrm{s})}$	2626	0.138	0.632	$\nu_{\mathrm{OH}}^{b,s}+\nu_{\mathrm{OO}}^{s}$
			0.547	$\nu_{\mathrm{OH}}^{b,s}$
			-0.547	$\nu_{\mathrm{OH}}^{b,a}+\nu_{\mathrm{OO}}^{A}$
$\mathrm{Rh}_{\mathrm{d}}^{(\mathrm{s})}$	2178	0.301	-0.628	$\nu_{\mathrm{OH}}^{b,s}$
			-0.608	$\nu_{\mathrm{OH}}^{b,a}+\nu_{\mathrm{OO}}^{A}$
			0.291	$\nu_{\mathrm{HOH}}^{b/f}+\nu_{\mathrm{rot-C}}^{b/f}$
$\mathrm{Rh}_{\mathrm{e}}^{(\mathrm{s})}$	2147	0.977	-0.689	$\nu_{\mathrm{HOH}}^{b}+\nu_{\mathrm{rot-C}}^{b/f}$
			-0.662	$\nu_{\mathrm{OH}}^{b,s}+\nu_{\mathrm{OO}}^{a}$
			-0.241	$\nu_{\mathrm{rot-A}}^{b}+\nu_{\mathrm{rot-B}}^{b}$
$\mathrm{Rh}_{\mathrm{f}}^{(\mathrm{s})}$	2097	0.098	-0.951	$\nu_{\mathrm{HOH}}^{b/f}+\nu_{\mathrm{rot-C}}^{b/f}$
			-0.203	$\nu_{\mathrm{OH}}^{b,s}$
			-0.153	$\nu_{\mathrm{OH}}^{b,a}+\nu_{\mathrm{OO}}^{A}$
$\mathrm{Rh}_{\mathrm{g}}^{(\mathrm{s})}$	2026	1.000	0.635	$\nu_{\mathrm{HOH}}^{b}+\nu_{\mathrm{rot-C}}^{b/f}$
			-0.462	$\nu_{\mathrm{OH}}^{b,a}$
			0.389	$\nu_{\mathrm{rot-A}}^{b}+\nu_{\mathrm{rot-B}}^{b}$
$\mathrm{Rh}_{\mathrm{h}}^{(\mathrm{s})}$	1938	0.306	0.871	$\nu_{\mathrm{HOH}}^{w,s}+\nu_{\mathrm{OO}}^{A}$
			0.258	$\nu_{\mathrm{OH}}^{b,a}$
			-0.255	$\nu_{\mathrm{HOH}}^{b}+\nu_{\mathrm{rot-C}}^{b/f}$
$\mathrm{Rh}_{\mathrm{i}}^{(\mathrm{s})}$	1793	0.828	-0.775	$\nu_{\mathrm{rot-A}}^{b}+\nu_{\mathrm{rot-B}}^{b}$
			-0.448	$\nu_{\mathrm{HOH}}^{b}+\nu_{\mathrm{OO}}^{A}$
			0.274	$\nu_{\mathrm{HOH}}^{b/f}+\nu_{\mathrm{OO}}^{s}$
$\mathrm{Rh}_{\mathrm{j}}^{(\mathrm{s})}$	1764	0.710	0.844	$\nu_{\mathrm{HOH}}^{b}+\nu_{\mathrm{OO}}^{A}$
			-0.386	$\nu_{\mathrm{rot-A}}^{b}+\nu_{\mathrm{rot-B}}^{b}$
			0.248	$\nu_{\mathrm{OH}}^{b,a}$

[a] These features are plotted in red in Figure 3.4 and Figure 3.6.

Table 3.14: Shifted, Coupled GSPA Frequencies, Relative Intensities, and Assignments for $\mathrm{D_7O_3}^{+}$[a] (Rd)

Symbol	Frequency (cm^{-1})	Rel. Int.	C_n	n
$\mathrm{Rd}_{\mathrm{a}}^{(\mathrm{s})}$	2190	0.027	-0.682	$\nu_{\mathrm{OH}}^{b,s}+\nu_{\mathrm{OO}}^{A}$
			-0.571	$\nu_{\mathrm{OH}}^{b,s}+\nu_{\mathrm{rot-C}}^{b/f}$
			0.386	$\nu_{\mathrm{OH}}^{b,A}$
$\mathrm{Rd}_{\mathrm{b}}^{(\mathrm{s})}$	2182	0.027	-0.785	$\nu_{\mathrm{OH}}^{b,s}+\nu_{\mathrm{rot-C}}^{b/f}$
			0.526	$\nu_{\mathrm{OH}}^{b,s}+\nu_{\mathrm{OO}}^{A}$
			-0.252	$\nu_{\mathrm{OH}}^{b,A}+\nu_{\mathrm{OO}}^{s}$
$\mathrm{Rd}_{\mathrm{c}}^{(\mathrm{s})}$	2177	0.049	0.583	$\nu_{\mathrm{OH}}^{b,A}+\nu_{\mathrm{OO}}^{A}$
			-0.550	$\nu_{\mathrm{OH}}^{b,s}+\nu_{\mathrm{OO}}^{s}$
			-0.468	$\nu_{\mathrm{OH}}^{b,s}$
$\mathrm{Rd}_{\mathrm{d}}^{(\mathrm{s})}$	1692	0.202	-0.736	$\nu_{\mathrm{OH}}^{b,s}$
			0.380	$\nu_{\mathrm{HOH}}^{w,a}+\nu_{\mathrm{rot-C}}^{b/f}$
			-0.354	$\nu_{\mathrm{OH}}^{b,A}+\nu_{\mathrm{OO}}^{A}$
$\mathrm{Rd}_{\mathrm{e}}^{(\mathrm{s})}$	1650	1.000	0.816	$\nu_{\mathrm{OH}}^{b,A}$
			0.299	$\nu_{\mathrm{OH}}^{b,s}+\nu_{\mathrm{OO}}^{A}$
			-0.267	$\nu_{\mathrm{HOH}}^{w,a}+\nu_{\mathrm{OO}}^{s}$
$\mathrm{Rd}_{\mathrm{f}}^{(\mathrm{s})}$	1566	0.072	0.940	$\nu_{\mathrm{HOH}}^{w,a}+\nu_{\mathrm{OO}}^{s}$
			0.225	$\nu_{\mathrm{OH}}^{b,A}$
			-0.122	$\nu_{\mathrm{HOH}}^{b/f}+\nu_{\mathrm{OO}}^{s}$
$\mathrm{Rd}_{\mathrm{g}}^{(\mathrm{s})}$	1461	0.089	-0.878	$\nu_{\mathrm{HOH}}^{b}+\nu_{\mathrm{rot-C}}^{b/f}$
			-0.403	$\nu_{\mathrm{HOH}}^{b/f}+\nu_{\mathrm{OO}}^{s}$
			-0.146	$\nu_{\mathrm{rot-B}}^{b}+\nu_{\mathrm{rot-B}}^{b}$
$\mathrm{Rd}_{\mathrm{h}}^{(\mathrm{s})}$	1393.8	0.472	-0.823	$\nu_{\mathrm{rot-B}}^{b}+\nu_{\mathrm{rot-B}}^{b}$
			-0.341	$\nu_{\mathrm{HOH}}^{b/f}+\nu_{\mathrm{OO}}^{s}$
			-0.225	$\nu_{\mathrm{OH}}^{b,a}$

[a] These features are plotted in red in Figure 3.4 and Figure 3.6.

Table 3.15: Coupled GSPA Frequencies, Relative Intensities, and Assignments for $H_9O_4{}^{+a}$ (Th)

Symbol	Frequency (cm^{-1})	Rel. Int	C_n	n
$\mathrm{Th}_{\mathrm{a}}^{(\mathrm{m})}$	3175	0.098	-0.530	$\nu_{\mathrm{OH}}^{b,a(2)}+\nu_{\mathrm{OO}}^{a(1)}$
			0.529	$\nu_{\mathrm{OH}}^{b,a(1)}+\nu_{\mathrm{OO}}^{a(2)}$
			0.486	$\nu_{\mathrm{OH}}^{b,a(1)}+\nu_{\mathrm{OO}}^{s}$
$\mathrm{Th}_{\mathrm{a}}^{(\mathrm{m})}$	3175	0.098	0.530	$\nu_{\mathrm{OH}}^{b,a(2)}+\nu_{\mathrm{OO}}^{a(2)}$
			0.530	$\nu_{\mathrm{OH}}^{b,a(1)}+\nu_{\mathrm{OO}}^{a(1)}$
			-0.485	$\nu_{\mathrm{OH}}^{b,a(2)}+\nu_{\mathrm{OO}}^{s}$
$\mathrm{Th}_{\mathrm{b}}^{(\mathrm{m})}$	2881	0.046	0.908	$\nu_{\mathrm{OH}}^{b,s}+\nu_{\mathrm{trans,C}}^{b}$
			0.395	$\nu_{\mathrm{OH}}^{b,s}+\nu_{\mathrm{wag}}^{w,i}$
			-0.082	$\nu_{\mathrm{OH}}^{b,a(2)}+\nu_{\mathrm{rock}}^{w,o(2)}$
$\mathrm{Th}_{\mathrm{c}}^{(\mathrm{m})}$	2713	0.081	0.676	$\nu_{\mathrm{OH}}^{b,a(1)}+\nu_{\mathrm{OOO}}^{(2)}$
			-0.676	$\nu_{\mathrm{OH}}^{b,a(2)}+\nu_{\mathrm{OOO}}^{(1)}$
			-0.238	$\nu_{\mathrm{OH}}^{b,a(2)}$
$\mathrm{Th}_{\mathrm{d}}^{(\mathrm{m})}$	2722	0.075	0.685	$\nu_{\mathrm{OH}}^{b,a(1)}+\nu_{\mathrm{OOO}}^{(1)}$
			0.675	$\nu_{\mathrm{OH}}^{b,a(2)}+\nu_{\mathrm{OOO}}^{(2)}$
			-0.229	$\nu_{\mathrm{OH}}^{b,a(1)}$
$\mathrm{Th}_{\mathrm{e}}^{(\mathrm{m})}$	2558	1.000	0.686	$\nu_{\mathrm{OH}}^{b,a(1)}$
			-0.531	$\nu_{\mathrm{OH}}^{b,a(2)}$
			0.211	$\nu_{\mathrm{OH}}^{b,a(2)}+\nu_{\mathrm{OO}}^{a(2)}$
$\mathrm{Th}_{\mathrm{e}}^{(\mathrm{m})}$	2558	0.997	0.684	$\nu_{\mathrm{OH}}^{b,a(2)}$
			0.531	$\nu_{\mathrm{OH}}^{b,a(1)}$
			-0.211	$\nu_{\mathrm{OH}}^{b,a(2)}+\nu_{\mathrm{OO}}^{a(1)}$

[a] These features are plotted in gold in Figure 3.6.

Table 3.16: Coupled GSPA Frequencies, Relative Intensities, and Assignments for $D_9O_4{}^{+a}$ (Td)

Symbol	Frequency (cm^{-1})	Rel. Int.	C_n	n
$\text{Td}_\text{a}^{(\text{m})}$	2399	0.022	-0.651	$\nu_{\text{OH}}^{b,s}+\nu_{\text{OO}}^{a(2)}$
			-0.429	$\nu_{\text{HOH}}^{w,a(1)}+\nu_{\text{HOH}}^{w,s}$
			0.367	$\nu_{\text{HOH}}^{w,a(2)}+\nu_{\text{HOH}}^{w,a(2)}$
$\text{Td}_\text{a}^{(\text{m})}$	2400	0.016	-0.609	$\nu_{\text{HOH}}^{w,a(1)}+\nu_{\text{HOH}}^{w,a(2)}$
			0.563	$\nu_{\text{OH}}^{b,s}+\nu_{\text{OO}}^{a(1)}$
			-0.422	$\nu_{\text{HOH}}^{w,a(2)}+\nu_{\text{HOH}}^{w,s}$
$\text{Td}_\text{b}^{(\text{m})}$	2389	0.024	-0.706	$\nu_{\text{OH}}^{b,s}+\nu_{\text{OO}}^{a(1)}$
			-0.584	$\nu_{\text{HOH}}^{w,a(2)}+\nu_{\text{HOH}}^{w,s}$
			-0.318	$\nu_{\text{HOH}}^{w,a(1)}+\nu_{\text{HOH}}^{w,a(2)}$
$\text{Td}_\text{b}^{(\text{m})}$	2388	0.016	0.683	$\nu_{\text{HOH}}^{w,a(1)}+\nu_{\text{HOH}}^{w,s}$
			-0.635	$\nu_{\text{OH}}^{b,s}+\nu_{\text{OO}}^{a(2)}$
			-0.244	$\nu_{\text{HOH}}^{w,a(2)}+\nu_{\text{HOH}}^{w,a(2)}$
$\text{Td}_\text{c}^{(\text{m})}$	2378	0.015	-0.705	$\nu_{\text{HOH}}^{w,a(1)}+\nu_{\text{HOH}}^{w,a(2)}$
			0.563	$\nu_{\text{HOH}}^{w,a(2)}+\nu_{\text{HOH}}^{w,s}$
			-0.265	$\nu_{\text{OH}}^{b,a(2)}+\nu_{\text{OO}}^{a(2)}$
$\text{Td}_\text{c}^{(\text{m})}$	2376	0.014	0.570	$\nu_{\text{HOH}}^{w,a(2)}+\nu_{\text{HOH}}^{w,a(2)}$
			-0.568	$\nu_{\text{HOH}}^{w,a(1)}+\nu_{\text{HOH}}^{w,a(1)}$
			0.456	$\nu_{\text{HOH}}^{w,a(1)}+\nu_{\text{HOH}}^{w,s}$
$\text{Td}_\text{d}^{(\text{m})}$	2119	0.034	-0.558	$\nu_{\text{OH}}^{b,s}+\nu_{\text{OOO}}^{(1)}$
			0.499	$\nu_{\text{OH}}^{b,a(1)}+\nu_{\text{OOO}}^{(1)}$
			-0.498	$\nu_{\text{OH}}^{b,a(2)}+\nu_{\text{OOO}}^{(2)}$
$\text{Td}_\text{d}^{(\text{m})}$	2118	0.031	-0.634	$\nu_{\text{OH}}^{b,s}+\nu_{\text{OOO}}^{(2)}$
			-0.441	$\nu_{\text{OH}}^{b,a(2)}+\nu_{\text{OOO}}^{(1)}$
			0.394	$\nu_{\text{HOH}}^{b(2)}+\nu_{\text{HOH}}^{b(2)}$
$\text{Td}_\text{e}^{(\text{m})}$	2019	0.046	-0.981	$\nu_{\text{OH}}^{b,s}+\nu_{\text{trans,C}}^{b}$
			0.174	$\nu_{\text{OH}}^{b,s}+\nu_{\text{wag}}^{w,i}$
			-0.066	$\nu_{\text{OH}}^{b,a(1)}+\nu_{\text{wag}}^{w,o(2)}$
$\text{Td}_\text{f}^{(\text{m})}$	2000	1.000	-0.884	$\nu_{\text{OH}}^{b,a(2)}$
			-0.210	$\nu_{\text{OH}}^{b,s}+\nu_{\text{OO}}^{a(1)}$
			-0.167	$\nu_{\text{HOH}}^{b(1)}+\nu_{\text{HOH}}^{b(2)}$
$\text{Td}_\text{f}^{(\text{m})}$	1999	0.994	0.881	$\nu_{\text{OH}}^{b,a(1)}$
			-0.210	$\nu_{\text{OH}}^{b,s}+\nu_{\text{OO}}^{a(2)}$
			-0.156	$\nu_{\text{OH}}^{b,a(2)}+\nu_{\text{OO}}^{a(1)}$

[a] These features are plotted in gold in Figure 3.6.

Table 3.17: Coupled GSPA Frequencies, Relative Intensities, and Assignments for $H_7O_3{}^{+a}$ (Rh)

Symbol	Frequency (cm^{-1})	Rel. Int.	C_n	n
$Rh_a^{(m)}$	2899	0.095	0.913	$\nu^{b,s}_{OH}+\nu^{A}_{OO}$
			-0.416	$\nu^{b,a}_{OH}$
			0.295	$\nu^{b,a}_{OH}+\nu^{s}_{OO}$
$Rh_b^{(m)}$	2805	0.094	-0.584	$\nu^{b,s}_{OH}+\nu^{s}_{OO}$
			-0.443	$\nu^{b}_{HOH}+\nu^{b}_{HOH}$
			-0.440	$\nu^{b,a}_{OH}+\nu^{A}_{OO}$
$Rh_c^{(m)}$	2623	0.121	-0.626	$\nu^{b,s}_{OH}+\nu^{s}_{OO}$
			0.558	$\nu^{b,a}_{OH}+\nu^{A}_{OO}$
			-0.546	$\nu^{b,s}_{OH}$
$Rh_d^{(m)}$	2168.1	0.279	-0.641	$\nu^{b,s}_{OH}$
			-0.595	$\nu^{b,a}_{OH}+\nu^{A}_{OO}$
			0.332	$\nu^{b/f}_{HOH}+\nu^{b/f}_{rot-C}$
$Rh_e^{(m)}$	2139	0.753	0.772	$\nu^{b}_{HOH}+\nu^{b/f}_{rot-C}$
			0.610	$\nu^{b,a}_{OH}$
			0.216	$\nu^{b,s}_{OH}+\nu^{A}_{OO}$
$Rh_f^{(m)}$	2096	0.104	-0.937	$\nu^{b/f}_{HOH}+\nu^{b/f}_{rot-C}$
			-0.236	$\nu^{b,s}_{OH}$
			-0.176	$\nu^{b,a}_{OH}+\nu^{A}_{OO}$
$Rh_g^{(m)}$	2005	0.859	-0.712	$\nu^{w,a}_{HOH}+\nu^{s}_{OO}$
			0.432	$\nu^{b,a}_{OH}$
			-0.362	$\nu^{b}_{HOH}+\nu^{b/f}_{rot-C}$
$Rh_h^{(m)}$	1988	0.335	0.633	$\nu^{w,a}_{HOH}+\nu^{s}_{OO}$
			-0.627	$\nu^{w,s}_{HOH}+\nu^{A}_{OO}$
			-0.343	$\nu^{b}_{HOH}+\nu^{b/f}_{rot-C}$
$Rh_i^{(m)}$	1926	1.000	-0.718	$\nu^{w,s}_{HOH}+\nu^{A}_{OO}$
			-0.439	$\nu^{b,a}_{OH}$
			0.376	$\nu^{b}_{HOH}+\nu^{b/f}_{rot-C}$
$Rh_j^{(m)}$	1769	0.138	0.959	$\nu^{b}_{HOH}+\nu^{A}_{OO}$
			-0.179	$\nu^{b/f}_{HOH}+\nu^{s}_{OO}$
			0.145	$\nu^{b,a}_{OH}$

[a] These features are plotted in gold in Figure 3.6.

Table 3.18: Coupled GSPA Frequencies, Relative Intensities, and Assignments for $\mathrm{D_7O_3}^{+a}$ (Rd)

Symbol	Frequency (cm^{-1})	Rel. Int.	C_n	n
$\mathrm{Rd}_{\mathrm{a}}^{(\mathrm{m})}$	2190	0.025	-0.674	$\nu_{\mathrm{OH}}^{b,s}+\nu_{\mathrm{OO}}^{A}$
			-0.584	$\nu_{\mathrm{OH}}^{b,s}+\nu_{\mathrm{rot-C}}^{b/f}$
			0.382	$\nu_{\mathrm{OH}}^{b,A}$
$\mathrm{Rd}_{\mathrm{b}}^{(\mathrm{m})}$	2182	0.027	-0.776	$\nu_{\mathrm{OH}}^{b,s}+\nu_{\mathrm{rot-C}}^{b/f}$
			0.537	$\nu_{\mathrm{OH}}^{b,s}+\nu_{\mathrm{OO}}^{A}$
			-0.257	$\nu_{\mathrm{OH}}^{b,A}+\nu_{\mathrm{OO}}^{s}$
$\mathrm{Rd}_{\mathrm{c}}^{(\mathrm{m})}$	2177	0.048	-0.584	$\nu_{\mathrm{OH}}^{b,A}+\nu_{\mathrm{OO}}^{A}$
			0.551	$\nu_{\mathrm{OH}}^{b,s}+\nu_{\mathrm{OO}}^{s}$
			0.467	$\nu_{\mathrm{OH}}^{b,s}$
$\mathrm{Rd}_{\mathrm{d}}^{(\mathrm{m})}$	1691	0.195	-0.732	$\nu_{\mathrm{OH}}^{b,s}$
			0.383	$\nu_{\mathrm{HOH}}^{w,a}+\nu_{\mathrm{rot-C}}^{b/f}$
			-0.351	$\nu_{\mathrm{OH}}^{b,A}+\nu_{\mathrm{OO}}^{A}$
$\mathrm{Rd}_{\mathrm{e}}^{(\mathrm{m})}$	1645	1.000	-0.804	$\nu_{\mathrm{OH}}^{b,A}$
			0.291	$\nu_{\mathrm{HOH}}^{w,s}+\nu_{\mathrm{rot-C}}^{b/f}$
			-0.289	$\nu_{\mathrm{OH}}^{b,s}+\nu_{\mathrm{OO}}^{A}$
$\mathrm{Rd}_{\mathrm{f}}^{(\mathrm{m})}$	1565	0.098	0.932	$\nu_{\mathrm{HOH}}^{w,a}+\nu_{\mathrm{OO}}^{s}$
			0.251	$\nu_{\mathrm{OH}}^{b,A}$
			-0.129	$\nu_{\mathrm{HOH}}^{b/f}+\nu_{\mathrm{OO}}^{s}$
$\mathrm{Rd}_{\mathrm{g}}^{(\mathrm{m})}$	1460	0.121	-0.839	$10+\nu_{\mathrm{rot-C}}^{b/f}$
			-0.477	$\nu_{\mathrm{HOH}}^{b/f}+\nu_{\mathrm{OO}}^{s}$
			0.145	$\nu_{\mathrm{HOH}}^{w,s}+\nu_{\mathrm{OO}}^{A}$
$\mathrm{Rd}_{\mathrm{h}}^{(\mathrm{m})}$	1430	0.111	-0.862	$\nu_{\mathrm{HOH}}^{b/f}+\nu_{\mathrm{OO}}^{s}$
			0.423	$10+\nu_{\mathrm{rot-C}}^{b/f}$
			-0.152	$\nu_{\mathrm{OH}}^{b,A}$
$\mathrm{Rd}_{\mathrm{i}}^{(\mathrm{m})}$	1230	0.190	0.898	$\nu_{\mathrm{rot-B}}^{b}+\nu_{\mathrm{rot-B}}^{b}$
			-0.328	$\nu_{\mathrm{HOH}}^{w,a}+\nu_{\mathrm{OOO}}$
			-0.204	$\nu_{\mathrm{HOH}}^{b/f}+\nu_{\mathrm{OOO}}$

[a] These features are plotted in gold in Figure 3.6.

Table 3.19: Degenerate VPT2 Eigenvectors for the Frequencies with Intensities Greater Than 250 km/mole for $H_7O_3{}^{+a}$

State	1864 cm^{-1} 1996 km/mole	2182 cm^{-1} 570 km/mole	2291 cm^{-1} 493 km/mole	2511 cm^{-1} 451 km/mole	2268 cm^{-1} 291 km/mole	1962 cm^{-1} 290 km/mole	2370 cm^{-1} 285 km/mole
Umbrella overtone	-0.0999887	0.0786380	0.0811653	0.0220112	-0.3317440	0.3718431	0.2077090
Antisymmetric shared proton stretch	-0.7756729	-0.3960983	-0.3693140	-0.3179659	-0.0272219	-0.0482199	-0.0163480
Symmetric shared proton stretch	-0.0389290	0.0427128	-0.0499363	-0.0055641	0.5126822	0.5256205	-0.5155341
Umbrella + Out of plane H_3O^+ rot.	0.5722478	-0.7322176	-0.3099396	-0.1269017	-0.0258428	0.0626847	-0.0098142
In Plane H_3O^+ rot. + HOH bend	0.1784513	0.5108411	-0.8210234	-0.1087296	-0.1436027	0.0148703	-0.0121748
OO Stretch + Symmetric shared proton stretch	0.1636175	0.1764470	0.2659640	-0.9329318	0.0173335	0.0121485	0.0213834
Out of plane H_3O^+ rot. overtone	-0.0234618	-0.0320670	0.0211757	0.0012558	-0.2395484	0.7155379	0.1659745
Out of plane H_3O^+ rot. + HOH bend	-0.0009791	0.0018364	-0.0028375	-0.0009023	0.0272687	0.0151659	-0.0382634
Out of plane HOH rot. + Antisymmetric shared proton stretch	-0.0100928	-0.0721680	0.0235755	0.0010699	-0.2857866	0.2117899	0.1595813
Out of plane HOH rot. + Asymmetric shared proton stretch	0.0058616	-0.0210046	0.1103165	-0.0020306	-0.6502292	-0.1007518	-0.7370257
HOH bend + Antisymmetric shared proton stretch	0.0068944	-0.0134888	0.0215635	0.0093126	-0.2053601	-0.1077129	0.3040194

[a] Reproduced from Ref. 68.

Table 3.20: Degenerate VPT2 Eigenvectors for the Frequencies with Intensities Greater Than 250 km/mole for $D_7O_3{}^{+a}$

State	1678 cm^{-1} (1062 km/mole)	1716 cm^{-1} (583 km/mole)	1464 cm^{-1} (434 km/mole)	1567 cm^{-1} (181 km/mole)
Umbrella overtone	-0.0307717	-0.5228655	-0.1328262	-0.8413064
Asymmetric shared deuterium stretch	0.7702360	-0.3731850	0.5019512	0.1245436
Symmetric shared deuterium stretch	-0.4621568	-0.7440645	0.0379119	0.4747282
Umbrella + Out of plane D_3O^+ rotation	-0.4370316	0.1712117	0.8537931	-0.2252268

[a] Reproduced from Ref. 68.

Table 3.21: Degenerate VPT2 Eigenvectors for the Frequencies with Intensities Greater Than 250 km/mole for ${H_9O_4}^{+a}$

State	2569 cm^{-1} (180 km/mole)	2573 cm^{-1} (195 km/mole)	2666 cm^{-1} (2426 km/mole)	2667 cm^{-1} (2430 km/mole)
Antisymmetric shared proton stretch	0.212577	0.157946206	0.957095	0.117616096
Antisymmetric shared proton stretch	-0.151810	0.221460952	-0.120279	0.955741521
Umbrella + H_3O^+ bend	0.965206	0.01196393	-0.231276	0.121435004
Umbrella + H_3O^+ bend	-0.011955	0.962218742	-0.126547	-0.240786501

[a] Reproduced from Ref. 68.

Table 3.22: GSPA Calculated Frequencies, Relative Intensities, and Assignments for the Low Frequency Region of $H_7O_3{}^+$ (Rh) and $H_9O_4{}^+$ (Th)[a]

System	Symbol	Frequency (cm^{-1})	Rel. Int.	Assignment
$H_7O_3{}^+$	$\mathrm{Rh}_{\mathrm{a}}^{(\mathrm{f})}$	820	0.304	$\nu^{b}_{\mathrm{rot-B}}$
	$\mathrm{Rh}_{\mathrm{b}}^{(\mathrm{f})}$	450	0.344	$\nu^{w,o}_{\mathrm{wag}} + \nu^{w,o}_{\mathrm{wag}}$
	$\mathrm{Rh}_{\mathrm{c}}^{(\mathrm{f})}$	369	1.000	ν^{a}_{OO}
	$\mathrm{Rh}_{\mathrm{d}}^{(\mathrm{f})}$	325	0.878	$\nu^{w,i}_{\mathrm{rock}}$
	$\mathrm{Rh}_{\mathrm{e}}^{(\mathrm{f})}$	253	0.227	$\nu^{f}_{\mathrm{rot-B}} + \nu^{f}_{\mathrm{rot-B}}$
$H_9O_4{}^+$	$\mathrm{Th}_{\mathrm{a}}^{(\mathrm{f})}$	827	0.419	ν^{b}_{umb}
	$\mathrm{Th}_{\mathrm{b}}^{(\mathrm{f})}$	460	0.066	$\nu^{w,o(1)}_{\mathrm{wag}} + \nu^{w,i}_{\mathrm{wag}}$
		460	0.066	$\nu^{w,o(2)}_{\mathrm{wag}} + \nu^{w,i}_{\mathrm{wag}}$
	$\mathrm{Th}_{\mathrm{c}}^{(\mathrm{f})}$	358	0.467	$\nu^{a(1)}_{\mathrm{OO}}$
		358	0.467	$\nu^{a(2)}_{\mathrm{OO}}$
	$\mathrm{Th}_{\mathrm{d}}^{(\mathrm{f})}$	315	1.000	$\nu^{w,i}_{\mathrm{rock}}$
	$\mathrm{Th}_{\mathrm{e}}^{(\mathrm{f})}$	245	0.172	$\nu^{s}_{\mathrm{OO}} + \nu^{b}_{\mathrm{trans,C}}$

[a] These features are plotted in blue in Figure 3.5.

Chapter 4

GPU-ACCELERATED NEURAL NETWORK POTENTIAL ENERGY SURFACES FOR DIFFUSION MONTE CARLO

Reproduced in part with permission from [Ryan J. DiRisio, Fenris Lu, and Anne B. McCoy. GPU-Accelerated Neural Network Potential Energy Surfaces for Diffusion Monte Carlo. *J. Phys. Chem. A* **2021** , 125 (26), 5849-5859]. Copyright [2021] American Chemical Society.

4.1 Introduction

In previous chapters, we discussed the concept of solving the vibrational Schrödinger Equation using Diffusion Monte Carlo to obtain the ground state wave function and zero-point energy for an arbitrary molecular system. In order to calculate the wave function, one must evaluate the potential energy of each of the molecular configurations of each of the walkers in the simulation at every time step. A DMC simulation based on 10 000 walkers that is propagated over 10 000 time steps requires roughly 100 million evaluations of the potential energy. Clearly, it is computationally intractable to perform this many calculations at a high level of theory of electronic structure theory for even the very smallest molecules. As such, DMC simulations often employ potential energy surfaces that have been fit to energies obtained from electronic structure calculations, the spectroscopy of the molecule, or both. Even when fitted potentials are used, the evaluations of these functions can become expensive as the system size is increased. For example, DMC studies of $(H_2O)_6$ required ensembles of 10^6 walkers run for 10^5 to 10^6 time steps to obtain converged results.[43,87]

One solution to this problem is to take advantage of high performance computing resources and introduce multi-node and multi-core parallelism into the DMC code to perform potential calls at each time step. This can be accomplished using packages such as MPI and openMP. Such a strategy was implemented for a 10^6 walker calculation of the ground state of the water hexamer.[43] Even with these modifications, this calculation required a wall time of 2 days, and the calculations use 1088 cores spread among 17 KNL compute nodes. To obtain statistically meaningful results, the results of several (typically 5-10) independent DMC simulations are combined to obtain the final wave function and zero-point energy. This further increases the total computational requirements for a DMC study. Such computational demands severely limit the scope of studies. In particular, this high cost makes studies involving isotopic substitutions, which allow us to gain insights into nuclear quantum effects, intractable for all but the smallest molecular systems.

One strategy, which has been gaining increasing traction, is using machine-learning techniques to generate potential surfaces. In these studies, potential energy surfaces are developed from the results of a small number of electronic structure calculations using methods such as Gaussian Process Regression (GPR) and Artificial Neural Networks (NN). For example, Jiang and Guo used *ab initio* data to generate permutationally invariant neural network potential energy surfaces for reactive scattering calculations.[88] Bačič, Tuckermann, and coworkers used a neural network potential to perform enhanced sampling path integral molecular dynamics on clathrate hydrates.[89] Additionally, Paesani and coworkers compared permutationally invariant polynomials, neural networks, and GPR in calculating many-body energies of water clusters.[90] Miller and co-workers used GPR to fit CCSD(T) quality correlation energies based on molecular orbitals obtained from a Hartree-Fock calculation,[91] and Bowman and Vargas-Hernandez have compared the accuracy and evaluation time of machine learning models using permutationally invariant polynomials and GPR for representing the potential energy surfaces of small molecules from *ab initio* data.[92] In many of these earlier studies, the goal was to develop a global or reactive potential surface with good accuracy across all relevant configurations.

A global potential energy surface is often not necessary. If the process of interest samples a specific region of the potential, describing that region well using neural networks will be sufficient. This is the case for DMC calculations, which focus on the vibrational ground state of the specific system of interest. Clearly, for this approach to be effective, we also need a way to determine the relevant region of the potential before training the neural network.

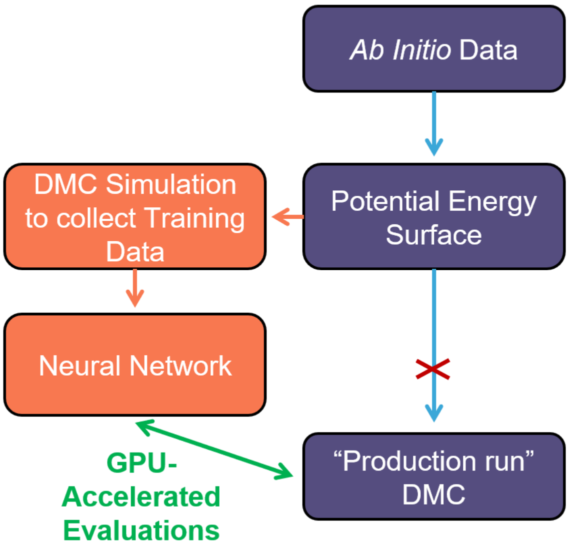

Figure 4.1: The workflow (purple) of a standard DMC simulation. The NN-DMC workflow (orange). In NN-DMC, rather than evaluating the potential energy directly, we first collect training data and train a neural network potential. Then, we use this neural network for parallel, GPU-accelerated potential energy evaluations.

Based on these ideas, in this study we develop a generic algorithm that trains a neural network to learn the region of a potential energy surface for the system of interest over the range of configurations that are sampled in a DMC simulation. The geometries and corresponding energies that are collected as training data are obtained by running a small DMC simulation that uses the potential energy surface that we want to describe with the neural network. Once trained, this NN-potential can be used to perform large scale DMC simulations. This procedure is illustrated in Figure 4.1. To train the neural network, we use the Keras API implemented in the TensorFlow library.[93] Using TensorFlow makes training and evaluating the neural network model compatible with graphics processing units (GPUs).

Evaluating the neural network using GPUs drastically reduces the computation time and resources required for the evaluation of the potential energy. To distinguish this approach from standard DMC methods, we will refer to it as NN-DMC in the following discussion. While the NN-DMC approach can be applied to any potential surface, in the present study we will focus on potential energy surfaces that have been previously fit to electronic structure and where converged DMC simulations are achievable. This will allow us to explore the accuracy of the NN-DMC approach and benchmark the results against traditional DMC calculations.

In this study, we focus on three molecular systems, H_2O, $(H_2O)_2$, and $CH_5{}^+$. These were chosen because they represent examples of the types of systems that are often studied by DMC. In the case of H_2O, the three high-frequency vibrations make it surprisingly challenging to describe accurately using DMC, and the calculation of the ground state of H_2O requires smaller time steps to converge the results compared to $CH_5{}^+$.[43,87] Its small size also makes H_2O amenable to converged variational calculations of the vibrational energies, allowing us to explore the accuracy of the NN-potential for the evaluation of vibrational excited states. As we move to more fluctional molecules, one needs to consider the extent to which it is important to ensure full permutational symmetry in the potential. When full permutational symmetry is required, we must consider how to incorporate the permutational invariance in the NN-potential.

The water dimer presents a good example of a system that has sufficiently high barriers between equivalent minima on the potential such that consideration of full permutational symmetry of the potential will not be necessary for DMC studies that focus on the ground state. In principle, the potential for $(H_2O)_2$ should be invariant under exchange of the two water molecules and exchange of the two hydrogen atoms within either of these water molecules. This leads to eight equivalent minima on the potential. Operationally, a DMC ground state simulation that is initially localized in one of these minima does not sample all eight minima. Based on analysis of the ground state wave function, only the two hydrogen atoms shown in green in Figure 4.2 are found to exchange.[41] Such situations of reduced

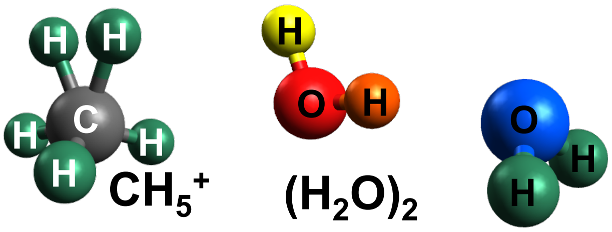

Figure 4.2: The workflow (purple) of a standard DMC simulation. The NN-DMC workflow (orange). In NN-DMC, rather than evaluating the potential energy directly, we first collect training data and train a neural network potential. Then, we use this neural network for parallel, GPU-accelerated potential energy evaluations.

permutation symmetry sampled by the ground state wave function come up in a variety of molecular clusters, and $(H_2O)_2$ allows us to explore the efficacy of the NN-DMC approach for such situations.

We also consider $CH_5{}^+$. This is a molecular ion for which the barriers for exchange of any pair of hydrogen atoms are less than 350 cm^{-1}.[6] This means that the NN-potential must account for the full permutational symmetry of this ion. This is reflected by all five hydrogen atoms in the structure of $CH_5{}^+$ being displayed in green in Figure 4.2 . Upon partial deuteration, the sizes of the effective barriers that separate the minima increase. This leads to localization of the ground state of the ion in a subset of the minima,[94] and the zero point energies of the isotopologues of $CH_5{}^+$ will be sensitive to the the extent to which the ground state is localized. As such, studies of $CH_5{}^+$ and its deuterated analogues provide a stringent test of the NN-DMC approach.

In addition to providing representative model systems to explore the efficacy of the NN-DMC approach, potential surfaces have been developed for each of these three systems, and each of these systems have been previously sttudied using DMC.[6,41,94] For H_2O, we use the potential surface generated by Partridge and Schwenke (PS);[7] for $CH_5{}^+$ we use the surface generated by Jin, Braams, and Bowman (JBB);[6] and for $(H_2O)_2$ we use the generalized water potential MB-pol developed by Paesani and coworkers (MB-pol).[8–10] We will add NN to the beginning of each of these potentials (e.g. NN-PS) to refer to the NN-potential that was trained based on the indicated surface.

4.2 Neural Networks for Fitting Potential Energy Surfaces

Neural networks have been used to generate molecular potential energy surfaces for a variety of systems and in an assortment of contexts. Typically, the training data consists of a set of molecular configurations and the corresponding energies obtained using a specified level of electronic structure theory. For example, Carrington and coworkers generated a neural network potential energy surface for H_2CO using electronic energies evaluated at the CCSD(T) level of theory, which was then used to calculate vibrational energies.[95] Guo and coworkers developed a many-body potential based on CASSCF/CASPT2 data to perform scattering calculations for N_4.[96] Behler and coworkers developed a scalable (2-8mer) protonated water cluster potential energy surface based on DFT energies and used it in *ab initio* molecular dynamics calculations.[97] As mentioned above, the NN-DMC approach can be used with a variety of sources for the potential energies. Since the focus of the present study is to demonstrate the efficacy of the approach, we will use the energies obtained using potential energy surfaces that were previously fit to electronic structure data. Once the training set is determined there are several other considerations that need to be addressed. These include the structure of the neural network and how it is trained as well as the choice of descriptor, and will be described in the following discussion.

4.2.1 Structure and Training of the Neural Network

The details of generating a potential energy surface using neural networks are described thoroughly by Behler, Manzhos and Carrington, and Jiang and Guo.[88,98,99] In the present study, we employ regression neural networks that will be used to learn the region of the potential surface that is relevant to DMC ground state simulations.

Hyperparameter optimization is an important, yet empirical, component of reducing the prediction error of a neural network. The selection of the number of hidden layers, number of nodes per layer, learning rate, activation function, and optimization algorithm each have a significant impact on the accuracy of the resulting neural network. Numerous studies have addressed on these choices for chemical problems. For example, Manzhos and Carrington have noted that one hidden layer of nodes is typically all that is necessary to approximate a potential energy surface when training with evenly-distributed, unbiased electronic structure training data,[99] while Juang and Guo and Bačič and coworkers have elected to employ deep neural networks (i.e. multiple hidden layers) to obtain potential energy surfaces.[88,100] We have elected to use a deep neural network in this work, since the training data obtained from a DMC simulation will be unevenly distributed and biased based on how the ground state wave function samples the potential surface.

Overfitting is generally a concern when training neural networks. Small numerical instabilities can occur when there is a bias towards the accuracy of the potential at geometries included in the training set when compared to geometries that are not included in the training set.[99] Due to the long wavelength of the vibrational ground state wave function, DMC calculations have been shown to be relatively insensitive to small numerical instabilities in the potential.[101] Nonetheless, we will take steps to avoid overfitting, for example by confirming that our training and test sets show similar errors in the calculated energies.

One other ingredient in generating the NN-potential is the choice of activation functions. Activation functions perform a nonlinear transformation of the input data at a given node. It is typical in the computational chemistry community to use sigmoid or hyperbolic tangent functions.[88,90,95,100] These activation functions are well-suited for single, and in some cases, multiple hidden layer networks, but will suffer from the vanishing gradient problem[102,103] in deep learning contexts. To minimize the effect of the vanishing gradient problem, we use the Swish activation function,

$$f(x) = \frac{x}{1+e^{-x}} \tag{4.1}$$

for the nodes in the hidden layers. This function has empirically been shown to perform well in deep learning training.[104] Additionally, we use the the rectified linear unit function (RELU)[105]

$$f(x) = \begin{cases} x & x > 0 \\ 0 & x \leq 0 \end{cases} \tag{4.2}$$

in the output layer. This function forces the predicted energy of the NN-potential to be either positive or 0, even in regions of configuration space that are poorly described by the training data.

The mean squared error was chosen as the loss function, and the Nadam algorithm is used to optimize the weights of the neural network.[106] Since neural networks have trouble learning and predicting a large range of energies, it is typical to transform and scale the training energies before using them to train the neural network.[99] To maintain the generality of our algorithm and to compress the energy range, we uniformly shift the energies so that the training data are based on a potential with its global minimum at 100 cm^{-1}. We then take the natural logarithm of the calculated energies and use the resulting quantities as the input for the neural network. The shift is introduced because the natural logarithm transformation spreads out the energies that are close to zero, increasing the likelihood of overfitting the low-energy region of the potential. With this combination of hyperparameters, we have found that using a neural network with three hidden layers and $10 \times (3N - 6)$ nodes per layer, where N is the number of atoms for the system of interest, yields the training and validation accuracy needed for the present application.

4.2.2 Choice of Descriptor

One of the challenges currently facing the chemistry machine learning community is how to best represent molecular coordinates as rotationally, translationally, and permutationally invariant vectors. In addition to this list, for the purposes of interfacing a neural network potential energy surface with DMC, we aim to find a generic and transferable descriptor whose transformation from the Cartesian coordinates of the atoms can be efficiently evaluated using a GPU. If the calculation of the descriptor takes longer than the original potential energy call, our primary goal of developing an efficient approach for evaluating the potential is not met. To this end, we considered using permutationally invariant polynomials of interatomic distances (PIPs), the Coulomb matrix (CM), and the Behler-Parinello neural network structure that uses atom-centered symmetry functions. Using PIPs is a promising option, however the number of polynomials required to adequately describe molecular systems scales poorly with system size. While there have been recent efforts to contract the number of terms required to describe larger symmetrical systems using fundamental invariants,[107,108] this work has not been extended beyond 10 atoms. The Behler-Parinello neural network formalism is inherently permutationally, rotationally, and translationally invariant.[98] However, finding the sufficient number and types of symmetry functions to use is not obvious and requires empirical testing. Additionally, since all atom-atom distances as well as all atom-atom-atom angles must be calculated for the symmetry functions, this becomes computationally unfavorable.

The CM[109] provides an efficient and effective descriptor due to its generality, its rotational and translational invariance, and its low cost to evaluate. The elements of the CM are given by

$$\mathrm{CM}_{ij} = \begin{cases} 0.5 Z_i^{2.4} & i = j \\ \frac{Z_i Z_j}{r_{ij}} & i \neq j \end{cases} \tag{4.3}$$

where Z_i is the nuclear charge of the ith atom, and r_{ij} is the interatomic distance between atoms i and j. As such, evaluating the elements of the symmetric CM only requires the evaluation of the interatomic distances. The size of the final descriptor, which is the upper or lower triangle of the matrix, scales as N^2, where N is the number of atoms in the system of interest. To obtain permutation invariance from this descriptor, the rows and columns of the CM are reordered based on the norm of the values in the columns.[110] A limitation of using this sorted CM as a descriptor is that it may lead to discontinuities in the NN-potential.[111] In the discussion that follows, we will use the sorted CM as the descriptor for $CH_5{}^+$ to ensure permutational invariance for the NN-potential for this ion. We initially elected not to sort the CM for either H_2O or $(H_2O)_2$ and use the unsorted CM as the descriptor for these systems. We will return to this decision for $(H_2O)_2$ in our discussion of the DMC results. Finally, for efficiency, we implement the unsorted and sorted CM using CuPy, a software package used to execute numerical Python code on GPUs.[112]

4.2.3 Numerical Details

We use the following simulation parameters to reproduce literature values of the calculated DMC zero-point energy reported in Table 4.2. For both the water monomer and water dimer, we propagate 60 000 walkers for 50 000 time steps. For $CH_5{}^+$, with 20 000 walkers, we permute the hydrogen atoms to randomly sample all 120 equivalent minima in the potential, and then run the DMC simulation for 20 000 time steps. We also run analogous calculations for all 5 of the isotopologues of $CH_5{}^+$: CH_4D^+, $CH_3D_2{}^+$,$CH_2D_3{}^+$,$CHD_4{}^+$,$CD_5{}^+$. For $CH_5{}^+$ and $(H_2O)_2$, we also performed larger-scale DMC simulations to ensure convergence for these simulations. 200 000 walkers are propagated for 20 000 time steps for $CH_5{}^+$ and 200 000 walkers are propagated for 50 000 time steps for $(H_2O)_2$. All DMC calculations were performed using a time step ($\Delta\tau$) of 1 a.u. To obtain the zero-point energies reported in Table 4.2, we average V_{ref} starting at 16 667 a.u. for H_2O and $(H_2O)_2$ and at 6667 a.u. for CH_5^+ and its deuterated analogues.

4.3 Training Procedure

The training data set is loaded into the neural network with a batch size of 32 and learning rate of 0.00025. At the end of each full iteration of weight minimization, known as an epoch, the mean absolute error of both the training data set and the validation data set are evaluated to monitor the training progress. The learning rate is halved if the mean absolute error of the training data set does not improve for 5 consecutive epochs, and the training is terminated when the learning rate reaches 10^{-6}.

4.4 Variational Calculation

The calculations of the vibrational levels of water were performed in Jacobi coordinates. While these are not the most efficient coordinates for describing low-lying vibrational levels of water, they have the advantage of a simple kinetic energy operator,

$$\hat{H} = \frac{\hat{p}_r^2}{2\mu_r} + \frac{\hat{P}_R^2}{2\mu_R} + \left(\frac{1}{2\mu_R R^2} + \frac{1}{2\mu_r r^2}\right)\hat{\jmath}^2 + V(R, r, \theta) \tag{4.4}$$

where r represents one of the OH bond lengths, with reduced mass μ_r, R provides the distance between the second hydrogen atom and the center of mass of the OH bond described by r, and θ is the angle between $\vec{r}$ and $\vec{R}$. The reduced mass associated with R is

$$\mu_R = \left(\frac{1}{m_{\mathrm{H}}} + \frac{1}{m_{\mathrm{H}} + m_{\mathrm{O}}}\right) \tag{4.5}$$

To start, three cuts through the potential were taken, one along each of the three coordinates with the other two coordinates set to their equilibrium values. Each cut was used in a 1D Discrete Variable Representation (DVR) calculation,[113] where a DVR based on the Hermite polynomials was used for R and r and the DVR in θ was based on Legendre Polynomials. For each DVR calculation, 250 DVR points were used. The resulting wave functions were used to obtain potential-optimized DVR points, with 35 in R and r and 30 in θ. These DVR points and the associated kinetic energy terms were used to set up the full Hamiltonian along with a potential cutoff of 35 000 cm^{-1}. With these parameters, we were able to converge the energies of the vibrational states of interest to within 1 cm^{-1}.

4.5 *Results and Discussion*

4.5.1 Collection of Training Data

In developing a strategy for collecting training data, our goal was to construct a general approach that is based on the collection of wave functions that are obtained from a DMC simulation without any additional pruning or enhancement of this data. In order for this to be successful, we must ensure that the geometries included in the training data fully sample the regions of the potential that are accessed by the ground state wave function in a DMC simulation. The red curve in Figure 4.3 illustrates the distributions of the energies of walkers obtained from a ground state DMC simulation for CH_5^+. As can be seen, the highest energies that are sampled exceed twice the value of the zero-point energy (dark blue line) of 10 918 cm^{-1}.[37] Additional plots showing the distribution of walker energies obtained from DMC simulations for H_2O and $(H_2O)_2$ can be found in the Supporting Information of this published work.[42]

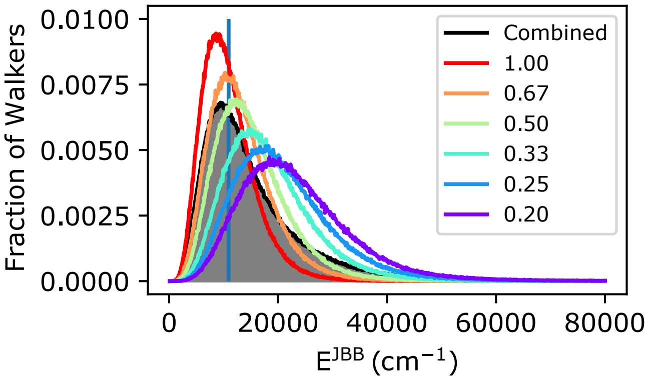

Figure 4.3: The fraction of the number of walkers obtained from DMC simulations plotted a functions of energy obtained using the JBB potential for CH_5^+.[6] The different colors correspond to walker distributions obtained when the masses of each of the atoms in CH_5^+ are multiplied by the indicated value. The shaded black curve provides the distribution of energies of the training data set used to obtain the NN-JBB potential as described in the text. The dark blue vertical line indicates the value of the calculated zero-point energy of CH_5^+.

Above the zero-point energy, the number of walkers with a specified energy decreases with energy. For an $M-$dimensional isotropic harmonic oscillator, the amount of configuration space that corresponds to a particular energy will be the surface area of a $M-$dimensional hypersphere with a radius that is proportional to $\sqrt{E}$. Based on this, the amount of configuration space that corresponds to an energy of E will scale as roughly $E^{(M-1)/2}$. This means that the density of sampled configurations in the DMC ensemble falls off rapidly as a function of E. If we use only the configurations that are captured by the distribution plotted in red in Figure 4.3, we will not have sufficient training data at energies above the zero-point energy for the neural network to provide an accurate description of the potential energy surface. When we performed DMC on a neural network trained only using data obtained from ground state sampling, we found that the NN-potential had large numerical instabilities in the surface, or holes, which caused DMC simulations based on this surface to fail.

One way to ensure that geometries included in the training set sample these higher energy regions of configuration space is to run DMC simulations in which the masses of the atoms have been decreased. For example, the light green distribution in Figure 4.3, which is labeled as 0.5, was obtained by performing a DMC simulation in which the masses of all of the atoms were multiplied by 0.5. This reduction of the atomic mass increases the zero-point energy of the system and expands the region of configuration space that the walkers can access. It also leads to poorer sampling at low-energy regions of the potential.

Based on these observations, we have developed a hybrid approach. The training data is obtained from a DMC simulation in which we propagate a set of walkers with their most abundant masses for the first half of the simulation. During the the second half of the simulation, we decrease the masses of all of the atoms until their masses have been reduced by a factor of ten. This is achieved by multiplying the masses by a constant factor at each time step. In the case of this study, the masses are decreased over the course of 4000 time steps. To decrease the masses of the atoms by a factor of 10 over this time period, at each time step the masses of the atoms are each multiplied by $\sqrt[4000]{0.1}$. The coordinates of the walkers along with their energies are collected periodically throughout this simulation, and this forms the training data for the NN-potential. The resulting energy distribution is shown as the shaded distribution in Figure 4.3. The shaded distribution follows the red curve at low energies while also providing a larger number of geometries at higher energies.

For all systems, we collect training data from a DMC simulation with 20 000 walkers, which is propagated for 8000 time steps with $\Delta\tau = 1$ a.u. All of the walkers are placed at the minimum in the potential at $\tau = 0$ a.u. The training data consists of the ensembles of walkers and their energies, which are collected every 100 time steps throughout the simulation. This results in a training set containing roughly 1.6×10^6 walkers for each system that is considered. By starting all of the walkers at the potential minimum and, in the case of $CH_5{}^+$ and $(H_2O)_2$, collecting the walkers after one time step, we ensure that the region near the potential minimum is well-sampled. This additional step was not required for H_2O, as it lacks the low frequency vibrations and multiple minima exhibited by the other systems.

4.5.2 Validation of Neural Network

A validation set was also collected from the training DMC simulation, where 100 000 randomly chosen walkers are collected using snapshots of the wave function between time step 3000 and 4000, which were not used in the construction of the training set. As such, the validation set only contains walkers that have unscaled masses and reflect geometries sampled by a ground state DMC simulation. The mean absolute error (mae) of the validation set was used as a convergence metric throughout the training process. To generate a test data set that consists of walkers and energies that were not used in the training process, we performed an independent DMC simulation using the same procedure as was used to obtain the training set. We obtained the test set by randomly selecting 80 000 of the generated molecular configurations from the wave functions obtained from this second DMC simulation.

After training the neural networks for the three systems of interest, we calculated the error associated with each model. The results are reported in Table 4.1. We report the mae for each neural network based on the training, validation, and test sets. Since the validation set includes configurations from a typical ground state DMC simulation, the energies of

Table 4.1: Mean Absolute Errors for the Training, Validation and Test Set Obtained for H_2O, $CH_5{}^+$, and $(H_2O)_2$ (cm^{-1}).

System	Training Error	Validation Error[a]	Test Error[b]
H_2O	5	2	5
$CH_5{}^+$	60	33	60
$(H_2O)_2$[c]	28	12	32
$(H_2O)_2$[d]	58	28	61

[a] The validation set consists of 100 000 geometries based on a ground state DMC simulation, as described in the text.

[b] Consists of 80 000 geometries collected during a DMC simulation with scaled masses.

[c] The NN was trained and evaluated using the unsorteed CM descriptor.

[d] The NN was trained and evaluated using the sorted CM descriptor.

the sampled configurations are expected to be smaller on average than the energies of the configurations that make up the training and test sets. In fact, for all three systems, the validation error is roughly half of the training error. The difference between the training and test error is less than 1 cm^{-1} for H_2O and $CH_5{}^+$ and smaller than 4 cm^{-1} for $(H_2O)_2$. This small difference between the training and test errors gives us confidence that the model predicts energies of configurations that are not included in the training set with similar accuracy to configurations that are in the training set.

To further explore how the error is distributed, in Figure 4.4 we plot the density of configurations in the validation set for H_2O as a function of the energy evaluated using the PS potential (E^{PS}) and the difference between values of the energy obtained using the PS potential and the NN-PS potential, $\Delta E = E^{\mathrm{PS}} - E^{\mathrm{NN-PS}}$. Overlaid on this plot, we show the average and standard deviation of ΔE for E^{PS} ranges of 750 cm^{-1}, shown with black dots and error bars, respectively, and a white line at $\Delta E = 0$. As is seen, the average value of ΔE remains close to zero up to 15 000 cm^{-1}, which is nearly four times the zero-point energy for water. The standard deviation of ΔE increases with E^{PS}. In the bottom panel, we plot the

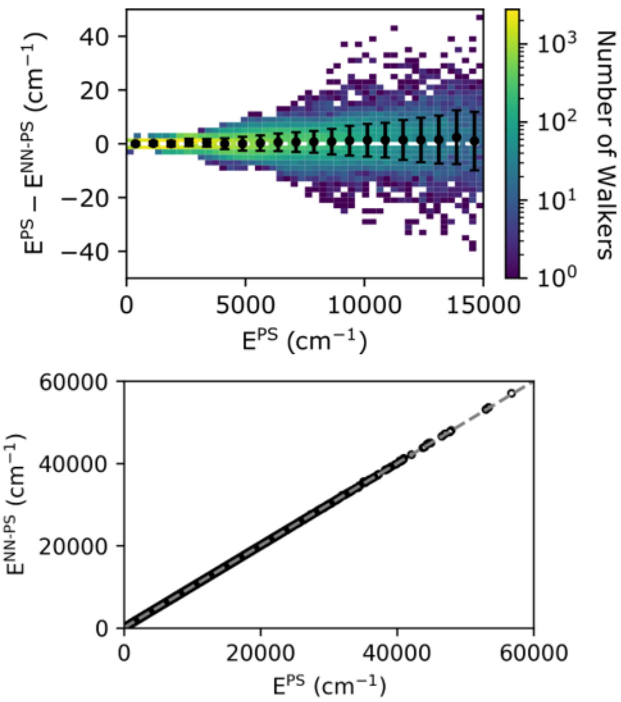

Figure 4.4: Comparisons between the NN-PS and PS[7] potentials for H_2O. (Top) Plot of the number of walkers as a function of the difference between the energies obtained using the PS and NN-PS surfaces and the energy evaluated using the PS surface. Superimposed on the heat map are the average (black circles) and standard deviation (black error bars) of the energy difference over energy ranges of 750 cm^{-1} centered at the position of the black circle. (Bottom) The predicted NN-PS energy (open circles) as a function of the PS energy over the full energy range sampled by the validation set.

correlation between $E^{\text{NN-PS}}$ and E^{PS} over the full energy range sampled by the validation set. The dashed line shows $E^{\text{NN-PS}} = E^{\text{PS}}$. As is seen, the data lies close to the dashed line. Taken together, these results show that while there are small, and growing, deviations between $E^{\text{NN-PS}}$ and E^{PS}, the error is centered at 0 and uniformly distributed about that value. For analogous plots for the other systems, please see the Supporting Information of this published work.[42] Consistent with the reported errors in Table 4.1, the distributions are similar to those for H_2O, albeit with slightly larger ranges of ΔE. The ensemble that is propagated in DMC randomly samples the potential, and the predicted value for the ground state energy is based on an ensemble average of the potential energy, $\bar{V}(\tau)$. Therefore, the uniformly distributed errors described above should lead to errors in the ground state energy that are much smaller than the mae values reported in Table 4.1.

4.5.3 Diffusion Monte Carlo Performance on the Neural Network Surfaces

The goal of this work is to develop a NN-based approach that allows for the efficient and accurate determination of the potential energies for a DMC calculation. Therefore, the most important test of the success of this approach is through comparisons of the energies and wave functions obtained using the NN-potential and the potential on which the NN-potential is based.

In Table 4.2, we compare the zero-point energies for H_2O, ${CH_5}^+$, and $(H_2O)_2$ obtained using the NN-potentials with a small and large ensemble of walkers along with previously reported results obtained using the PS, JBB, and MB-pol potentials, respectively. The smaller NN-DMC calculations were performed using the same ensemble size and propagation time as were used to obtain previously reported results on these systems. We performed the larger calculations to confirm that the results are converged. As can be seen in the results reported in Table 4.2, the energies obtained from the NN-DMC calculations are in excellent agreement with previously reported results for all three systems, with differences for these three systems of 1 cm^{-1} or less. As anticipated, these differences are much smaller than the mae of the energies calculated using the NN-potentials reported in Table 4.1. In addition, the

Table 4.2: Calculated DMC Zero-Point Vibrational Energies for H_2O, $CH_5{}^+$, and $(H_2O)_2$ (cm^{-1}).

System	Literature Value	NN-DMC	Large NN-DMC[a]
H_2O	4637[b]	4637 (0.4)	
$(H_2O)_2$ [c]	9910 (2)[e]	9910 (2)	9909 (0.3)
$(H_2O)_2$ [d]		9909 (3)	9908 (1)
$CH_5{}^+$	10 918 (7)[f]	10917 (4)	10 920 (2)
CH_4D^+	10 307 (11)[f]	10 312 (3)	10 310 (2)
$CH_3D_2{}^+$	9703 (8)[f]	9701 (6)	9703 (1)
$CH_2D_3{}^+$	9101 (8)[f]	9105 (2)	9106 (1)
$CHD_4{}^+$	8563 (6)[f]	8573 (7)	8570 (1)
$CD_5{}^+$	8045 (8)[f]	8048 (6)	8048 (2)

[a] Zero-point energies calculated based on a 200 000 walker DMC simulation described in the Numerical Details.

[b] Variational calculation reported in the manuscript.

[c] The NN was trained and evaluated using the unsorted CM descriptor.

[d] The NN was trained and evaluated using the sorted CM descriptor.

[e] Ref. 41.

[f] Ref. 37.

differences between the zero-point energies obtained from DMC and NN-DMC simulations are generally much smaller than the reported uncertainties of the DMC simulations.

While validation through comparisons of zero-point energies is important, the power of DMC comes from the ability to obtain the ground state vibrational wave function that describes the structure of the system of interest. To this end, we compare the wave functions generated from DMC using the NN-potentials and the potentials on which the NN-potential was based. We first consider the system that is most difficult to describe quantum mechanically, $CH_5{}^+$. As discussed above, $CH_5{}^+$ has 120 equivalent minima, and the energetic barriers to isomerize between these minima are lower than the zero-point energy in the associated vibrations. This leads to full permutation equivalence of the hydrogen atoms in the vibrational ground state. Additionally, when one performs isotopic substitution, the wave function becomes localized in a subset of these minima. This phenomenon has been described in previous work.[94,114] This partial localization of the ground state wave function makes the calculation of the ground state energies and wave functions for partially deuterated $CH_5{}^+$ a particularly stringent test of the NN-potential, as slight deviations in potential can impact the localization of the isotopic variants of this ion.

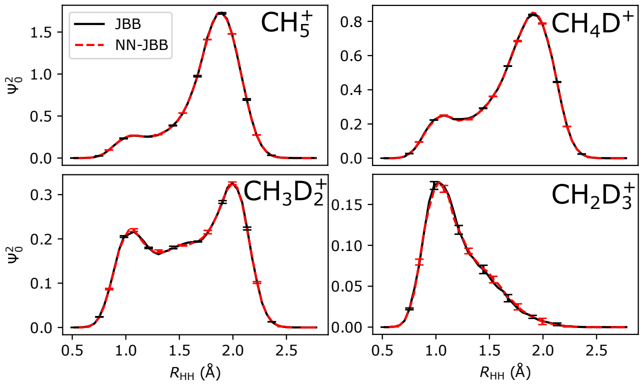

Figure 4.5: Plots of projections of the DMC probability amplitude onto all HH distances of the indicated system based on the JBB[6] (black) and NN-JBB (red) potential. The error bars indicate the standard deviation of the amplitude of Ψ_0^2 among five independent DMC simulations. The projections are normalized based on the number of HH distances in the ion.

We first examine the zero-point energies associated with each of the isotopologues, reported Table 4.2. There is good agreement between the previously reported values based on DMC calculations that used the JBB surface, the NN-DMC calculation, the large-scale NN-DMC calculation. To compare the ground state probability amplitude obtained from DMC calculations using the NN-JBB surface to those obtained using the JBB surface, in Figure 4.5 we project the Ψ_0^2 obtained from these two calculations onto the HH distances in each of the isotopologues of CH_5^+ that contains two or more hydrogen atoms. While there are subtle differences between the distributions obtained when the DMC calculations were performed using the JBB and NN-JBB potentials, these differences are generally smaller than the uncertainty in the values as indicated by the error bars. The corresponding projections onto the HD and DD distances show similar trends (see the Supporting Information of this published work[42]). As noted above, one concern about using the sorted CM as the descriptor in generating the NN-potential comes in the possibility of discontinuities.

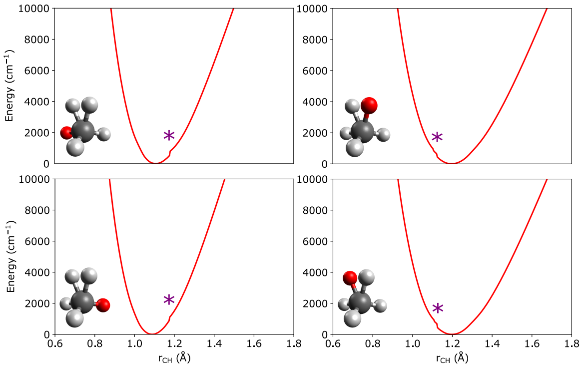

Figure 4.6: One-dimensional cuts through the NN-JBB surface along each of the unique CH stretches in CH_5^+. The red hydrogen in the inset of each panel indicates the hydrogen atom that is displaced. This NN-potential was trained and evaluated using the sorted CM descriptor. This choice leads to discontinuities in the cuts through the potential, which are indicated by the purple asterisks.

In fact, if we plot cuts through the NN-JBB surface along each of the four unique CH bond lengths in CH_5^+, constraining all other coordinates to their equilibrium values, we note such discontinuities (see Figure 4.6). While this is a possible limitation of the use of the sorted CM in the NN-DMC approach, it does not appear to be affecting the accuracy of the zero-point energies or the probability amplitude obtained when we perform a DMC simulation using the NN-JBB potential.

As discussed above, the water dimer is a system that has eight equivalent minima on the potential surface. However, when the DMC simulation is initialized in one of the eight minima, only two of these minima are sampled by the ground state wave function. The water dimer also exhibits highly anharmonic, low frequency vibrational motions in the intermolecular degrees of freedom. To examine how these attributes of $(H_2O)_2$ are captured by the NN-potential, we project the probability amplitude onto pairs of OH distances in Figure 4.7. In the top panel, we show the projection of Ψ_0^2 onto both of the intramolecular OH distances in the donor the water molecule (the two OH bonds of the water molecule with red, orange, and yellow atoms in Figure 4.2). There is excellent agreement between the wave functions collected from DMC simulations using the MB-pol surface and the NN-MB-pol surfaces. In the bottom panel of Figure 4.7, we show the projection of Ψ_0^2 onto the intermolecular OH distances between the oxygen in the donor water and the two hydrogen atoms in the acceptor water (the red oxygen atom and the two green hydrogen atoms in the structure in Figure 4.2). We find generally good agreement between these projections, which are plotted in black and red, although there is a small peak around 2 Å that is only partially captured in the DMC calculation that is based on the NN-MB-pol potential. If we train a new NN-potential using the sorted CM as the molecular descriptor and perform a DMC calculation, we recover this feature (gold dotted line). The mae for this new NN-potential is reported in Table 4.1, the DMC zero-point energies are reported in Table 4.2. The training, test, and validation mae of the sorted CM NN-MB-pol surface are all comparable to the mae of the CH_5^+ model, which contains the same number of atoms and also uses the sorted CM as the molecular descriptor. Additionally, the zero-point energy calculated using the sorted CM NN-potential is in agreement with the NN-DMC simulations that used the unsorted CM NN-potential for $(H_2O)_2$.

Upon closer inspection of the walkers that correspond to the peak near 2 Å in the pro-

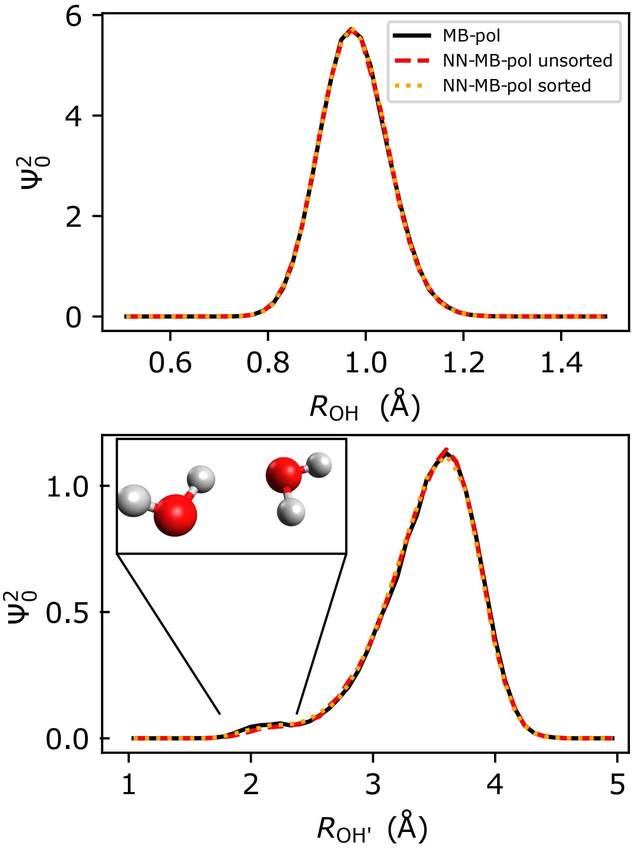

Figure 4.7: The DMC ground-state probability amplitude obtained from simulations using the NN-MB-pol with an unsorted CM descriptor (red dashed lines) and a sorted CM descriptor (gold dotted lines) and the MB-pol[8–10] potentials (black solid lines) projected onto pairs of OH distances in $(H_2O)_2$. (Top) The DMC probability amplitude projected onto the intramolecular OH distance in the donor water molecule (the two OH bonds between the red oxygen and orange and yellow hydrogen atoms in Figure 4.2). (Bottom) The DMC probability amplitude projected onto an intermolecular OH distance between the hydrogen atoms in the donor water molecule and the oxygen atom in the acceptor water molecule (the distance between the red oxygen and the two green hydrogen atoms in Figure 4.2). The inset in the bottom panel shows the geometry of a walker that contributes to the feature near 2 Å, where the walkers sample geometries near the transition state for the exchange of the identities of the donor and acceptor water molecules.

jections of the ground state probability amplitude plotted in the bottom panel of Figure 4.7, we find that they are structurally similar to the hydrogen bond interchange transition state,[115,116] which is shown in the inset in the bottom panel of Figure 4.7. The energy of this transition state has been reported as approximately 235 cm^{-1} based on the MB-pol surface,[115] while the harmonic normal mode frequency that corresponds to the motion that connects the minimum energy structure and this transition state is below 200 cm^{-1}. While the ground state DMC calculation may sample geometries that are near this transition state, the walkers are not able to tunnel through this barrier. When we examined the structures that are sampled by the DMC simulation used to generate the training and test sets, we found they do not show evidence of tunneling through this barrier. The enforced symmetry introduced by the sorted CM provides an improved description of this region of the potential and more accurate ground state wave function. Further evidence of this improvement can be seen in the projections of Ψ_0^2 onto the intermolecular HH distances shown in Figure 4.8. Finally, we have considered the projections of the probability amplitude onto the OH distance and HOH bend in H_2O, and the results are provided in the Supporting Information of the published work. The projections obtained using the NN-PS surface show excellent agreement with those obtained using the PS surface.

4.5.4 Efficiency Gain from Neural Network Potentials

Next we consider the relative efficiency of the NN-potentials when compared to the potential energy surfaces on which the NN-potentials are based. To explore this, we calculate the time it takes to evaluate the energies using the MB-pol potential and the GPU accelerated NN-MB-pol potential for $(H_2O)_2$. The analogous timing plots for H_2O and $CH_5{}^+$, as well as detailed timings for all the systems, are found in Figure 4.10 and Table 4.3. We call the compiled MB-pol surface within Python using the ctypes foreign function interface, and we parallelize the calls to MB-pol across CPU cores using Python's multiprocessing module. In Figure 4.9, we compare the average time required to evaluate the potential energy over 400 time steps in a DMC simulation for a series of different ensemble sizes. Continuous weighting

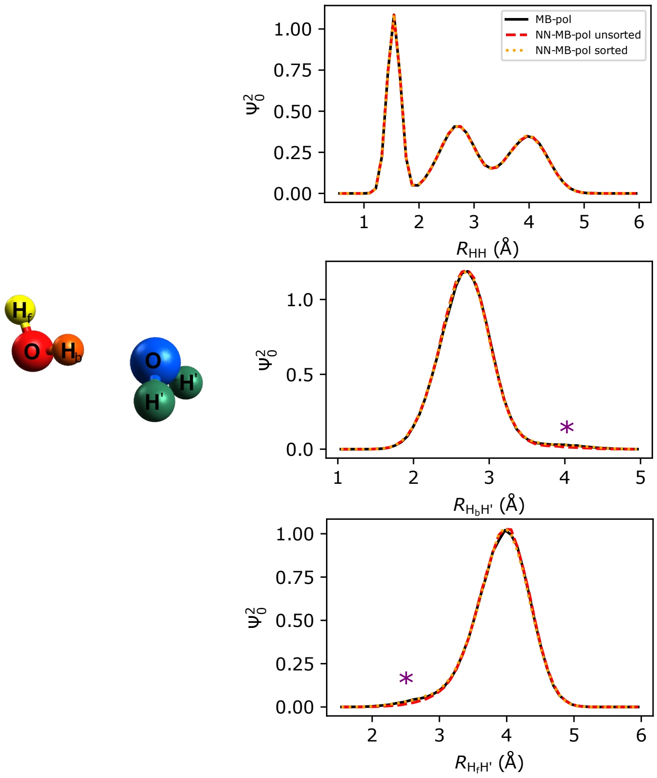

Figure 4.8: (Top) The DMC ground-state probability amplitude projected onto all six HH distances in the water dimer using the potential energy surfaces denoted in the legend. (Middle) The DMC probability amplitude projected onto the intermolecular HH distances between the hydrogen-bonded hydrogen atom in the donor water molecule, and the two hydrogen atoms in the acceptor water molecule (the distance between the orange hydrogen and the two green hydrogen atoms). (Bottom) The DMC probability amplitude projected onto the intermolecular HH distances between the free hydrogen atom in the donor water molecule and the two hydrogen atoms in the acceptor water molecule (the distance between the yellow hydrogen and the two green hydrogen atoms). The shoulders in the distributions, indicated by purple asterisks, in the middle and bottom panels correspond to the transition state geometries discussed in the text.

DMC[36] is used in these calculations in order to keep the ensemble size constant throughout the 400 time steps. The DMC simulations using the MB-pol potential are performed using a single 28-core Intel Xeon E5-2680 v4 2.40 GHz processor. We perform the analogous calculation on the NN-potential using one of the GPU nodes on the Cori supercomputer at the National Energy Research Scientific Computation Center (NERSC). These GPU nodes have 8 NVIDIA Tesla V100 GPUs per node and two 20-core 2.40 GHz Intel Xeon Gold 6148 Skylake processors. For these NN-DMC calculations, only one of the 8 GPU nodes was used.

Table 4.3: Average Potential Energy Call Time for the NN-Potential and the Potential On Which the NN-Potential Is Based (s).

Ensemble Size	PS[a]	NN-PS[a]	JBB[a]	NN-JBB[a]	MB-pol[b]	NN-MB-pol[b]
100	0.003	0.016	0.003	0.018	0.005	0.017
1000	0.002	0.016	0.002	0.018	0.006	0.016
10 000	0.004	0.016	0.02	0.019	0.034	0.018
100 000	0.037	0.025	0.153	0.038	0.324	0.037
1 000 000	0.27	0.085	1.163	0.322	3.087	0.31

[a] Plotted in Figure 4.10.

[b] Plotted in Figure 4.9.

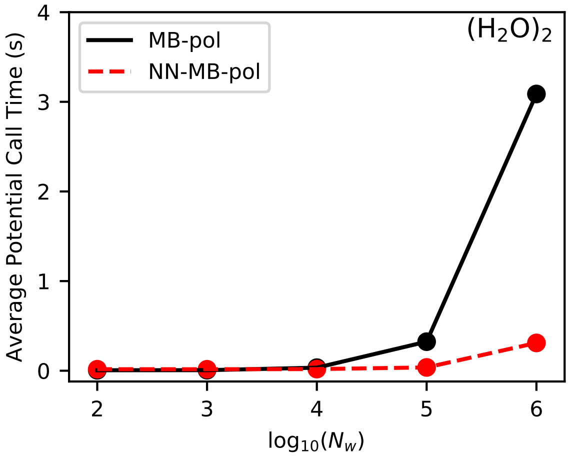

Figure 4.9: The average potential energy call time in a sample DMC simulation for varying numbers of $(H_2O)_2$ configurations using the MB-pol surface[8–10] (black solid) compared to the NN-MB-pol surface (red dashed).

The results plotted in Figure 4.9 illustrate that the GPU-optimized NN-MB-pol evaluations scale significantly better than the calls to the underlying MB-pol potential. The improvement is shown most prominently in the 10^6 walker case, where the GPU calls of thee NN-potential are 3x faster for H_2O, 4x faster for $CH_5{}^+$, and 10x faster for $(H_2O)_2$ compared to the CPU calls to the potential on which the NN-potential is trained. In some senses this comparison is not entirely fair as similar speed-ups could be obtained by using a version of the underlying potentials that has been modified to take advantage of GPU's. This is not always a straight-forward procedure, and advantage of the present approach for obtaining the NN-potentials is that it can be applied to a broad range of potential surfaces without modification.

With these gains in speed we can perform extremely large NN-DMC simulations at a cost that is independent of the cost to evaluate the underlying potential. As such, the use of these NN-potentials will enable us to perform DMC calculations that use significantly more expensive approaches for evaluation of the potential energy. For example, we are currently exploring applications in which the energies are evaluated using electronic structure

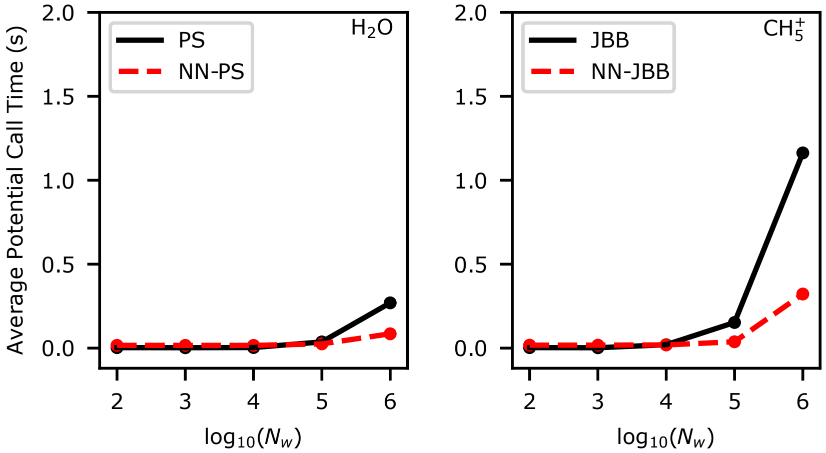

Figure 4.10: The average potential energy evaluation time plotted as a function of the number of walkers for H_2O (left) and $CH_5{}^+$ (right). The black solid and red dashed lines on the left correspond to the PS[7] and NN-PS surfaces, respectively, and the black solid and red dashed lines on the right correspond to the NN-JBB and JBB[6] potentials, respectively. The plotted data is provided in Table 4.3.

calculations directly.

4.5.5 Variational Calculation of Vibrational States Using the NN-Potential

The discussion above focuses on ground state properties, and the geometries that were used to develop the NN potential for the NN-DMC calculation were chosen for the calculation of the ground state. It is interesting to ask how well this potential describes excited states. In the case of water, the excited state vibrational energies are reasonably straightforward to evaluate, and the details of the calculation are provided in the Supporting Information of this published work.[42] The results of these calculations are provided in Table 4.4. Comparing the results obtained using the PS and NN-PS potentials, we find there are small differences in energies. For example, the zero-point energies differ by 0.1 cm^{-1}, while the energies of all other vibrational states differ by less than 1 cm^{-1}. The calculated zero-point energy is also in excellent agreement with the DMC values reported in Table 4.2. This shows that the

NN-potential obtained for DMC calculations can also be used in other types of large scale calculations that require many calls to a potential energy surface.

Table 4.4: Ground and Excited State Vibrational Energies for H_2O Using the NN-PS and the PS Potentials[7] (cm^{-1}).

v_s^a	v_b	v_a	PS^b	NN-PS
0	0	0	4636.8	4636.9
0	1	0	1594.4	1594.5
0	2	0	3150.8	3150.8
1	0	0	3656.2	3656.7
0	0	1	3755.1	3755.5
0	3	0	4665.7	4666.0
1	1	0	5233.8	5234.4
0	1	1	5330.0	5330.5

[a] v_s, v_b, v_a correspond to number of quanta in the symmetric OH stretch, the HOH bend, and the antisymmetric OH stretch, respectively.

[b] The first row reports the zero-point energy E_0, and all other values are $E-E_0$.

4.6 Conclusions

In this work, we have developed a generic algorithm to train a neural network to learn a potential energy surface using data obtained from a single, small-scale DMC simulation. After training this neural network, we are able to perform large-scale DMC simulations by taking advantage of the efficiency of parallel evaluations of the NN-potential on a GPU. These NN-potentials are system-dependent, meaning that one has to train a new neural network for each system of interest and for different isomers of a particular molecular cluster. These surfaces focus on describing low energy vibrational states, although modification of the training protocols could extend the region covered by the neural network. There are other methods, such as path integral ground state (PIGS) methods[117,118] and Path Integral Monte Carlo[119,120] that require dozens to hundreds of potential energy evaluations per step. These methods can also take advantage of parallel evaluation of these potential energy values on a GPU.

Chapter 5

ISOLATING THE VIBRATIONAL SPECTRAL SIGNATURES OF SITE-SPECIFIC WATER MOLECULES IN $Cs^+ \cdot H_2O(D_2O)_{19}$ USING CHANGES IN ELECTRON DENSITY

Reproduced in part with permission from [Nan Yang, Thien Khuu, Sayoni Mitra, Chinh H. Duong, Mark A. Johnson, Ryan J. DiRisio, Anne B. McCoy, Evangelos Miliordos, and Sotiris S. Xantheas. Isolating the Contributions of Specific Network Sites to the Diffuse Vibrational Spectrum of Interfacial Water with Isotopomer-Selective Spectroscopy of Cold Clusters. *J. Phys. Chem. A* **2020** , 124 (50), 10393-10406]. Copyright [2020] American Chemical Society.

5.1 Introduction

Understanding the spectroscopy of liquid water has been a subject of study for many years. As mentioned in previous chapters, studying bulk water in detail is difficult due to computational cost. As such, advancements in computational and experimental methods to study the spectroscopy of chemical models of liquid water have led to novel interpretations of the dynamics and structure of liquid water.[47–53] These models include small protonated water clusters[2,5,54–59] as well as larger ionic clusters.[11,121–123]

Recently, Johnson, McCoy, and coworkers reported the gas-phase infrared spectra of $Cs^+ \cdot (H_2O)_{20}$ and its deuterated analogs.[121] In that work and in this analysis,[11] the infrared spectrum of $Cs^+ \cdot (H_2O)_{20}$ and $Cs^+ \cdot H_2O(D_2O)_{19}$ were compared to an experimental spectrum of the surface of liquid water. The gas-phase cluster spectra were collected using a tandem mass-spectrometry infrared spectroscopy procedure, where the detection of bare, untagged Cesium clusters were measured upon loss of a D_2 tag due to vibrational excitation. A more detailed explanation of the experiment can be found elsewhere.[11,121]

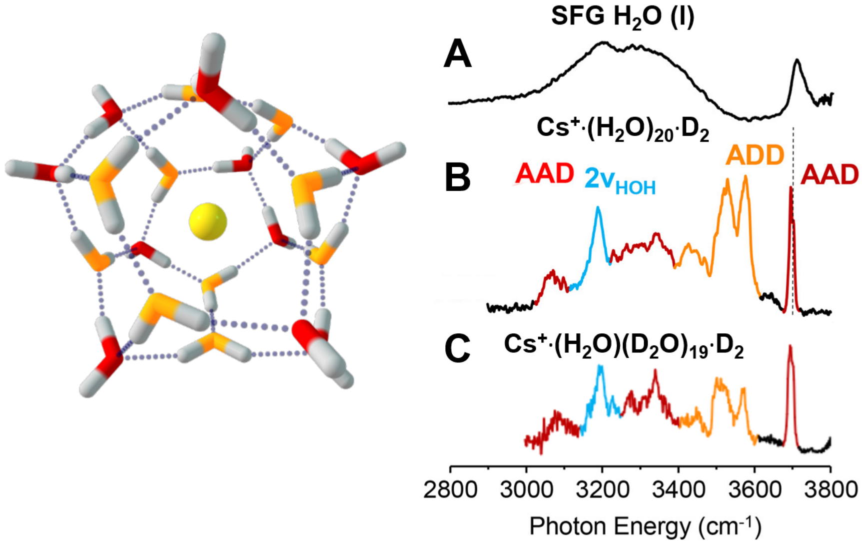

Figure 5.1: (Left) The structure of $Cs^+ \cdot (H_2O)_{20}$, color-coded to highlight the type of hydrogen bond donor present in the cluster.[11] The red molecules correspond to a water monomer that is accepting two hydrogen bonds, and donating one (AAD), and the orange molecules are donating two hydrogen bonds and accepting one (ADD). (Right) (A) The sum-frequency generation (SFG) spectrum of liquid water compared to the spectrum of (B) D_2-tagged $Cs^+ \cdot (H_2O)_{20}$ and (C) $Cs^+ \cdot H_2O(D_2O)_{19}$. The feature near 3700 cm^{-1} corresponds to the unbounded OH stretches.

In both the sum-frequency generation (SFG) spectrum of the surface of liquid water and $Cs^+ \cdot (H_2O)_{20}$, as seen in Figure 5.1, there are broad peaks ranging from 3000-3600 cm^{-1} that are widely attributed to the fundamental excitations in the OH stretches in water.[11,121] The broad spectral envelope in this OH stretching region reflects the fact that the frequencies of the OH oscillators are modulated by the hydrogen bonding environment of the water molecule. Since the spectrum of $Cs^+ \cdot (H_2O)_{20}$ has a similarly broad spectroscopic feature as the spectrum of the surface of water, this implies that $Cs^+ \cdot (H_2O)_{20}$ can act as a model system through which to study the complicated hydrogen bonding network of liquid water. Specifically, we will study how the hydrogen bonding environment of $Cs^+ \cdot (H_2O)_{20}$ affects the hydrogen bond strength of a water molecule, and in turn its characteristic hydrogen-bonded

OH stretch frequency.

Interestingly, the gas-phase infrared spectrum of $Cs^{+}\cdot(H_2O)_{20}$ and $Cs^{+}\cdot H_2O(D_2O)_{19}$ are almost identical (see spectra B and C in Figure 5.1). The fact that the features in the spectrum are so similar implies that, in the experiment, the H_2O molecule occupies each of the 20 sites in the water network in $Cs^{+}\cdot H_2O(D_2O)_{19}$ with roughly equal preference. In addition, it shows that there is minimal information loss in examining the spectral region of a single monomer compared to the ensemble. Because of this spectroscopic phenomenon, we can make direct connections between theory and experiment by examining in detail the environment of a single water monomer, particularly in how the impact of the hydrogen-bonding environment of individual water molecules relates to its infrared spectral signature.

To perform this analysis, we must construct a theoretical model that relates the relative hydrogen bonding environment of a given water monomer participating in hydrogen bonding to its hydrogen bond strength and its OH stretch frequency. Skinner and Ohno have formulated theoretical models that relate the physical characteristics of water systems to their infrared spectroscopy. Skinner has empirically shown through a large number of electronic structure calculations that the frequency shift of the hydrogen-bonded, OH stretch vibration in a water network relative to an isolated water monomer is correlated to the solvation environment of the water molecule.[124,125] The different coordination types are defined based on whether the monomer is donating (D) a hydrogen bond through its hydrogen atom, or accepting (A) a hydrogen bond through its oxygen atom. From this simple categorization, one can name the various solvation environments for a single water molecule in solution: A, AD, AAD, ADD, and AADD. Skinner has decomposed the broad spectral envelope in liquid water into contributions from these five types of water monomers.

A qualitative explanation put forth by Skinner relates the hydrogen bond strength to charge transfer between the hydrogen donor atom and the lone pair electrons on the acceptor water molecule. The lone pair electrons are donated into the σ^* orbital of the OH bond, elongating it. This strengthens the hydrogen bond and lowers the vibrational frequency. An example of this model can be examined if one considers a double acceptor, single

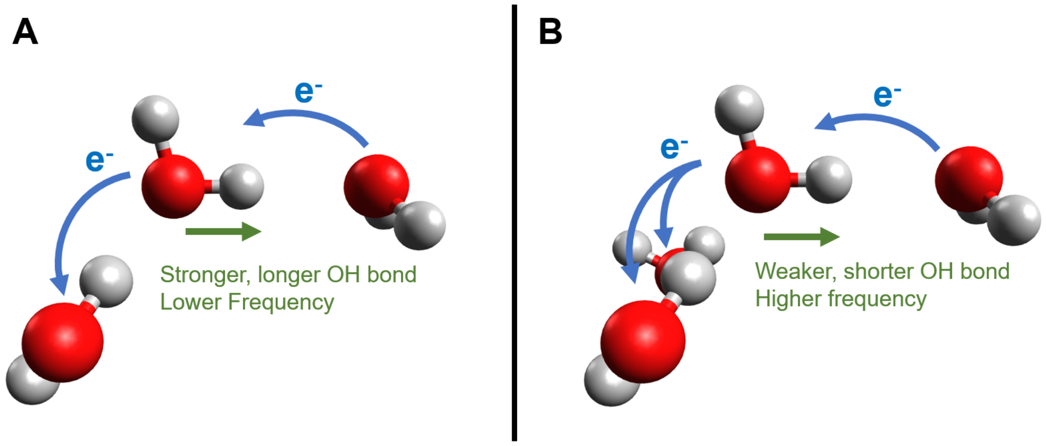

Figure 5.2: Schemes of Skinner's postulated change in electron density for (A) a single acceptor, single donor (AD) molecule and (B) A double acceptor, single donor (AAD) water molecule. The movement of electrons in the ADD monomer leads to a weaker hydrogen bond, leading to a shorter OH bond and higher OH stretch frequency.

donor (AAD) monomer (see Figure 5.2). The two hydrogen bonds accepted by the donating monomer would lead to a weaker donor hydrogen bond relative to a single acceptor (AD), as there is further depletion in the electron density that can populate the σ^* orbital. This qualitative picture can be expanded to explain the cooperative and anti-cooperative effects of the various different types of hydrogen bonding environments.

Ohno summarized these observations by defining a parameter, M, which relates the OH bond strength to the number of donor and acceptor hydrogen bonds surrounding the two participating water molecules involved in a hydrogen bond of interest.[126] The value is defined as:

$$M = -d' + a' + d'' - a'' \tag{5.1}$$

where d′ and a′ are the number of donor and acceptor water molecules surrounding the donor monomer in the hydrogen-bonded water dimer, and d″ and a″ are the number of donor and acceptor water molecules surrounding the acceptor monomer in the dimer. The formula accounts for the change in hydrogen bond strength as a result of the presence of these molecules, where the higher the M-value, the stronger the hydrogen bond. Examples of the correlation between the M-value and the strength of the hydrogen bond, measured by the OH stretch frequency in the $Cs^+ \cdot H_2O(D_2O)_{19}$ cluster, can be found in Figure 5.3.

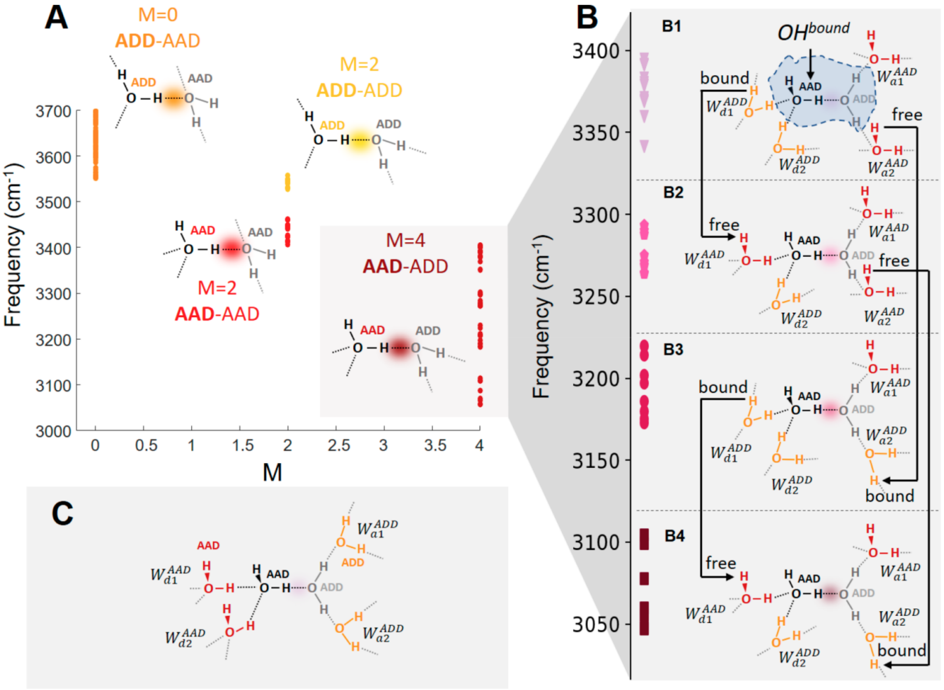

Figure 5.3: Calculated bound OH frequencies in isomers of $Cs^+ \cdot H_2O(D_2O)_{19}$ classified by their hydrogen bonding environments. (A) Harmonic frequencies of the bound OH groups plotted against the M index proposed by Ohno. These points are further classified and color coded with an index proposed by Skinner and co-workers, which capture the binding type of both the donor and acceptor water molecules of the H-bond of interest. The schematic structures are shown as water dimers. For example, AAD-ADD corresponds to the case where an OH group on an AAD water molecule donates to an ADD water molecule. The OH oscillators indexed by $M = 4$ (or AAD-ADD) are again further classified in (B) by the binding types of water molecules surrounding the dimer (W_a and W_d). B1 and C represent the environments that yield the weakest and strongest H-bond in the central dimer, respectively. B1-B4 are the structures present in the clusters. The black brackets highlight the change of exterior water molecule's type from one class to another.

The categorization scheme put forth by Ohno and the qualitative, empirical explanation put forth by Skinner are helpful and informative explanations for how hydrogen bond strength affects the frequency of the OH oscillator. However, in this chapter, we will quantify these effects by calculating the change in quantum mechanical electron density of a hydrogen bond donor and acceptor pair relative to varying solvation environments. We will discuss how the resultant electron density difference relates to the strength of hydrogen bonding and thus the OH stretch frequency in the donor/acceptor pair. Once this is established, we will apply this technique to the $Cs^+ \cdot H_2O(D_2O)_{19}$ cluster.

5.2 Calculating Changes in Electron Density in a Model Water Cluster

To quantify how the strength of a hydrogen bond changes with the local solvation environment that surrounds it, we turn to electronic structure calculations. Skinner postulated that the change in vibrational frequency is related to the change in electron occupancy of molecular orbitals. Here, we generalize that idea and investigate the change in quantum mechanical electron density in the hydrogen bonding region of a water dimer when its first and second solvation shell environment change. Specifically, we explore how adding or removing donors (D) and acceptors (A) on both water molecules participating in the hydrogen bond affects the electron density in the hydrogen-bonding region and develop a metric that encapsulates these changes, δ_e.

To explore the effects of solvation on a single hydrogen bond, we solvate a water dimer, the simplest hydrogen bonding scheme, with six water molecules: two that donate hydrogen bonds to the donating water monomer, one accepting a hydrogen bond from this water molecule, two water molecules that accept hydrogen bonds from the acceptor water molecule, and one that donates a hydrogen bond to this molecule. This fully solvated dimer (8 water molecules total, referred to as the octamer) was optimized at the MP2/aug-cc-pVTZ level of theory and basis set as implemented in Gaussian 16.[83] The OH distances and HOH angles of the individual water molecules as well as the OO distances were optimized. The hydrogen bonds were constrained to be linear and the angle between the donating hydrogen and the bisector of the two OH vectors on external A water molecules was set to 180 degrees.

This structure was used for all calculations involving the solvation of the water dimer.

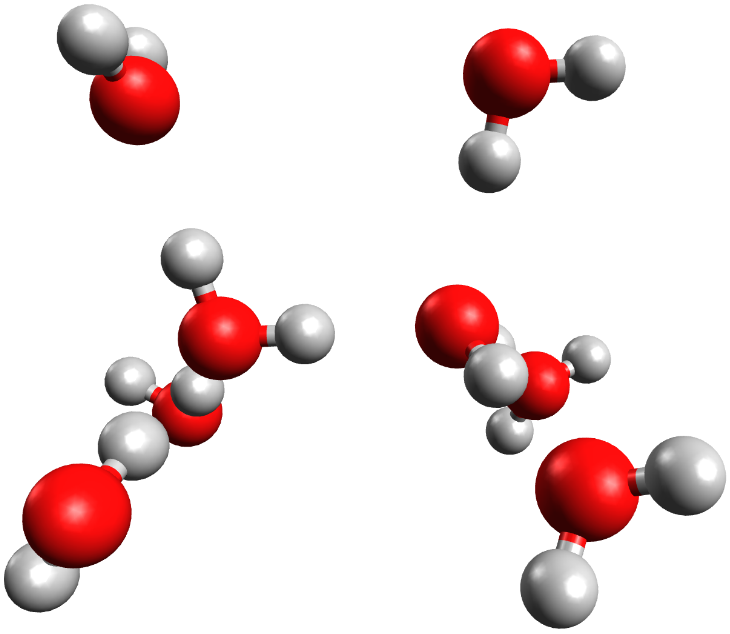

Figure 5.4: The water octamer model system. The hydrogen bonds are constrained to be linear, and the central water dimer is the subject of analysis.

To examine different solvation environments, only some of the water molecules are included in the calculation of the electron density. To obtain the electron density differences, a second calculation of the electron density is performed using the same set of basis functions, but only the electrons associated with the six atoms that make up the central water dimer were included. Specifically, ghost atoms are introduced in the positions of the atoms in the solvating water molecules, but neither the charged nuclei nor the associated electrons are included in this calculation. The electron densities for all of these systems were evaluated by calculating the electron density in discrete cubes that encompass the system using the cubegen tool in Gaussian 16. The electron density is reported based on a $100\times100\times100$ set of grid points that are placed at the center of these cubes. Electron density differences were then calculated by subtracting the calculated electron density of the dimer pair from the electron density of the larger system at each of these 100^3 points. This process was repeated for all possible donor and acceptor solvation environments.

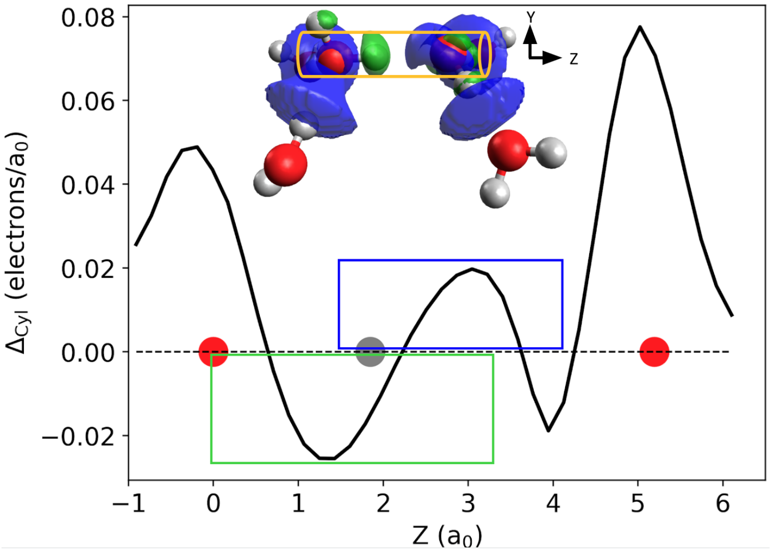

Figure 5.5: (Inset) The difference between the electron density calculated for an AAD-ADD cluster and the electron density for the central dimer in the above structure, plotted for regions where the electron density difference exceeds 0.001 electron/a_0^3. The hydrogen bonding region where the electron density is larger for the full AAD-ADD system than for the dimer is shown in blue, while the region of the donor OH bond where the electron density is depleted is shown in green. The gold cylinder shows the volume over which these densities are integrated to obtain the black curve. (Black line) The Δ_{Cyl} value, calculated using Eq. 5.2, is plotted as a function of the axis along the hydrogen bond, Z. To facilitate comparison of the plot to the inset, the locations of the oxygen atoms (red) and hydrogen atom (grey) are also shown in the plot. To evaluate δ_e using Eq. 5.3, hydrogen-bonding feature is integrated over the length of the green box to obtain δ_{HB}, while the OH bond feature is integrated over the length of the blue box to obtain δ_{OH}, and the difference between these two quantities is evaluated.

The electron density difference between the cluster with the strongest hydrogen bond, AAD-ADD (M=4), and the isolated water dimer is shown in the top inset of Figure 5.5. The change in electron density shows a significant increase in electron density in the hydrogen bonding region (blue) along with a depletion of the electron density in the region of the covalent OH bond in the donor molecule (green). This combination of changes reflects a weakening of the covalent OH bond in the donor water molecule and a strengthening of the hydrogen bond interaction between the donor and acceptor molecule. These are both types of interactions one would expect to see as the hydrogen bonding interaction is increased. We also note that these changes are localized around the O-H$\cdots$O hydrogen-bonding axis (referred to as the Z-axis in Figures 5.5 and 5.6) and have roughly cylindrical symmetry. To help compare the changes in the charge distributions among several systems, we project these distributions onto this O-H$\cdots$O axis by integrating them over circular sections with a radius of 1 a_0. This allows us to evaluate

$$\Delta_{\mathrm{Cyl}}(Z) = \int_0^{1\ a_0} \int_0^{2\pi} [\rho_{\mathrm{full}}(r,\theta,Z) - \rho_{\mathrm{dimer}}(r,\theta,Z)] r\ drd\theta \tag{5.2}$$

where ρ represents the electron density associated with either the full system or the dimer core. Operationally, this analysis is done in Cartesian coordinates, where the electron density at grid points that fall within the radius of the circular section is summed. Δ_{Cyl} is plotted as a function of Z (black curve in Figure 5.5). As noted above, the magnitudes of both the positive feature in the region of the hydrogen bond ($\Delta_{\mathrm{Cyl}}^{\mathrm{HB}}(Z)$) and the negative feature in the region of the OH bond that donates into the hydrogen bond ($\Delta_{\mathrm{Cyl}}^{\mathrm{OH}}(Z)$), provide information about the strength of the hydrogen bonding interaction. For this reason, we express:

$$\Delta_{\mathrm{Cyl}}(Z) = \Delta_{\mathrm{Cyl}}^{\mathrm{HB}}(Z) - \Delta_{\mathrm{Cyl}}^{\mathrm{HB}}(Z) \tag{5.3}$$

5.3 *Results and Discussion*

To obtain insights into the effect of the local solvation environment on the electron density around the shared OH stretch region in the water dimer, we report Δ_{Cyl} for situations in which we change either the number of water molecules participating in hydrogen bonds with the donating water molecule or the acceptor water molecule, and we report the results in Figure 5.6. In Panel A, the donor environment is varied. As can be seen, there is depletion of electron density in the OH bond itself upon adding additional water molecules, and an increase in electron density in the space between the OH bond and the accepting hydrogen bond. This corresponds to a stronger hydrogen bond overall. The trend shows that an AAD donor results in the strongest hydrogen bond (for donors: AAD $>$ AD $\approx$ AADD $>$ ADD). Likewise, Panel B shows that when the acceptor environment is varied, an ADD acceptor water yields the strongest hydrogen bond (for H-bond acceptors: ADD $>$ AD $\approx$ AADD $>$ AAD).

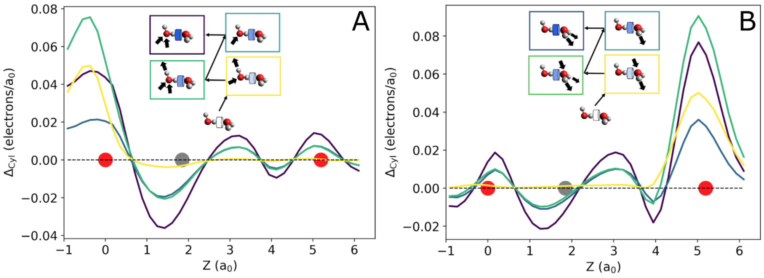

Figure 5.6: Changes in the electron density difference, Δ_{Cyl} resulting from changes in the hydrogen bonding environment of (A) the acceptor water molecule and (B) the donor water molecule.

While the trends illustrate that Δ_{Cyl} provides a way to compare changes in electron density differences across various systems, it would be desirable to encode this information into a single parameter. This can be achieved by integrating $\Delta^{\text{HB}}_{\text{Cyl}}(Z)$ and $\Delta^{\text{OH}}_{\text{Cyl}}(Z)$ as

$$\delta_e = \int_{1.5}^{4.2\ a_0} \Delta^{\text{HB}}_{\text{Cyl}}(Z) - \int_{0}^{3.5\ a_0} \Delta^{\text{OH}}_{\text{Cyl}}(Z) = \delta_e^{\text{HB}} - \delta_e^{\text{OH}} \tag{5.4}$$

In Figure 5.7, δ_e is plotted as a function of the M index. The structures shown in Figure 5.7 correspond to adding to the number of hydrogen bonds the donor accepts, increasing a′, and adding to the number of hydrogen bonds the acceptor donates, increasing d″. This choice leads to a clear trend in the M value proposed by Ohno, shown in the pink and brown arrows. On the other hand, calculating δ_e shows that this trend is truly the result of the changes in the electron density near the hydrogen bonding site, as δ_e increases as the M value increases. Furthermore, as multiple structures have the same M value, it is advantageous to examine the δ_e metric, since it provides a more detailed picture of hydrogen bond strength for the different types solvation environments.

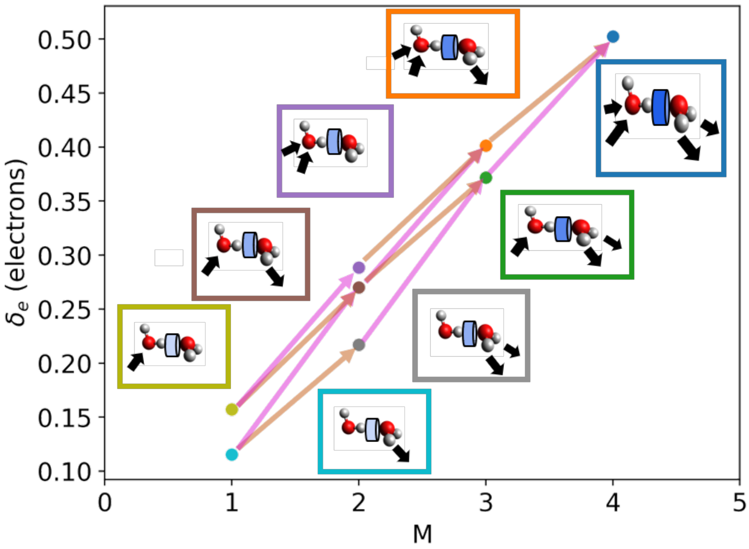

Figure 5.7: δ_e, which is calculated using Eq. 5.4, as a function of the M index (defined in Eq. 5.1) for various solvation environments. The pink arrows indicate an increase of a′, the number of hydrogen bonds the donor accepts, and the brown arrows indicate an increase of d″, the number of hydrogen bonds the acceptor donates.

The calculation of δ_e was repeated for each of the OH bonds the $Cs^+ \cdot H_2O(D_2O)_{19}$ cluster, and the results are reported Figure 5.8. For these calculations, five low energy isomers of $Cs^+ \cdot H_2O(D_2O)_{19}$ were optimized at the B3LYP/ 6-31++G** level of theory/basis using an LANL2DZ pseudopotential for Cs.[11] Single point energy calculations were then performed

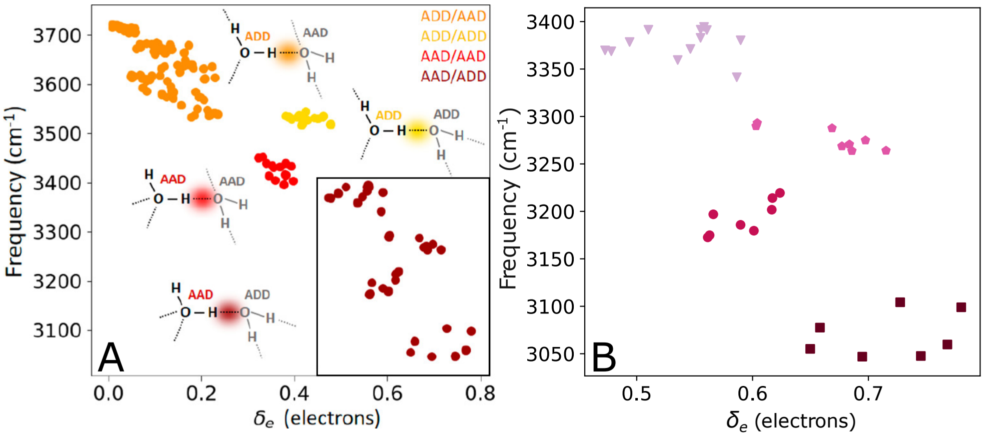

Figure 5.8: (A) Hydrogen-bonded OH stretch harmonic frequency as a function of the changes in the electron density in the donor OH group and the region along the hydrogen bond, δ_e. Calculations are carried out for five isomers of $Cs^+ \cdot H_2O(D_2O)_{19}$. Changes in the electron density are calculated relative to the isolated water dimers at each motif in the cage. (B) The zoomed-in region of the AAD-ADD dimer pairs, denoted by a black rectangle in panel A. The different shapes correspond to second solvation shell environments that are visualized in Figure 5.3

at the B3LYP/6-31++G** level of theory/basis on each of the isomers with the Cs removed. Then, single point energy calculations were performed on all donor/acceptor pairs in the isomer in a manner similar to that described for the model water system. The electron density analysis for each dimer pair was then compared to a harmonic frequency calculation, where the H_2O was placed at each donor water site in a given isomer.

In the $Cs^+ \cdot H_2O(D_2O)_{19}$ cage, it is shown that the dimer pairs with the largest changes in electron density and therefore the lowest OH stretch frequency are the AAD-ADD pairs. More broadly, it is shown that an ADD donor leads to a stronger hydrogen bond relative to an ADD donor, and ADD acceptors lead to stronger hydrogen bonds relative to AAD ones. In the AAD-ADD case, the depletion of electron density in the OH bond region can be attributed to the two monomers hydrogen bonding into the donor monomer, pulling electron density away from the OH bond. Likewise, there is an increase of electron density in the hydrogen bonding region because of more electron density being pulled from the acceptor monomer than usual. This is due to additional electron density from the two monomers on the acceptor monomer. This combination leads to the strongest hydrogen bond when considering the first solvation shell. Going one step further, the clustering of the AAD-ADD pairs in this plot demonstrates how the changes in the electron density relate to the second shell of hydrogen bonding interactions present in the cluster, color-coded in various shades of red, pink, and purple in Figure 5.3 and 5.8B. As can be seen, there is a clear clustering of different types of hydrogen bonding environments, and this is revealed by examining the frequency and the δ_e metric together.

5.4 Conclusions

In this work, $Cs^+ \cdot H_2O(D_2O)_{19}$ was used as a model system to examine how the environment of single water molecules in a sample hydrogen bonding network modulates the strength of its hydrogen bonds. We were able to perform an in-depth theoretical analysis of how the strength of a hydrogen bond is directly related to its solvation environment through examination of electron density. More specifically, we used a model water octamer that replicated the different hydrogen bonding environments of a water dimer and examined how the electron density along the hydrogen bond axis was affected by solvation of both participating water molecules with both hydrogen bond donors and acceptors. With this model, we were able to develop an appropriate metric through which to measure the change in electron density, δ_e, which is based on both the depletion of electron density in the OH bond and enhancement of electron density in the hydrogen bond region. With this metric, we showed how the categorization scheme by Ohno mapped onto the changes in the quantum mechanical electrostatic environemnt of the molecule upon solvation. This methods goes beyond the qualitative, empirical explanation by Skinner by using *ab intio* electronic structure calculations to demonstrate causality between electron movement and hydrogen bond strength.

Once this formalism was established, we applied this analysis to five low-energy isomers of $Cs^+ \cdot H_2O(D_2O)_{19}$ and found a causal relationship between it and the harmonic frequency of the OH oscillators in the large ionic cluster. In doing this, we showed that the shifts in the OH stretch frequency can be attributed to changes in the hydrogen bonding environment that are fully quantum mechanical in nature, and that the local electronic environment of the oscillator is the indicator for the hydrogen bond strength. This idea relates back to both Skinner and Ohno's work on understanding hydrogen bonding environments, but it can also be applied in the future to further understand how the spectroscopy of OH stretch oscillators can be correlated to a local environment. Since this method is general and computationally efficient, and it can be used to study larger hydrogen bonding networks in the future.

Chapter 6

SUMMARY AND ONGOING WORK

The works discussed above broadly fit into the categories of model and simulation development and analysis. The models and simulations used throughout these works were developed in pursuit of a better understanding of how quantum mechanics influences the dynamics, structure, and spectroscopy of hydrogen bonding in water and proton transfer.

After DMC was reviewed in the first chapter, the Ground State Probability Amplitude (GSPA) approach was discussed, improved, and extended to two sizes of protonated water clusters. Through both the GSPA approach and the rich information encoded in the DMC ground state wave function, the structure and theoretical spectra of the protonated water trimer and tetramer were calculated, discussed and analyzed in detail. Two significant conclusions from this study were that, when including vibrational zero-point effects, both clusters sample a high-symmetry, vibrationally-averaged saddle point geometry in the ground state that can be used as a reference structure for defining a set of coordinates for the GSPA approach, and that once the model is constructed, one can use the GSPA approach to find not only what zero-order transitions and intensities contribute to the vibrational spectrum, but also how those zero-order states couple to produce the complicated experimental spectrum. The vibrational modes that are strongly coupled to the shared proton stretch, also known as the proton transfer coordinate, were identified across both clusters and their deuterated analogs.

In the next chapter, the incorporation of machine learning into the DMC workflow greatly improved simulation efficiency. The general approach is to run small-scale DMC simulations that sample beyond the regions of the potential energy surface that are accessed by conventional DMC simulations, and then use the walker energies and coordinates to train a new version of the existing potential energy surface using a deep neural network. Once this neural network is trained, the evaluation of the potential energy, the rate-limiting step in a conventional DMC simulation, is decreased by up to an order of magnitude due to the ability to evaluate a neural network in a highly parallel fashion on a Graphics Processing Unit. The neural network workflow was shown to increase simulation efficiency for studies of H_2O, ${CH_5}^+$, and $(H_2O)_2$.

In the final chapter, a model was constructed from first principles and used to explain the known correlation between a hydrogen-bonded OH stretch frequency in water and its surrounding solvation environment. The number of water molecules solvating both the donating monomer and its acceptor has been clearly empirically outlined previously. In this work, the quantification of this phenomenon in a model based on *ab initio* electron density is put forth as an explanation for this phenomena. This model was shown to match onto previously known trends, and also provide a metric for hydrogen bond strength in the large water network in a $Cs^+ \cdot H_2O(D_2O)_{19}$ cluster. Second solvation shell effects were also discussed in the context of this cluster.

Diffusion Monte Carlo provides a powerful tool for understanding the vibrational landscape and spectroscopy of weakly bound, anharmonic molecular systems. However, there are a few challenges that come with extending these developments to new systems. The first issue is in the scaling and computational cost associated with DMC simulations.[43,127] In principle, the cost of the simulation should scale with the cost of the potential calls, while in practice the size of the ensemble required to obtain accurate results also grows with system size. The use of the guided DMC approach[37,41,43] leads to a significant reduction in the ensemble size required to obtain a high-quality ground state wave function and zero-point energy, with only a small increase in the computational cost. While this strategy renders studies of systems with up to 20 atoms feasible, at some point these calculations will also become computationally intractable.

A second and perhaps larger challenge to extending the systems for which DMC calculations are performed is the availability of potential surfaces with sufficient accuracy to obtain meaningful results, and which can be evaluated efficiently. The highly accurate protonated water cluster surface used in Chapter 3 was fit to tens of thousands of CCSD(T) calculations.[3,128] While the evaluation of this potential is substantially less expensive than the underlying electronic structure calculations, it still uses approximately 95% of the time of the calculation. The use of neural network potential energy surfaces, as outlined in Chapter 4, is a promising partial solution to this issue when potential energy surfaces are available.

Moving forward, the GSPA approach may be used in analyses of larger water cluster systems. It is not necessary to define a full $3N - 6$ set of internal coordinates for the GSPA model, instead one can construct a reduced dimensional basis composed of high frequency stretches and bends to calculate a subset of anharmonic frequencies and intensities given a DMC wave function. This may lead to further insights based on the DMC wave function without having to construct a full basis.

If potential energy surfaces are unavailable for a system of interest, the use of machine learning and DMC to construct novel potentials is also a promising area of exploration. One could in principle perform small-scale DMC simulations using on an *ab initio* potential energy surface, or perhaps using an efficient but rudimentary surface, to collect training data for a neural network to then learn. This would allow for the study of any arbitrary system with the simulation method.

Finally, the electron density difference model can be extended to even larger networks, since the calculations required to perform such an analysis are computationally inexpensive. This may allow for an in-depth analysis of how even more levels of solvation affect the frequency of an OH stretch in a water molecule.

BIBLIOGRAPHY

[1] McCoy, A. B.; Dzugan, L. C.; DiRisio, R. J.; Madison, L. R. *Faraday Discuss.* 2018 *212*, 443–466.

[2] Duong, C. H.; Gorlova, O.; Yang, N.; Kelleher, P. J.; Johnson, M. A.; McCoy, A. B.; Yu, Q.; Bowman, J. M. *J. Phys. Chem. Lett.* 2017 *8*(16), 3782–3789.

[3] Yu, Q.; Bowman, J. M. *J. Chem. Phys.* 2017 *146*(12), 121102.

[4] Duong, C. H.; Yang, N.; Kelleher, P. J.; Johnson, M. A.; DiRisio, R. J.; McCoy, A. B.; Yu, Q.; Bowman, J. M.; Henderson, B. V.; Jordan, K. D. *J. Phys. Chem. A* 2018 *122*(48), 9275–9284.

[5] Esser, T. K.; Knorke, H.; Asmis, K. R.; Schöllkopf, W.; Yu, Q.; Qu, C.; Bowman, J. M.; Kaledin, M. *J. Phys. Chem. Lett.* 2018 *9*(4), 798–803.

[6] Jin, Z.; Braams, B. J.; Bowman, J. M. *J. Phys. Chem. A* 2006 *110*, 1569–1574.

[7] Partridge, H.; Schwenke, D. W. *J. Chem. Phys.* 1997 *106*(11), 4618–4639.

[8] Babin, V.; Medders, G. R.; Paesani, F. *J. Phys. Chem. Lett.* 2012 *3*(24), 3765–3769.

[9] Babin, V.; Medders, G. R.; Paesani, F. *J. Chem. Theory. Comput.* 2014 *10*(4), 1599–1607.

[10] Paesani, F. *Acc. Chem. Res.* 2016 *49*(9), 1844–1851.

[11] Yang, N.; Khuu, T.; Mitra, S.; Duong, C. H.; Johnson, M. A.; DiRisio, R. J.; McCoy, A. B.; Miliordos, E.; Xantheas, S. S. *J. Phys. Chem. A* 2020 *124*(50), 10393–10406.

[12] Tomasi, J.; Mennucci, B.; Cammi, R. *Chem. Rev.* 2005 *105*(8), 2999–3094.

[13] Jorgensen, W. L.; Chandrasekhar, J.; Madura, J. D.; Impey, R. W.; Klein, M. L. *J. Chem. Phys.* 1983 *79*(2), 926–935.

[14] Neria, E.; Fischer, S.; Karplus, M. *Journal Chem. Phys.* 1996 *105*(5), 1902–1921.

[15] Born, M.; Oppenheimer, R. *Annalen der Physik* 1927 *389*(20), 457–484.

[16] Nielsen, H. H. *Rev. Mod. Phys.* 1951 *23*, 90–136.

[17] Bowman, J. M. *Accounts of Chemical Research* 1986 *19*(7), 202–208.

[18] Bowman, J. M.; Christoffel, K.; Tobin, F. *The Journal of Physical Chemistry* 1979 *83*(8), 905–912.

[19] Anderson, J. B. *J. Chem. Phys.* 1975 *63*(4), 1499–1503.

[20] Anderson, J. B. *J. Chem. Phys.* 1976 *65*(10), 4121–4127.

[21] Dirac, P. A. M.; Fowler, R. H. *Proceedings of the Royal Society of London. Series A, Containing Papers of a Mathematical and Physical Character* 1929 *123*(792), 714–733.

[22] Scemama, A.; Caffarel, M.; Oseret, E.; Jalby, W. QMC=Chem: A Quantum Monte Carlo Program for Large-Scale Simulations in Chemistry at the Petascale Level and beyond. In *High Performance Computing for Computational Science - VECPAR 2012*; Daydé, M.; Marques, O.; Nakajima, K., Eds.; Springer Berlin Heidelberg: Berlin, Heidelberg, 2013.

[23] Kent, P. R. C. *et al. J. Chem. Phys.* 2020 *152*(17), 174105.

[24] Lüchow, A. *WIREs Comput Mol Sci* 2011 *1*, 388–402.

[25] Zhang, S.; Motta, M. *WIREs Comput Mol Sci* 2018 *8*, 1–29.

[26] Pineda Flores, S. D.; Neuscamman, E. *J. Phys. Chem. A* 2019 *123*(8), 1487–1497 PMID: 30702890.

[27] Lester, W. A., Ed.; *Recent Advances in Quantum Monte Carlo Methods;* Recent Advances in Computational Chemistry - Vol. 2 World Scientific: Singapore, 1997.

[28] Lester, W. A.; Rothstein, S. M.; Tanaka, S., Eds.; *Recent Advances in Quantum Monte Carlo Methods, Part II;* Recent Advances in Computational Chemistry - Vol. 2 World Scientific: Singapore, 2002.

[29] Anderson, J. B.; Rothstein, S. M., Eds.; *Advances in Quantum Monte Carlo Methods;* volume 953 of *ACS Symposium Series* American Chemical Society: Washington, DC, 2007.

[30] Tanaka, S.; Rothstein, S. M.; Lester, W. A., Eds.; *Advances in Quantum Monte Carlo Methods;* volume 1094 of *ACS Symposium Series* American Chemical Society: Washington, DC, 2012.

[31] Tanaka, S.; Roy, P.-N.; Mitas, L., Eds.; *Recent Progress in Quantum Monte Carlo Methods;* volume 1234 of *ACS Symposium Series* American Chemical Society: Washington, DC, 2016.

[32] Metropolis, N.; Ulam, S. *J. Am. Stat. Assoc.* 1949 *44*, 334–341.

[33] McCoy, A. B. *Chem. Phys. Lett.* 2000 *321*, 71–77.

[34] McCoy, A. B. *Int. Rev. Phys. Chem.* 2006 *25*(1-2), 77–107.

[35] Feit, M. D.; Fleck, J. A. *J. Chem. Phys.* 1983 pages 301–8.

[36] Suhm, M. A.; Watts, R. O. *Phys. Rep* 1991 *204*(4), 293 – 329.

[37] Finney, J. M.; DiRisio, R. J.; McCoy, A. B. *J. Phys. Chem. A* 2020 *124*(46), 9567–9577.

[38] Petit, A. S.; Wellen, B. A.; McCoy, A. B. *J. Chem. Phys.* 2013 *138*(3), 034105/1–11.

[39] Barone, V.; Alessandrini, S.; Biczysko, M.; Cheeseman, J. R.; Clary, D. C.; McCoy, A. B.; DiRisio, R. J.; Neese, F.; Melosso, M.; Puzzarini, C. *Nature Reviews Methods Primers* 2021 *1*(1), 38.

[40] Petit, A. S.; McCoy, A. B. *J. Phys. Chem. A* 2013 *117*(32), 7009–7018.

[41] Lee, V. G. M.; McCoy, A. B. *J. Phys. Chem A* 2019 *123*(37), 8063–8070.

[42] DiRisio, R. J.; Lu, F.; McCoy, A. B. *J. Phys. Chem. A* 2021 *125*(26), 5849–5859.

[43] Lee, V. G. M.; Vetterli, N. J.; Boyer, M. A.; McCoy, A. B. *J. Phys. Chem. A* 2020 *124*(34), 6903–6912.

[44] Barnett, R.; Reynolds, P.; W.A Lester, J. *J. Comput. Phys.* 1991 *96*(2), 258 – 276.

[45] Hovington, P.; Drouin, D.; Gauvin, R. *Scanning* 1997 *19*(1), 1–14.

[46] DiRisio, R. J.; Lu, F.; McCoy, A. B. “rjdirisio/pyvibdmc:1.3.4”, 2021.

[47] Thämer, M.; De Marco, L.; Ramasesha, K.; Mandal, A.; Tokmakoff, A. *Science* 2015 *350*(6256), 78–82.

[48] Fournier, J. A.; Carpenter, W. B.; Lewis, N. H. C.; Tokmakoff, A. *Nature Chemistry* 2018 *10*(9), 932–937.

[49] Schaefer, J.; Backus, E. H. G.; Nagata, Y.; Bonn, M. *J. Phys. Chem. Lett.* 2016 *7*(22), 4591–4595.

[50] Sovago, M.; Campen, R. K.; Wurpel, G. W. H.; Müller, M.; Bakker, H. J.; Bonn, M. *Phys. Rev. Lett.* 2008 *100*, 173901.

[51] Inoue, K.-i.; Ishiyama, T.; Nihonyanagi, S.; Yamaguchi, S.; Morita, A.; Tahara, T. *J. Phys. Chem. Lett.* 2016 *7*(10), 1811–1815.

[52] Verma, D.; Erukala, S.; Vilesov, A. F. *J. Phys. Chem. A* 2020 *124*(30), 6207–6213.

[53] Sofronov, O. O.; Bakker, H. J. *Phys. Chem. Chem. Phys.* 2020 *22*, 21334–21339.

[54] Okumura, M.; Yeh, L. I.; Myers, J. D.; Lee, Y. T. *J. Chem. Phys.* 1986 *85*(4), 2328–2329.

[55] Yeh, L. I.; Okumura, M.; Myers, J. D.; Price, J. M.; Lee, Y. T. *J. Chem. Phys.* 1989 *91*(12), 7319–7330.

[56] Headrick, J. M.; Diken, E. G.; Walters, R. S.; Hammer, N. I.; Christie, R. A.; Cui, J.; Myshakin, E. M.; Duncan, M. A.; Johnson, M. A.; Jordan, K. D. *Science* 2005 *308*(5729), 1765–1769.

[57] Yu, Q.; Carpenter, W. B.; Lewis, N. H. C.; Tokmakoff, A.; Bowman, J. M. *J. Phys. Chem. B* 2019 *123*(33), 7214–7224.

[58] Douberly, G. E.; Walters, R. S.; Cui, J.; Jordan, K. D.; Duncan, M. A. *J. Phys. Chem. A* 2010 *114*(13), 4570–4579.

[59] Wolke, C. T.; Fournier, J. A.; Dzugan, L. C.; Fagiani, M. R.; Odbadrakh, T. T.; Knorke, H.; Jordan, K. D.; McCoy, A. B.; Asmis, K. R.; Johnson, M. A. *Science* 2016 *354*(6316), 1131–1135.

[60] Huang, X.; Cho, H. M.; Carter, S.; Ojamae, L.; Bowman, J. M.; Singer, S. J. *J. Phys. Chem. A* 2003 *107*, 7142–7151.

[61] Yu, Q.; Bowman, J. M. *J. Chem. Theory. Comput.* 2016 *12*(11), 5284–5292 PMID: 27673756.

[62] Vendrell, O.; Gatti, F.; Meyer, H.-D. *J. Chem. Phys.* 2007 *127*, 184303/1–10.

[63] Duong, C. H.; Yang, N.; Johnson, M. A.; DiRisio, R. J.; McCoy, A. B.; Yu, Q.; Bowman, J. M. *J. Phys. Chem. A* 2019 *123*(37), 7965–7972.

[64] McDonald, D. C.; Wagner, J. P.; McCoy, A. B.; Duncan, M. A. *J. Phys. Chem. Lett.* 2018 *9*, 5664–5671 PMID: 30205006.

[65] Yu, Q.; Bowman, J. M. *J. Am. Chem. Soc.* 2017 *139*(32), 10984–10987 PMID: 28756669.

[66] Yu, Q.; Bowman, J. M. *J. Phys. Chem. A* 2019 *123*(7), 1399–1409.

[67] Samala, N. R.; Agmon, N. *Chem. Phys.* 2018 *514*, 164 – 175.

[68] Dzugan, L. C. *Theoretical Treatments of the Effects of Low Frequency Vibrations on OH Stretches in Molecules and Ion-Water Complexes That Undergo Large Amplitude Motions,* Thesis, The Ohio State University, 2017.

[69] Petit, A. S.; Ford, J. E.; McCoy, A. B. *J. Phys. Chem. A* 2014 *118*(35), 7206–7220.

[70] Lee, V. G. M.; Madison, L. R.; McCoy, A. B. *J. Phys. Chem. A* 2019 *123*(20), 4370–4378.

[71] McCoy, A. B.; Diken, E. G.; Johnson, M. A. *J. Phys. Chem. A* 2009 *113*(26), 7346–7352.

[72] Guasco, T. L.; Johnson, M. A.; McCoy, A. B. *J. Phys. Chem. A* 2011 *115*(23), 5847–5858.

[73] Lin, Z.; McCoy, A. B. *J. Phys. Chem. A* 2013 *117*(46), 11725–11736.

[74] DiRisio, R. J.; Finney, J. M.; Dzugan, L. C.; Madison, L. R.; McCoy, A. B. *J. Phys. Chem. A* 2021 *125*(33), 7185–7197.

[75] Wilson, E. B.; Decius, J. C.; Cross, P. C. *Molecular Vibrations;* Dover: New York, 1955.

[76] McCoy, A. B. *Chem. Phys. Lett.* 2011 *501*(4), 603 – 607.

[77] Huang, X.; Carter, S.; Bowman, J. M. *J. Chem. Phys.* 2003 *118*, 5431–5441.

[78] Huang, X.; Bowman, J. M. private communication.

[79] Colbert, D. T.; Miller, W. H. *J. Chem. Phys.* 1992 *96*, 1982–1991.

[80] McCoy, A. B.; Hinkle, C. E.; Petit, A. S. Recent Advances in Quantum Monte Carlo Methods. In , Vol. 4; Tanaka, S.; Rothstein, S. M.; William A. Lester, J., Eds.; ACS Symposium Series 1094: , 2012.

[81] Louck, J. D.; Galbraith, H. W. *Rev. Mod. Phys.* 1976 *48*, 69–106.

[82] Eckart, C. *Phys. Rev.* 1935 *47*, 552–558.

[83] Frisch, M. J. *et al.* "*Gaussian 16 Revision A.03*", 2016 Gaussian Inc. Wallingford CT.

[84] Liu, D. J.; Haese, N. N.; Oka, T. *J. Chem. Phys.* 1985 *82*(12), 5368–5372.

[85] Vaden, T. D.; Lisy, J. M.; Carnegie, P. D.; Dinesh Pillai, E.; Duncan, M. A. *Phys. Chem. Chem. Phys.* 2006 *8*, 3078–3082.

[86] Boyer, M. A.; Marsalek, O.; Heindel, J. P.; Markland, T. E.; McCoy, A. B.; Xantheas, S. S. *J. Phys. Chem. Lett.* 2019 *10*(5), 918–924.

[87] Mallory, J. D.; Brown, S. E.; Mandelshtam, V. A. *J. Phys. Chem. A* 2015 *119*(24), 6504–6515.

[88] Jiang, B.; Guo, H. *J. Chem. Phys.* 2013 *139*(5), 54112.

[89] Cendagorta, J. R.; Shen, H.; Bačić, Z.; Tuckerman, M. E. *Adv. Theory Simul.* 2021 *4*(4), 2000258.

[90] Nguyen, T. T.; Székely, E.; Imbalzano, G.; Behler, J.; Csányi, G.; Ceriotti, M.; Götz, A. W.; Paesani, F. *J. Chem. Phys.* 2018 *148*(24), 241725.

[91] Welborn, M.; Cheng, L.; Miller, T. F. *J. Chem. Theory. Comput.* 2018 *14*(9), 4772–4779.

[92] Qu, C.; Yu, Q.; Van Hoozen, B. L.; Bowman, J. M.; Vargas-Hernández, R. A. *J. Chem. Theory. Comput.* 2018 *14*(7), 3381–3396.

[93] Abadi, M. *et al.* "TensorFlow: Large-Scale Machine Learning on Heterogeneous Systems", 2015 Software available from tensorflow.org.

[94] Johnson, L. M.; McCoy, A. B. *J. Phys. Chem. A* 2006 *110*, 8213–8220.

[95] Manzhos, S.; Wang, X.; Dawes, R.; Carrington, T. *J. Phys. Chem. A* 2006 *110*(16), 5295–5304.

[96] Li, J.; Varga, Z.; Truhlar, D. G.; Guo, H. *J. Chem. Theory. Comput.* 2020 *16*(8), 4822–4832.

[97] Kondati Natarajan, S.; Morawietz, T.; Behler, J. *Phys. Chem. Chem. Phys.* 2015 *17*(13), 8356–8371.

[98] Behler, J. *J. Chem. Phys.* 2011 *134*(7), 74106.

[99] Manzhos, S.; Carrington, T. *Chem. Rev.* 2020 page in press https://doi.org/10.1021/acs.chemrev.0c00665.

[100] Liu, Y.; Li, J.; Felker, P. M.; Bačič, Z. *Phys. Chem. Chem. Phys.* 2021 *23*, 7101–7114.

[101] Crittenden, D. L.; Jordan, M. J. T. *J. Chem. Phys.* 2005 *122*(4), 044102.

[102] Glorot, X.; Bordes, A.; Bengio, Y. Deep Sparse Rectifier Neural Networks. In *Proceedings of the Fourteenth International Conference on Artificial Intelligence and Statistics*, Vol. 15; Gordon, G.; Dunson, D.; Dudík, M., Eds.; JMLR Workshop and Conference Proceedings: Fort Lauderdale, FL, USA, 2011.

[103] Xie, X.; Persson, K. A.; Small, D. W. *J. Chem. Theory. Comput.* 2020 *16*(7), 4256–4270.

[104] Ramachandran, P.; Zoph, B.; Le, Q. V. *arXiv* 2017 page 1710.05941.

[105] Nair, V.; Hinton, G. E. Rectified Linear Units Improve Restricted Boltzmann Machines. In *Proceedings of the 27th International Conference on International Conference on Machine Learning*; ICML'10 Omnipress: Madison, WI, USA, 2010.

[106] Dozat, T. Incorporating Nesterov Momentum into Adam. In *International Conference on Learning Representations 2016 Workshop*; : Stanford University: Stanford, CA, USA, 2016.

[107] Shao, K.; Chen, J.; Zhao, Z.; Zhang, D. H. *J. Chem. Phys.* 2016 *145*(7), 71101.

[108] Chen, R.; Shao, K.; Fu, B.; Zhang, D. H. *J. Chem. Phys.* 2020 *152*(20), 204307.

[109] Rupp, M.; Tkatchenko, A.; Müller, K.-R.; von Lilienfeld, O. A. *Phys. Rev. Lett.* 2012 *108*, 058301.

[110] Montavon, G.; Hansen, K.; Fazli, S.; Rupp, M.; Biegler, F.; Ziehe, A.; Tkatchenko, A.; Lilienfeld, A.; Müller, K.-R. Learning Invariant Representations of Molecules for Atomization Energy Prediction. In *Advances in Neural Information Processing Systems*, Vol. 25; Pereira, F.; Burges, C. J. C.; Bottou, L.; Weinberger, K. Q., Eds.; Curran Associates, Inc.: , 2012.

[111] Hansen, K.; Montavon, G.; Biegler, F.; Fazli, S.; Rupp, M.; Scheffler, M.; von Lilienfeld, O. A.; Tkatchenko, A.; Müller, K.-R. *J. Chem. Theory. Comput.* 2013 *9*(8), 3404–3419.

[112] Okuta, R.; Unno, Y.; Nishino, D.; Hido, S.; Loomis, C. CuPy: A NumPy-Compatible Library for NVIDIA GPU Calculations. In *Proceedings of Workshop on Machine Learning Systems (LearningSys) in The Thirty-first Annual Conference on Neural Information Processing Systems (NIPS)*; : , 2017.

[113] Lill, J.; Parker, G.; Light, J. *Chem. Phys. Lett* 1982 *89*(6), 483–489.

[114] Fore, M. E.; McCoy, A. B. *J. Phys. Chem. A* 2019 *123*(21), 4623–4631.

[115] Babin, V.; Leforestier, C.; Paesani, F. *J. Chem. Theory. Comput.* 2013 *9*(12), 5395–5403.

[116] Tschumper, G. S.; Leininger, M. L.; Hoffman, B. C.; Valeev, E. F.; Schaefer, H. F.; Quack, M. *J. Chem. Phys* 2002 *116*(2), 690–701.

[117] Schmidt, M.; Roy, P.-N. *J. Chem. Phys.* 2018 *148*(12), 124116.

[118] Sahoo, T.; Iouchtchenko, D.; Herdman, C. M.; Roy, P.-N. *J. Chem. Phys.* 2020 *152*(18), 184113.

[119] Ceperley, D. M. *Rev. Mod. Phys.* 1995 *67*, 279–355.

[120] Yan, Y.; Blume, D. *J. Phys. B: At. Mol. Opt. Phys.* 2017 *50*(22), 223001.

[121] Yang, N.; Duong, C. H.; Kelleher, P. J.; McCoy, A. B.; Johnson, M. A. *Science* 2019 *364*(6437), 275–278.

[122] Fournier, J. A.; Johnson, C. J.; Wolke, C. T.; Weddle, G. H.; Wolk, A. B.; Johnson, M. A. *Science* 2014 *344*(6187), 1009–1012.

[123] Shin, J.-W.; Hammer, N. I.; Diken, E. G.; Johnson, M. A.; Walters, R. S.; Jaeger, T. D.; Duncan, M. A.; Christie, R. A.; Jordan, K. D. *Science* 2004 *304*(5674), 1137–1140.

[124] Tainter, C. J.; Ni, Y.; Shi, L.; Skinner, J. L. *J. Phys. Chem. Lett.* 2013 *4*(1), 12–17.

[125] Gruenbaum, S. M.; Tainter, C. J.; Shi, L.; Ni, Y.; Skinner, J. L. *J. Chem. Theo. Comp.* 2013 *9*(7), 3109–3117.

[126] Ohno, K.; Okimura, M.; Akai, N.; Katsumoto, Y. *Phys. Chem. Chem. Phys.* 2005 *7*, 3005–3014.

[127] Mallory, J. D.; Mandelshtam, V. A. *J. Chem. Phys.* 2016 *145*(6), 064308.

[128] Huang, X.; Braams, B. J.; Bowman, J. M. *J. Chem. Phys.* 2005 *122*, 044308.